EMC, RF, and Antenna Systems in Miniature Electronic Devices

Ruaro, Andrea

Publication date:
2016

Document Version
Publisher's PDF, also known as Version of record

EMC, RF, and Antenna Systems in Miniature Electronic Devices

Ph.D. Thesis

Andrea Ruaro

January 2016

The present work was carried out at GN ReSound A/S (place of employment) and at DTU Electrical Engineering in partial fulfilment of the requirements for the Ph.D. degree from the Technical University of Denmark.

Supervisors:

Kaj Bjarne Jakobsen, Ph.D.
Electromagnetic Systems, DTU Elektro, Technical University of Denmark

Jesper Thaysen, Ph.D.
GN ReSound A/S

The well in which Truth is said to reside is really a bottomless pit.

– Oliver Heaviside, in *Electromagnetic Theory*, 1893.

Abstract

Advanced techniques for the control of electromagnetic interference (EMI) and for the optimization of the electromagnetic compatibility (EMC) performance has been developed under the constraints typical of miniature electronic devices (MED). The electromagnetic coexistence of multiple systems and their mutual interaction have been the underlying theme of the work. The research results concern different aspects related to the integration of radio-frequency (RF) electronics in MEDs and hearing instruments (HI).

To control internal EMI, a novel near-field parasitic resonator (NFPR) has been researched. The structure allows for effective suppression of radiation from the MED, while taking into consideration the integration and miniaturization aspects. To increase the sensitivity of the system, a compact LNA suitable for on-body applications has been developed. The LNA allows for an increase in the overall sensitivity of a system comprised of two HIs communicating among them.

To optimize the on-body and off-body communication links of HIs, a novel wearable antenna was designed. The design originates from considerations about the EM environment where the antenna operates. An EMC-robust alternative to the on-body link was investigated through the use of body-coupled communications (BCC) and integrated with the antenna in a unique system.

Overall, the novel researched solutions effectively addressed a set of intra- and inter-system EMI and EMC issues, as dictated by the complexity of emerging modern miniature electronics.

Resumé

Avancerede teknikker til reduktion af elektromagnetisk interferens (EMI) og optimering af elektromagnetisk kompatibilitet (EMC) er udviklet under de begrænsninger, som er typisk for miniaturiseret elektronisk udstyr (MED). Den elektromagnetiske sameksistens af flere systemer og deres indbyrdes samspil, har været det underliggende emne for dette arbejde. Forskningsresultaterne vedrører forskellige aspekter relateret til integrationen af radiofrekvenselektronik (RF-elektronik) i MED og høreapparater (HI).

For at kunne kontrollere den interne EMI, er en nærfeltsparasitresonator (NFPR) blevet udforsket. Strukturen tillader effektivt undertrykkelse af strålingen fra MED, idet der tages hensyn til integrations- og miniaturiseringsaspekter. For at øge systemfølsomheden, er der udviklet en kompakt LNA, der er velegnet til på-kroppen-applikationer. LNAen giver mulighed for at forøge den samlede følsomhed af systemet, der består af to høreapparater, der kommunikerer med hinanden.

For at optimere på-krop og ud-af-krop kommunikationsforbindelsen, er der designet en ny bærbar antenne. Designet hidrører fra overvejelser om det elektromagnetisk miljø, hvori antennen skal fungere. Et EMC-stærk alternativ til et link på kroppen, er blevet undersøgt ved brug af kropskoblet kommunikation (BCC), der er integreret med antennen til et unikt system.

Samlet set adresserer de nye forskningsløsninger effektivt et sæt af intra- og intersystem EMI- og EMC-problemer, som dikteres af kompleksiteten af moderne miniaturiseret elektronik.

Sommario

Tecniche avanzate per il controllo delle interferenze elettromagnetiche (EMI) e per l'ottimizzazione della compatibilità elettromagnetica (EMC) sono state studiate sotto i vincoli caratteristici dei dispositivi elettronici miniaturizzati (MED). La coesistenza elettromagnetica di diversi sistemi e la loro interazione reciproca sono stati i temi sottostanti del lavoro. I risultati della ricerca riguardano diversi aspetti dell'integrazione di elettronica a radiofrequenza (RF) in dispositivi miniaturizzati e apparecchi acustici (HI).

La ricerca esamina una nuova struttura, cioè un risuonatore parassita (NF-PR) posto in prossimità di una sorgente elettromagnetica, per controllare l'interferenza interna. La struttura permette la soppressione effettiva della radiazione generata in un dispositivo, tenendo conto degli aspetti di integrazione e miniaturizzazione dell'elettronica. Un compatto amplificatore a bassa figura di rumore (LNA) adatto per applicazioni indossabili è sviluppato per migliorare la sensibilità del circuito radio. L'amplificatore permette un miglioramento della sensibilità complessiva di un sistema composto da due apparecchi acustici che comunicano tra loro.

Una nuova antenna, adatta ad essere indossata, è stata progettata per ottimizzare i collegamenti radio degli apparecchi acustici. Il concetto è sviluppato a partire da considerazioni sull'ambiente elettromagnetico in cui l'antenna si trova ad operare. Un collegamento radio alternativo, robusto da una prospettiva di compatibilità elettromagnetica, è stato studiato attraverso l'uso di comunicazioni intra-corpo e integrato con l'antenna in un unico sistema.

Nel complesso, le nuovi soluzioni studiate affrontano con efficacia una serie di problemi di EMI e EMC, sia interni all'elettronica che riguardanti l'interazione con altri dispositivi, che stanno emergendo a causa della complessità della moderna elettronica in miniatura.

Preface

This thesis documents the work that was carried out within the framework of the project "Advanced techniques for EMI control and EMC optimization in miniaturized devices". The project was funded by GN ReSound A/S (GNR), a leading manufacturer of hearing instruments, and by the Innovation Fund Denmark (IF). The work was carried out in the R&D Radio Systems group at GNR and in collaboration with the Electromagnetic Systems group of the Department of Electrical Engineering at the Technical University of Denmark (DTU).

I would like to extend my whole-hearten thanks to all the colleagues at GNR and DTU that supported me with comments and feedback, showed interest in my work, and challenged me to constantly rise the bar. My professional growth would have not been the same without this. In particular, I would like to thank my supervisor Jesper Thaysen for granting me the opportunity to carry out this project and for his constant support and mentoring throughout it. Finally, I would like to extend my deepest gratitude to my supervisor Kaj Bjarne Jakobsen for his invaluable technical advice and friendly mentorship. Not once, in all these years, I found his door closed for me. Kaj, thank you for the trust you put in me, for always listening to me, and for helping me to shape this work.

Copenhagen, February 2016

Andrea Ruaro

List of Publications

The following publications contributes to the study. The papers [P1–P12] are attached on pages 43–121.

[P1] A. Ruaro, J. Thaysen, and K. B. Jakobsen, "Metamaterial-inspired near-field resonant parasitic structure for directional suppression of narrow-band EMI/RFI in compact systems", in *Proceedings of the Antennas and Propagation Symposium / International Union of Radio Science (AP-S/URSI)*, 2013.

[P2] ——, "Mitigation of unwanted forward narrow-band radiation from PCBs with a metamaterial unit cell", in *Proceedings of the European Microwave Conference (EuMC)*, 2013.

[P3] ——, "Directional EMI reduction on PCB transmission lines via a near-field parasitic resonator", *IEEE Transactions on Electromagnetic Compatibility*, 2016, submitted for publication.

[P4] ——, "Simultaneous out-of-band interference rejection and radiation enhancement in an electronic product via an EBG structure", in *Proceedings of the International Microwave Symposium (IMS)*, 2014.

[P5] A. Ruaro, S. Gülstorff, J. Thaysen, and K. B. Jakobsen, "Compact and ultra-low-power 2.4 GHz LNA for on-body communication devices", in *Proceedings of the Radio and Antenna Days of the Indian Ocean (RADIO)*, 2015.

[P6] A. Ruaro, S. Kvist, S. Gülstorff, J. Thaysen, and K. B. Jakobsen, "Influence of the antenna impedance variation and input matching network Q on LNA key figures", in *Proceedings of the Loughborough Antennas and Propagation Conference (LAPC)*, 2012.

[P7] A. Ruaro, J. Thaysen, and K. B. Jakobsen, "Cavity-backed on-body antenna for custom hearing instrument applications", *IET Electronics Letters*, 2015.

[P8] ——, "Rapid prototyping analysis and modeling of a small antenna for binaural hearing aids", in *Proceedings of the International Symposium on Antennas and Propagation (ISAP)*, 2015.

[P9] ——, "Battery coupling impact on the antenna efficiency in a small wearable device", in *Proceedings of the Loughborough Antennas and Propagation Conference (LAPC)*, 2015.

[P10] ——, "Wearable shell antenna for 2.4 GHz hearing instruments", *IEEE Transactions on Antennas and Propagation*, 2015, submitted for publication.

[P11] ——, "Head-centric body-channel propagation paths characterization", in *Proceedings of the European Conference on Antennas and Propagation (EuCAP)*, 2015.

[P12] ——, "Combined antenna—electrode system for custom hearing instrument applications", *IET Electronics Letters*, 2016, submitted for publication.

Contents

1

Introduction

Hearing instruments (HI) are today among the most miniature electronic devices (MED) with communication functions. The complexity of the medical high-tech applications exists together with the production needs typical of wearable consumer electronics. The trend in the evolution of electronics toward miniaturization has pushed the HIs from being relatively bulky, analog devices to become extremely compact, digital instruments. In particular, in recent times grew stronger and stronger the need of being able to operate the two devices that are placed on each side of the head as a single system. Most users, in fact, use two HIs, as their hearing loss is due to physiological factors like aging, which naturally impacts both ears. There is a substantial advantage in connecting two devices to each other: the possibility of true binaural hearing. In fact, our brain processes best audio cues that are presented to both ears [1]. Furthermore, a variety of more complex scenarios and true device "artificial intelligence" are empowered by connectivity. Some function examples may be: adaptive directionality, combining narrow-beam with omnidirectional microphone patterns; sound field depth perception, e.g., discern among a talk with a person nearby from a loud voice down the road; improved speech understanding in noise, thanks to audio streaming from the device with the highest signal-to-noise ratio (SNR).

An additional aspect of the communication function built-in in the hearing instruments is the capability to connect to a wide ecosystem of external accessory devices. Such accessories may range widely, as for instance: a remote control for easy selection of audio programs, instead of using the small physical button present on the HI shell; a television streamer that connects the HIs to the TV audio, removing the need of using, e.g., circum-aureal headsets that uncomfortably fit with HIs; a remote microphone for sampling the voice signal where it is stronger, e.g., close to a speaker's mouth (that might be a teacher, a car driver, or the like) and then stream it to the HI user.

Finally, there is a whole range of applications enabled by the possibility of establishing a connection to a smartphone, as this allows to take advantage of its communication capabilities and to truly bring the HIs to be part of the so-called "Internet of Things" (IoT). Prospective benefits range from direct streaming of the voice calls, to new possibilities of listening to music, to use more advanced features such as geolocation and the received signal strength indication (RSSI) reading for localization of lost devices or automatic program selection. It is as well not to be underestimated the impact that the introduction of new, modern, and ultimately appealing technologies has on the perception of the hearing impaired themselves. This might assist in

winning the stigma associated with hearing loss, still present in many contexts, and ultimately increase the adoption rate of the devices.

This new set of applications nevertheless comes at the price of an increased system complexity. In order to support connectivity, the HIs must integrate a radio system on the physical layer, which consists of at least a radio-frequency integrated circuit (RFIC) and an antenna. The introduction of a complete radio system is unfortunately rather demanding on the battery and processing capabilities of an ultra-compact, ultra-low-power device. Moreover, it causes a substantial issue in the integration process in regards to the coexistence among many components, which address different needs each, that are closely packed together. This includes, for instance, the loudspeaker or audio receiver, discrete or surface-mount microphones and their respective wiring, an extremely sensitive ferrite-core magnetic coil (called telecoil), etc. Further elaboration on this is presented in Section 2.2.

Traditional electromagnetic compatibility (EMC) techniques, such as systematic filtering or shielding, are severely hindered by the lack of physical space. In fact, they rely on significant electrical and mechanical design freedom, e.g., the ability to introduce a large solid ground plane, a closed shield around parts of the electronics, freedom in the printed circuit board (PCB) layout, the insertion of decoupling capacitors and filters wherever they are needed, and so on [2–5]. This is unfortunately not an option in the complex miniaturized environment that is found in HIs. Therefore, new techniques that take into account the specific needs of electronic integration are to be investigated.

This study investigates innovative methods in order to enhance the electromagnetic interference (EMI) control, or equivalently optimize the EMC performance, in electronics with a form factor similar to that of the products of GN ReSound A/S — that are both HIs and wireless accessories operating in the 2.4 GHz industrial-scientific-medical (ISM) band. Generally speaking, the definition of EMC/EMI is rather wide. The activity revolves around the common understanding of EMI, given as: "Any electromagnetic disturbance that interrupts, obstructs, or otherwise degrades or limits the effective performance of electronics and electrical equipment. It can be induced [...] unintentionally, as a result of spurious emissions and responses, intermodulation products, and the like." [6, Lemma 4.169]. Therefore, the research activities focus on such issues: ways to control, reduce, or prevent such disturbances; or strengthen the victim sub-system against them; or define a strategy for design-to-EMC.

The project is interdisciplinary among different areas, spanning from circuit topics (such as noise reduction and filtering) to PCB and signal integrity (SI) studies, to electromagnetic (EM) coupling and environment, and to antenna design. In particular, the different items investigated are grouped into two main areas:

- Desensitization and self-jamming among digital and analog sub-systems on physically- and electrically-small PCBs, studied in term of radio receiver sensitivity and EM coupling (simulation, characterization and measurement).

- Antenna and system design-to-EMC, together with considerations and analysis on how to hinder external interference.

The study is based on a full electromagnetic approach, i.e., the use of Maxwell's Equations. The approach aims to be cross-disciplinary within the EMC research field and include every physics aspect. Thus, the approach used here is very different from the more traditional circuit-based models and trial-and-error based approaches to EMC. As well, it does not include considerations on software or digital solutions.

Henceforth, the scientific goal of the study has been to perform an in-depth research in the field of EMC for miniaturized devices. From an industrial perspective, the project addressed possible solutions to the intra-system EMI problems and to the inter-system EMC reliability challenge. In this way, connectivity can still be a key driver in the future of the HI industry: in order to retain their respective competitive advantage provided by the proprietary radio systems, companies have to fully understand and own in-house a deep knowledge of the subject. In a wider perspective, the topic is critical for the productiveness of electronics and communications companies.

The subjects are organized in this thesis as follows. Chapter 2 addresses the possible sensitivity and emission-compliance issues rooted in the device electronics, as comprised of integrated circuits (IC) and PCB. More in detail, Section 2.2 deals with interference sources and victims all internal to a single HI device, whereas Section 2.3 focuses on the enhancement of receiver sensitivity in order to improve the link budget. Chapter 3 instead discusses connectivity among two HI devices in presence of external environmental interference, addressing it from the antenna design side and, in general, studying other techniques to ensure reliable communication. Finally, Chapter 4 summarizes the findings and outlines prospective work.

The purpose of the work documented in this thesis is to provide the reader with an overview of the developments researched within the subject. Further details on the different parts can be found in the individual studies reported in the appended papers [P1–P12].

2

Intra-System EMI Prevention

2.1 Background

EMC understanding and control is a key part of the research and development applied to commercial products. First and foremost, it is a legal issue: the compliance with the public regulation. In fact, in order to preserve the electromagnetic spectrum efficiency, electronic devices must operate without interfering with others nearby, for instance by limiting their out-of-band radiation below a given field strength level. This regulation is typically enforced by public bodies and is a necessary condition for the devices' commercialization. Hence, it is of critical importance to monitor the EMC aspects during the development of an electronic product. In fact, if the risk associated to EMC failures is not managed along the process, issues may arise at an advanced project stage: at which point, any initiative targeted to correct such problems may be really expensive and cause significant delays in the time-to-market.

An electronic device typically comprises of a number of sub-systems, each addressing a specific function. In particular, considering HIs as a benchmark, a wide array of sub-systems needs to coexist in a limited physical space. The discussion can be easily extended to most MEDs. Exploded views of a behind-the-ear HI are shown in Figure 2.1, where the different sub-systems are color-coded and pinpointed. The core blocks can be divided according to their function:

- Analog audio system. This includes the microphones (which may be MEMS,

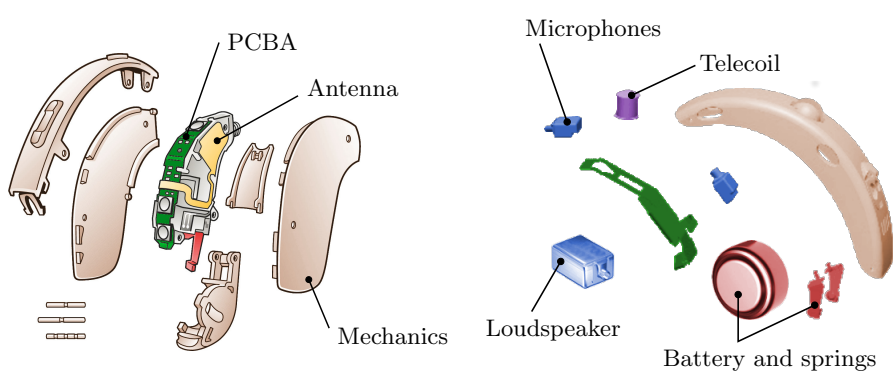

Figure 2.1. Two exploded views of a HI, with components highlighted. Courtesy of GNR.

SMD, discrete, ...) and the respective wiring. The wiring may be implemented with traces on a PCB or with litz wires: these transmission lines are typically filtered for audio purposes at kilohertz-range frequencies, but are potential radiators at RF. Another component of the analog audio system is the loudspeaker, or audio receiver. Its position may vary widely across different HI models, and can for instance be placed inside or outside the device's main body. The signal typically arrives at the loudspeaker through litz wires.

- Power system. This includes a power supply, typically a battery, which is zinc-air in the case of HIs, but Li-Ion is as well commonly found in MEDs. The battery may have different sizes according to each device design. The power system also includes the gold-plated or metallic battery springs, that are mostly a function of the mechanical design and may have considerable electrical size. The power is routed through a power distribution network (PDN) that consists of power supply lines. The power lines are typically decoupled, at least for a subset of frequencies. A proper decoupling is quite difficult to implement at low frequencies, as the capacitors have a physical size that is relevant in the context of MEDs, given the little space available on the PCB. The system may also include a power regulator, together with the relative additional network of power supply lines.

- Digital system. Its core is the digital signal processor (DSP). It can be made of one or more ICs, as there are many different digital blocks: A/D converters, memory stacks, etc. In most cases, the very own nature of digital signals and the choices regarding their routing is typically critical for the EMC performance of the device. This is due to the very sharp voltage steps that repeats at a high switching frequency, which generate a large array of harmonics in a wide frequency range. Digital signals are also carried on transmission lines among ICs, and is critical to guarantee their signal integrity (SI) performance.

- Sensor system. In the case of HIs, this may be represented by the telecoil; in other contexts, it could be the speaker's coil in a mobile phone [7]; motion sensors in a wrist-worn device; and so on. The telecoil is an analog device that is designed to couple to induction loops, which are placed in the ceiling or floor of public places such as churches or train stations. It is at its essence a coil wrapped around a ferrite core. Given the fact that it is designed to sense weak changes in the magnetic field, it is extremely sensitive to unintended radiation as well. The telecoil is wired to the PCB with litz wires.

- Radio system. This comprises of the RFIC, the RF transmission lines and matching network, and the antenna.

- Mechanical system. This includes physical parts as lossy plastics, and the physical user interface, that in HIs typically comprises of a push button and volume control. Overall, it can provide extreme constraints for the placement of the components.

Miniaturization in HIs has been mostly driven by aesthetic and functional needs. The same trend is as well noticeable in wearable electronics or handsets: in all these

applications, in fact, space comes at a premium. The compactness of the devices demands a strong system integration, which leads to the placement of the components very close to each other. The physical proximity easily translates into electrical proximity, i.e., there is a risk of electromagnetic coupling among sub-systems dictated by their physical placement. Unfortunately, there is no clear way out—and it is safe to assume that the trend will continue toward future "invisible electronics". It is therefore clear that, from an EMC-wise perspective, all the sub-systems discussed above can act both as aggressors and victims. Artifacts induced in a system due to the operation of another are not uncommon.

To summarize, the proximity of multiple functional sub-systems, which is dictated by the small dimensions of the electronic devices, poses serious constraints on the implementation of traditional EMC techniques, as briefly mentioned in Chapter 1. The issue is then aggravated by additional industrial requirements. Therefore, it is the *combination* of specific set of requirements that make MEDs particularly demanding. A review of state-of-the-art techniques and their limitations is presented in Section 2.2. The analysis makes visible a strong need to look for specific, innovative solutions, that take into account the trends of electronic integration and miniaturization.

2.2 Self-jamming

Integration and *miniaturization* are the keywords at the core of this section. In fact, the cause of many of the discussed issues is rooted into the very trends of modern electronics. Tackling them requires a shift in perspective: the issues cannot be faced as self-standing, but must be understood in their reciprocal interaction.

As discussed, inside a HI or MED there is a large number of possible EM aggressors. A first target of these may be the RFIC itself. In this case, desensitization or the receiver may occur, i.e., there is a loss of sensitivity due to the presence of EM noise. An interesting consideration in the case of the studied HIs is that, given the fact that it has been possible to increase the radio sensitivity by amplifying the signal at the input as described in Section 2.3, then the radio itself is not directly desensitized. This works as an indicator: if the limiting factor of the sensitivity was due to interference, i.e., to a high noise floor, the noise level would as well be amplified by a LNA placed in front of the receiver, and hence this action would not result in an actual increase in sensitivity. Nevertheless, desensitization is extremely case-specific and depends, among other factors, on the given 3D positioning of the different components. It is typically assessed with a total isotropic sensitivity (TIS) measurement.

A relevant EMI/RFI problem may be generated by the radio system itself. In fact, in a structure such a direct-converter transceiver there is an actual risk that the voltage-controlled oscillator (VCO) waveform leaks back at the input terminals of the transceiver itself, and is subsequently radiated while the radio is in RX mode. This causes a local oscillator (LO) leakage that may be above the emission threshold required by EMC regulation. As a side note, in this case an LNA placed on the RX chain as discussed in Section 2.3 would assist in solving the problem, since its inverse isolation would attenuate the noise signal below any sensible threshold. Traditional solutions like filtering are here not an option in this case. Even admitting that additional physical space on the HI's or MED's PCB would be found to place SMD components, the closeness among the rejection frequency and the received sig-

nal would demand high selectivity: i.e., an high order filter, that is likely to exhibit high IL for both RX and TX operation, in a context where every dB is of critical importance. Another possible issue to EMC approval which is rooted in the radio system itself are the higher-order harmonics generated by the RFIC's power amplifier (PA). These occur at multiples of the operating frequencies, i.e., at frequencies at which the antenna is likely to be resonant and a very effective radiator. This can be partly taken into account when designing the antenna matching network, but the final result—which is a compromise among different needs—might not be sufficient to leave a reasonable safety margin to account for the uncertainties and device-to-device variations. Overall, LO leakage and PA harmonics can act as actual interference sources which can compromise the product approval [8, 9].

The radio itself—or other power-hungry components—can be the cause of another serious issue. On the contrary to the previous one, which is relative to the device radiation toward the outer EM environment, this is caused by the near-field coupling to other components of the MED. In particular, any trace on the PCB can act as a radiator. This is even more true due to the fact that the ground plane is extremely small, as it is large as maximum as the whole PCB, i.e., a few squared millimeters. Since all the available layers are used for routing in order to allow a more efficient use of the available space, there is not much space left for a real solid ground plane. This also excludes the use of a power plane for power distribution. The ground plane may be even further divided in order to prevent interference among the audio and the digital parts; a ground plane dedicated to the radio system would be desirable instead. Furthermore, the antenna, when used in an unbalanced architecture, is strongly influenced by the currents running on the ground plane that define its polarization characteristic—which is of critical importance for the system performance, as given by, e.g., the ear-to-ear (E2E) metric [10]. Thus, a poor ground plane means that most PCB traces have relatively high impedance, i.e., high radiation resistance. They are also routed consistently around the edges of the PCB, due to space constraints, and are therefore even more critical from a radiation perspective [2, 11].

If any trace on the PCB can be a radiator, many components can act as radiation sources; every nonlinearity of the circuit complicates the scenario. For example, a possible source may be power-hungry ICs which operate in a switched-mode power supply (SMPS) regime [12]. This is a well-known phenomenon for most mobile phones when operating in the GSM bands: in fact, it is similar to the so-called GSM "buzz" or "bumblebee". In mobile handsets, in fact, GSM operation runs under time-multiplexing. This means that the RX components are activated a number of times to listen to the radio station. It causes the components to require a large amount of power from the battery: this can be seen as current pulses routed along the power distribution network (PDN) traces, or as voltage transients excited all along the device. This disturbance is subsequently radiated and couples to nearby analog audio systems at the frequency of 217 Hz, hence being in the audible spectrum [13]. This phenomenon can be generated as well by the 'charging' function of a voltage regulator, or by any SMPS draining power from the battery. The induced voltage transients creates current pulses traveling along the PDN, that may form loops-like structures. This excites a strong magnetic field moment. Unfortunately enough, in some devices as HIs there might be sensors extremely sensitive to magnetic fields, which in the case of the telecoil. It shall also be recalled that this is a true 3D problem, as the orienta-

tion of all components (often placed on flex PCBs) and of the generated EMI fields is of critical importance for the resulting coupling among aggressors and victims. This problem is not to be confused with the susceptibility of such components to external EM fields, for example generated by mobile phones [14]. It is a well-known different subject and is addressed by hearing aid compatibility (HAC) regulation for mobile phones, which defines a specific rating for the phones (including a telecoil rating) according to their near-field EM distribution [15].

The radiating traces are nonetheless not the entirety of those routed on the PCB. In fact, in a high-complexity environment, are typically present high-speed digital connections among different circuits. Thus, in order to preserve the SI performance, the routing and characteristics of the transmission lines must be taken into account [16]. From a SI perspective, the main requirement is that the performance is not worsened by the application of a solution aimed to suppress EMI. This is not straightforward, as multi-gigabit-per-second transmission are characterized by rise and fall times in the order of fractions of nanosecond, i.e., pulses are launched at different frequencies in the gigahertz range. The attenuation of EMI has necessarily to take place in close proximity of these digital transmission lines, while it cannot affect the performance of the digital sub-system.

Additionally, the very compact dimensions of the whole PCB makes difficult even to detect the precise location of the EMI source. In fact, automated probing systems require a high mechanical precision and probes with both high spatial resolution and high sensitivity [17]. As MEDs fall out of the scope of present commercial measurement systems, which do not provide adequate solutions, EM simulation software can be used, but the high amount of variables hinder their effectiveness.

Radiation suppression via near-field coupling

To summarize, the requirements can be organized as follows:

1. The EMI source (or multiple sources) are situated on the top layer of a PCB, and it is not possible to act directly on the coupling path in between the sources and the victim. It is not possible to rearrange the layer stack-up in order to use a ground or power plane as a partial shield.

2. The precise EMI source position is unknown, but it is known that it is located within an area of few square millimeters.

3. The space available to implement the solution, either on board or in the device, is strongly sub-wavelength at the frequency of noise rejection.

4. High selectivity. As in some cases the desired information signal is at a frequency close to that of the noise interference, the signal level at the operating frequency cannot be reduced more than fractions of decibel.

5. A narrowband filter range is suitable. This because the single radiation sources (e.g., LO leakage or PA harmonics) are inherently narrowbanded. Proceeding with the evolution of the solution, a wideband behavior would be desirable, but so far it appears overdemanding given the sum of the constraints.

6. The ground plane is physically and electrically small, and its integrity cannot be compromised. The ground plane may be connected to an unbalanced antenna, with the result that changes on the ground plane may impact the antenna performance.

7. Co-located digital transmission lines demand SI verification.

It shall be noted how traditional solutions (e.g., decoupling capacitors, closed shields, ...) are not allowed by the miniature dimensions of the device, for which both PCB area and any mechanical addition come at a premium. In fact, high selectivity calls for high filter order, i.e., one that requires many lumped components: even if the space on the PCB is to be found, the associated losses compromise the information signal quality. The effective use of capacitors in this fashion may be restricted to the sub-GHz range [12]. The use of closed shield introduces significant manufacturing issues, not last increasing the final size of the device, which may not be an option for MEDs or HIs. Additionally, an electrically-small shield may actually couple to the noise source itself [4], and may not be necessarily beneficial to the application.

A solution widely used to suppress EMI from PCBs is the use of filtering structures implemented on a layer of the board itself. If some applications demand a wide filter rejection range, here the suppression of narrowband interference suffices, making suitable the use of, e.g., a notch filter. Only planar designs are considered here, as the size and cost of 3D solutions violate the requirements dictated by MEDs. In particular, defected ground structures (DGS) and electromagnetic bandgap (EBG) filters found their way to a various set of electronic applications [5, 11, 18, 19]. Nevertheless, the very own operating principle of EBG solutions requires the repetition of a sizable unit cell [3, 20]. Therefore, to overcome this and filter transmission lines in space-constrained devices, the use of metamaterial-inspired mu-negative (MNG) solutions was proposed [21]. In order to couple to a structure such as a microstrip line, often a complementary design is required by the orientation of the **E**-field, e.g., complementary split-ring resonators (CSSR) [22]. Unfortunately, complementary designs and DGSs affects the integrity of the ground plane: in compact applications, this might jeopardize the SI performance; or, in the case an unbalanced antenna structure is also present in the device, may alter the radiation mechanism of the antenna.

Therefore, a novel solution must be researched. A new filter structure is proposed and assessed [P1–P3]. The structure design is inspired by a unit cell geometry that, when repeated, acquires an epsilon-negative (ENG) metamaterial behaviour [23]. This design has been used in the antenna field in order to enhance given radiation characteristics of small antennas [24–27]. The structure resonance frequency and mechanism is altered by varying the geometrical parameters showed in Figure 2.2a. The size is comparable to that of the unit cell of metamaterials implementations. The structure acquires a resonant behaviour and is placed in the proximity of the radiation source, i.e., acts as a near-field parasitic resonator (NFPR). The structure is physically implemented on a layer of the PCB close to the EMI source and is connected to the ground plane with a vertical interconnect access (VIA), visible in Figure 2.2b. Together with its strongly sub-wavelength dimensions and planar implementation, a strength and novelty of this design is the rotationally-asymmetric structure, which allows for a different coupling of the structure according to the direction of the transmission lines that interact with it.

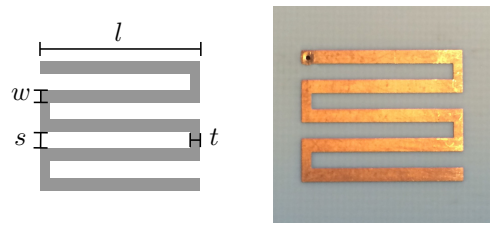

(a) Diagram. (b) Picture.

Figure 2.2. Element geometry, with dimensions [P3].

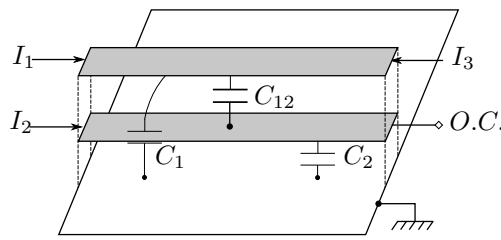

Figure 2.3. Broadside-coupled microstrip lines above a shared ground plane [P3].

Figure 2.3 shows two sections of microstrip transmission lines above a common ground plane. The two lines are situated at different heights above the ground plane. The ground reference is the same for both lines. The operating principle is similar to that of a directional coupler [28]. A current I_1 on the first line will induce a current I_2 on the second line. As the S-parameters are varying with frequency, the coupling varies and is significantly stronger when the second line is near resonance. When the element is resonant, the current is driven to ground with a VIA and is dissipated on a low-impedance surface. A series resistance can also be introduced [P3]. The structure can be made frequency-tunable by inserting a variable capacitance (e.g., by the use of a switched capacitor bank, a varactor, etc.) in series, parallel, or where the geometry of the NFPR allows.

The main results are summarized in Figure 2.4–2.7. For details, please refer to the single papers [P1–P3]. Please note, Figure 2.4a refers to a first prototype [P3], whereas Figure 2.4b and 2.4c to a second one [P2]. Figure 2.4a shows the transmission coefficient of a microstrip line crossing on a different PCB layer the location of the NFPR. Simulations (solid curves) and measurements (dotted curves) are really close to each other in both frequency and magnitude of the observed phenomenon. This supports the use of numerical simulation tools to predict performance in a fast and reliable way. The transmission line crosses the NFPR along two orientations of the latter: co-directional (black curves), i.e., when the sections of the meander line are parallel to the transmission line; and cross-directional (red curves), when the above mentioned sections are perpendicular to the transmission line. As a result, while the frequency of operation is determined by the characteristics of the NFPR itself, the magnitude of the filter effect is determined by the stronger or weaker coupling of the transmission line to the NFRP. Especially, it is seen how in the co-directional case the insertion loss is above 18 dB. The difference between the co- and cross-

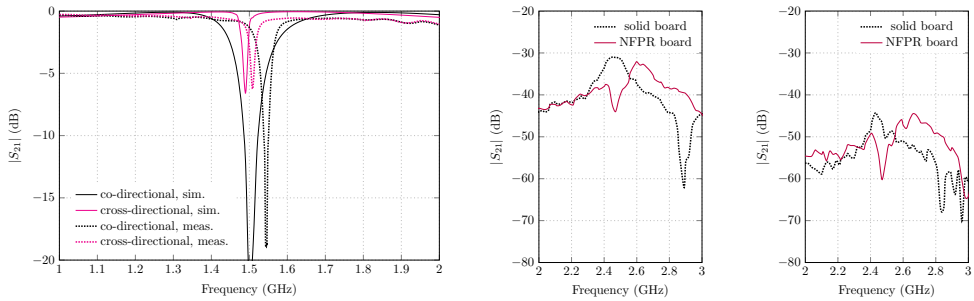

Figure 2.4. Simulated and measured performance of multiple NFPR prototypes. (a) Transmission coefficient of a microstrip transmission line crossing the NFPR, for two different orientation of the structure [P3]. (b) Emission from a board with the NFPR at a distance $d = 5$ cm from the board edge [P2]. (c) Emission from a board with the NFPR at a distance $d = 40$ cm from the board edge [P2].

directional scenarios is approximately 11 dB: this, combined with the results shown below in Figure 2.7, allows to define design guidelines for effective route tracing. In Figure 2.4b and 2.4c is shown a more comprehensive test. In fact, a strong radiation source is placed in proximity of the NFRP on a PCB. The radiation of the PCB is then sampled along the edge plane, i.e., on the same plane the PCB is laying on, at two different distances. It can be seen from the difference between the red curve to the black curve how the introduction of the NFPR strongly attenuates the radiation from the board both at a close distance and, in an even stronger way, at a farther distance (EMC compliance is tested at a fixed longer distance). This shows that the NFPR is able to effectively suppress radiation generated from a source placed above it on a PCB.

Figure 2.5 and 2.6 present further important results that are useful to understand the performance of the NFPR. Figure 2.5 shows the intensity of the simulated **E**-field on two orthogonal planes crossing the NFPR. It can be seen how the field distribution varies and the field strength is reduced along the radiation slot when the element is resonant. This qualitative observation can be linked to a quantitative parameter as in Figure 2.6, where is shown the gain pattern from a patch antenna on a PCB at different frequencies. While it can be seen in Figure 2.6a that the influence of the NFPR on a source radiating in the structure's pass-band is negligible, in the structure stop-band (i.e., near resonance) the radiation efficiency η_{rad} drops approximately of a factor 5. This means that the same radiation source is virtually unaffected in the NFPR pass-band, while it radiates much less in its stop-band. It is worth recalling that the NFPR is placed on a layer below the radiation source itself, nevertheless it is able to effectively suppress it in all directions [P2].

So far, the results assessed the ability of the NFPR to filter the unwanted radiation generated from a PCB. Figure 2.7 highlights another important aspect, which is that of SI. In fact, this assesses the impact of the NFPR on a sample digital signal routed on the trace. The eye diagram is extremely informative about a number of signal quality metrics, e.g., jitter or SNR, and offers a quick way to visualize the output

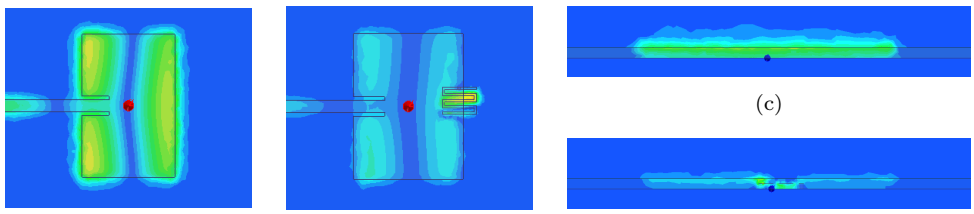

Figure 2.5. Simulated **E**-field of a patch antenna and the impact on it of the NFPR [P2, P3]. (a) Top view, reference; (b) top view, with NFPR; (c) side view, reference; (d) side view, with NFPR.

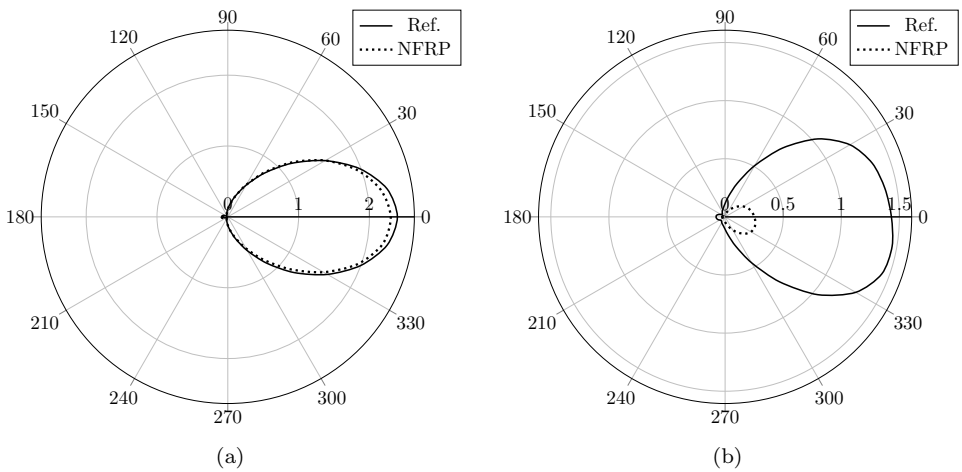

Figure 2.6. Polar plot of the simulated gain pattern of a radiation source (patch antenna on PCB) above a given NFPR [P2]. The top of the board is oriented toward 0°. Reference (solid line) and radiation source over the NFPR (dotted line) are shown (a) at a frequency $f_{\mathrm{pb}} = 2.45$ GHz in the pass-band and (b) at a frequency $f_{\mathrm{sb}} = 2.85$ GHz in the stop-band.

signal quality. In particular, it is possible to observe how the routing affects the strength of the coupling to the structure: placing the trace along the edge of the structure as in Figure 2.7c or cross-directional to the NFPR as in Figure 2.7d causes only a marginal worsening of the signal SNR. This is considered a safe method for the routing of traces carrying digital signals. On the contrary, the signal quality is noticeably affected for the case of strongest coupling shown in Figure 2.7b. Therefore, a trace routing strategy, based on the relative position and direction with respect to the NFPR, can be elaborated in order to filter noise signals from a subset of traces, while granting the signal quality of a second subset of traces routed in the same PCB area.

Coexistence EBG Structure-Antenna

A single NFPR was proven able to filter EM noise from transmission lines in an effective way. An important observation was that the use of such structure is able to reduce the radiation generated by a PCB. Relaxing in part one of the most stringent

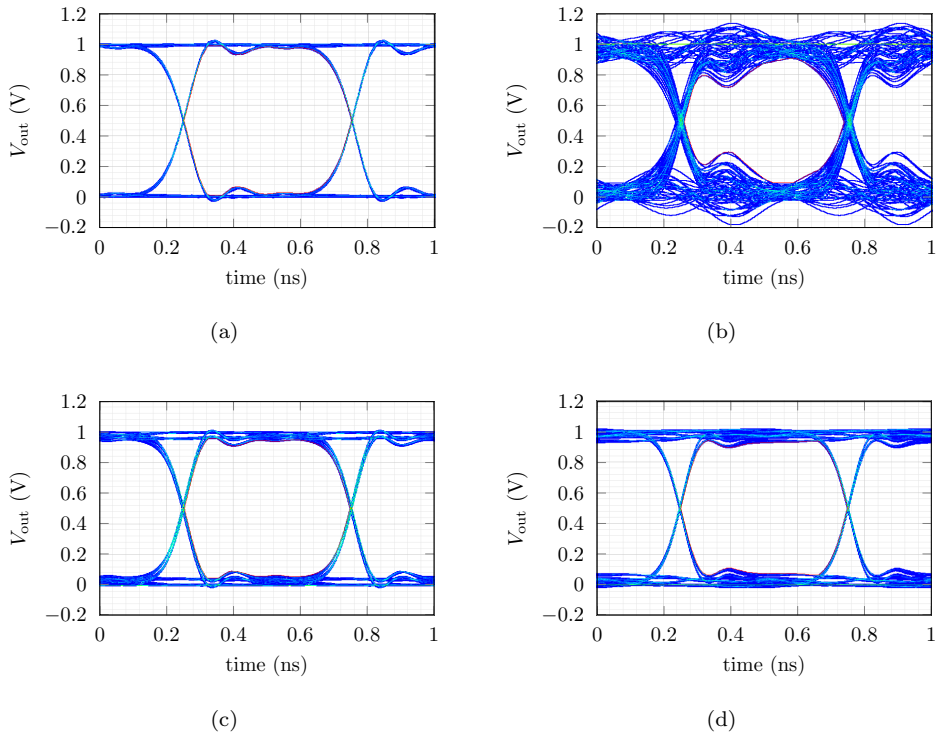

Figure 2.7. Simulated eye diagram for different scenarios of the interaction of a transmission line with the NFPR. (a) Reference board; (b) trace and NFPR co-directional and centered with respect to each other; (c) trace and NFPR co-directional and offset with respect to each other; (d) trace and NFPR cross-directional and centered with respect to each other [P3].

requirements, i.e., the space constraint, allows for a design to use a small array of unit cells. Therefore, the implementation of EBG structures become viable. As already mentioned, EBG structures are used for filtering EM noise from transmission lines and PCBs [3, 19, 20]. The operating principle is, nevertheless, different from that of the NFPR. Another category is constituted by DGS or complementary designs [11, 18]. On the other side, high-impedance surfaces (HIS) has been used by antenna scientists to improve the antenna efficiency and bandwidth, and reduce its size [29, 30]. It may be possible to implement such structures on a layer of the PCB of some MEDs. On a compact device, given that the space is sufficient to design and place an EBG structure, the needs of electronic integration demand that other systems share the space. Therefore, it is of interest to assess if the use of an EBG structure primarily intended to assist the antenna design may be used for EMC purposes, e.g., to reduce the EM noise generated by transmission lines that share a common ground plane with the antenna.

In order to do this, a complementary Jerusalem Cross pattern was etched on the ground plane as shown in Figure 2.8a. This pattern acts as an EBG structure and allows for noise filtering of EM noise from transmission lines [31]. A square patch antenna can also use this ground plane, resulting in a more compact and efficient design.

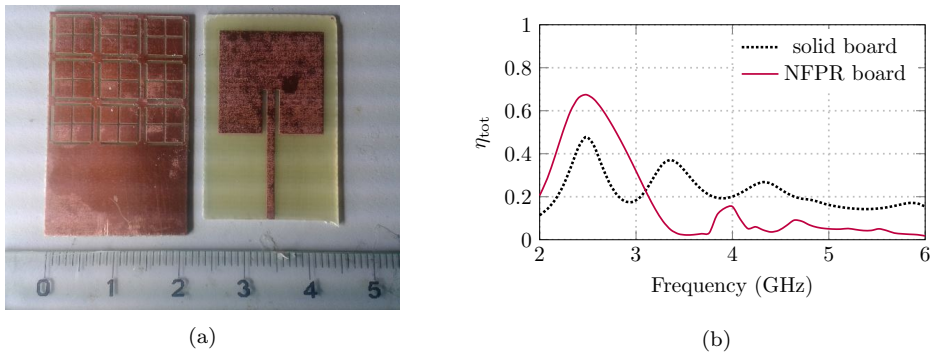

(a) (b)

Figure 2.8. (a) Prototype parts picture and (b) simulated total efficiency [P4].

The coexistence study investigates the possibility that unwanted signals, e.g., PA's higher-order harmonics, leaks to the antenna and are subsequently radiated [P4]. As shown in the plot in Figure 2.8b, the antenna implemented on the EBG ground plane is able to achieve higher total efficiency and increased bandwidth. This was expected based on literature studies. Instead, it was noticed that the radiation efficiency drops at higher out-of-band frequencies by a magnitude of 1 dB to over 10 dB, according to the frequency. Therefore, it is observed that the use of EBG structures etched on the ground plane not only can act as a EM noise filter on transmission lines, but assists the EMC performance reducing the radiated strength of out-of-band signals.

2.3 RX Sensitivity

Under the strong hypothesis that the internal environment of a MED is interference-free, no desensitization of the radio circuit is then taking place. The techniques researched in Section 2.2 can assist in improving the intra-system EMI issues. Given a system formed by a transmitter (TX) and a receiver (RX) device, in order to improve its performance is therefore possible to improve the sensitivity of the receiver RFIC. In fact, if the limiting factor of the sensitivity is not dictated by internally-generated EM noise (jammers), it is possible to increase the RX SNR. This would be inhibited in the case the desensitization of the RX is already happening: if an increase of the level of the received signal over the noise does not result in an equal increment of the overall sensitivity, it means that the noise floor is masking the signal. An increase in sensitivity can help in achieving a more stable ear-to-ear (E2E) link, and hence make the system more robust. In fact, among the largest characteristics of non-line-of-sight (NLOS) on-body links is the Rayleigh or multipath fading, that causes deep falls in the signal level due to destructive interference [32]. The problem is stronger in reflections-rich environment. It varies with respect to time in scenarios that include geometrical modifications of the operating environment, e.g., the motion of the human body. Therefore, an improved sensitivity could significantly reduce the level of lost packets, i.e., the packet error rate (PER), if the negative spikes in the signal level caused by the Raylegh fading does not bring the signal strength below the receiver threshold [33]. This would reduce the dependency of the performance from

Table 2.1. Review of CMOS LNA performance [P5].

NF (dB)	P_{DC} (mW)	V_{DD} (V)	G_{a} (dB)	IIP_3 (dBm)	Node (nm)	Year (-)	Ref. (-)
1.6	7.2	1.8	14.1	+1	180	2011	[34]
2.7	0.4	1.2	22.8	+3	180	2011	[35]
2.9	1.1	0.6	10.9	0	180	2013	[36]
4.0	1.3	1.2	20.0	−12	130	2011	[37]
4.4	0.7	1.2	9.7	−4	90	2014	[38]
4.8	0.6	1.8	14.7	+2	180	2014	[39]
5.2	0.9	1.5	21.4	−11	180	2008	[40]
1.5	1.0	1.0	6.2	−11	n/a	2015	[P5]

the specific physical environment the device is operating in.

In such case, the sensitivity of the receiver RFIC is as declared by the datasheet of the radio, and is then possible to increase the sensitivity of the radio itself. In fact, the sensitivity is generally given by

$$S = SNR_i \; k \; T_0 \; BW \; NF \tag{2.1}$$

where SNR_i is the signal-to-noise ratio necessary to process the signal, k is the Boltzmann constant, $T_0 = 290$ K, BW is the bandwidth, and NF is the noise figure of the receiver itself. According to Friis' noise equation, the noise figure of a receiving chain is given by

$$NF = NF_1 + \frac{NF_2}{G_1 - 1} \tag{2.2}$$

i.e., the overall noise figure NF is given by the noise figure NF_1 of the first stage of the chain, plus the noise figure NF_2 of the following stages weighted by the gain of the first stage G_1.

There is therefore room to improve the RX sensitivity by the use of an additional LNA placed at the input of the RFIC in the RX chain only. Most commercial RFIC datasheets report comparable sensitivity. In fact, this is a trade-off among multiple parameters, including dynamic range and overall power consumption. It has been estimated through a measurement campaign that such noise figure is in the range of $NF_2 \approx 10$ dB. In principle, nothing forbids that this parameter could be improved directly by the chip producer. In reality, research is apparently investigating trade-offs that do not privilege the noise figure in a particular way. In fact, as can be read in Table 2.1, most of the low-power to ultra-low-power and low-noise CMOS LNAs developed from the academic community do not really target the desired requirements. This might either be due to scarce awareness of this problem or to technological limitations. This applies as well for commercially-available LNAs.

Therefore, an LNA intended to operate under stringent requirements was designed and implemented in a few iterations with surface-mount components. The key chal-

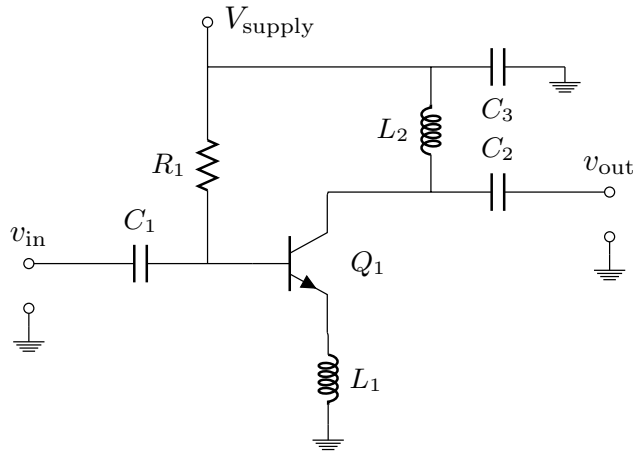

C_1	22	pF
C_2	0.7	pF
C_3	1.5	pF
L_1	0.9	nH
L_2	3.2	nH
R_1	75	kΩ

Figure 2.9. Design of the compact LNA: diagram and component list [P5].

lenges and the novelty of the selected approach were multiple, and included: an extremely small area available on the PCB (that translates in a few components count, and subsequent importance of the component footprints); a low supply voltage (down to 1.0 V); ultra-low-power consumption (less than 1 mW); and, of course, low *NF*. The final design is shown in Figure 2.9 and detailed in [P5]. Among the key design features, is the emitter feedback system, which ensures stability while it increases the bandwidth, and the reuse of decoupling components for input and output matching.

The key performance metrics of the LNA are shown in Figure 2.10. The measured *NF* is as low as 1.5 dB and the gain peaks at 6 dB as shown in Figure 2.10a, while the power constraints are satisfied. The area occupied by the LNA on the PCB is approximately 2.5 mm × 1.5 mm. The low gain helps in preventing the saturation of the internal LNA of the RFIC. The input and output reflection coefficients shown in Figure 2.10b are as intended by the design, whereas the ripple in the S11 profile is due to high VSWR on the input transmission line. In particular, the input reflection coefficient is less frequency selective because it uses a single-component matching network, that additionally doubles up as DC block. Moreover, the operation of the LNA in a context such as that of HIs faces it with an additional challenge: the impedance of the device's antenna is subject to detuning due to the morphological differences among different user's ear shape and to the time-by-time different positioning of the HI on the ear. In fact, it was studied how the variation of the input impedance can impact the performance of the LNA. It was found that a high-Q input matching network can compromise the performance, whereas a large bandwidth, i.e., a low-Q network can help in mitigating this undesirable effect [P6].

In order to assess the LNA performance in a comprehensive system-level test, the LNA prototype is installed on a PCB that also hosts the control logic. A picture of this board is shown in Figure 2.11a, where the area occupied by the LNA is highlighted. The board takes the logic control signals directly from an HI to operate. A set-up with a controlled path loss is able to show the impact of the LNA board on the overall link PER. The result is shown in Figure 2.11b in the case of, respectively: a

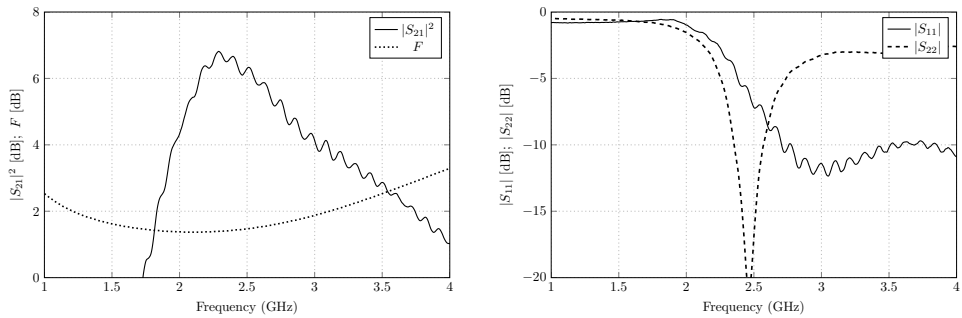

(a) (b)

Figure 2.10. Key performance metrics of the LNA [P5]. (a) Measured insertion power gain and computed noise figure. (b) Input and output reflection coefficients.

reference HI (black dotted line); a HI with the additional board in place and bypassed LNA (black solid line); the latter, when the LNA is switched on (red solid line). The improvement is in the range of approximately 6 dB. This makes the system more resilient to multipath fading, as it prevents the occurrence of packet transmission fails in the cases in which the destructive interference causes the RX signal strength to fall, up to 6 dB below the RFIC sensitivity level. Nevertheless, since the dynamic range of the RFIC is unaltered, a consequence of this is that to an increase in sensitivity corresponds a reduction of the C/I value, that was measured to be of a magnitude comparable to the sensitivity improvement.

This value can additionally be used to give a rough estimate of the RFIC *NF*. In fact, let assume

$$\Delta PER = \Delta S = \Delta NF \tag{2.3}$$

i.e., that the difference in PER introduced by the LNA is equal to the improvement in the RX sensitivity (that is reasonable, as in this application packets can be considered as i.i.d. variables), and that the only contribution to the sensitivity in Equation 2.1 is given by the noise figure. Therefore, with the definition of terms as in Equation 2.2, is given that

$$\Delta NF = NF_2 - NF \qquad \text{, i.e., } \qquad NF_2 = \Delta NF + NF_1 + \frac{NF_2}{G_1 - 1} \tag{2.4}$$

Solving for NF_2, it is obtained

$$NF_2 = (NF_1 + \Delta NF) \quad \frac{G_1 - 1}{G_1 - 2} \tag{2.5}$$

that, in this case, gives a projected RFIC *NF* value of 9.6 dB, close to the initial estimate.

2.4 Summary

This chapter discussed the challenges of MEDs, and more specifically how to tackle a set of EMI issues which can be originated within a device. After introducing the

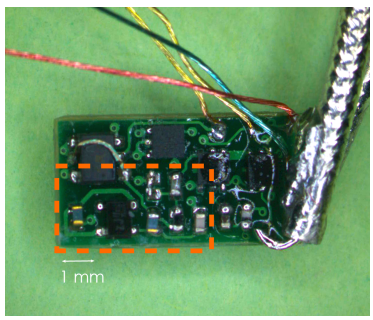

(a)

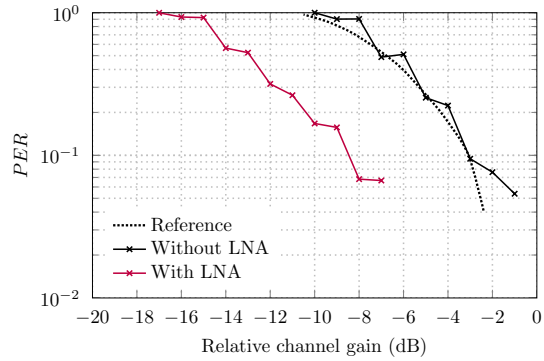

(b)

Figure 2.11. (a) A picture of the full board, hosting the LNA (highlighted area) and the control circuitry. (b) Impact of the LNA circuit on the system PER.

EM issues linked to system integration, such as LO or PA signals radiated from PCB microstrip traces, self-jamming issues have been addressed by the means of a near-field parasitic resonator (NFPR).

Given a complex list of requirements, a solution exploiting a metamaterial-inspired ENG resonator was introduced. The structure has strongly sub-wavelength dimensions and can be implemented on a PCB layer. It was shown to be highly selective and able to attenuate a noise signal of over 18 dB. The radiation generated from a board where the NFPR was added showed that the EMI was reduced by 6 to 8 dB as sampled on the board edge plane. The structure exhibits a rotationally asymmetric behaviour, that eases system integration preserving SI for signals routed on traces oriented in such a way that they couple only weakly to the NFPR. This allows to elaborate design guidelines based on the direction that traces are routed on a PCB in physically- and electrically-small MEDs. The impact of an EBG structure on a patch antenna was studied, leading to the discovery that this helps in reducing the out-of-band radiation possibly generated by the integrated electronics of a MED by an average magnitude of more than 5 dB.

Given that the internal environment of a MED is interference-free, there is no desense of the RFIC. An LNA was thus developed to increase the RX system sensitivity of an HI, and was shown to be able to do so in the magnitude of approximately 6 dB while consuming very little power from a 1.0 V supply. This allows for a reduced PER and an overall stabler on-body radio link.

3

System Design-for-EMC

3.1 Background

One of the concerns that were risen in conjunction with the use of the 2.4 GHz ISM band for the operation of medical devices was that a possible future crowding of the frequency band could cause interference problems, and hence jeopardize their functioning [41]. At present, there is nothing like a band dedicated to medical devices such as HIs, and the need for interoperability—e.g., with a mobile phone—demands for the use of an actual commercially-available band. In fact, the presence of many interferers—which number is going to grow exponentially in the next years, due to the boom of wireless accessories and appliances—could start affecting the way that hearing instruments also communicate. As for other medical devices, it is of paramount importance that the link is stable and reliable.

Certainly, a number of software and algorithm solutions that are already implemented strongly helps in mitigating the problem. Solutions as time multiplexing or frequency hopping were proven able to ensure a satisfactory link quality [33]. Nevertheless, it is important to address the potential future consequences of an excessive crowding of the 2.4 GHz band that would affect the way that the HIs communicate. In particular, the ear-to-ear (E2E) link would be the first to be affected, as it has the highest path loss [10].

The communication function, nevertheless, has to be established along many on- and off-body links, of which the E2E is only an example, even though it is one of the most critical and has foremost importance [42]. This made necessary the study of additional options in order to grant communications among a set of nodes placed around the head, as it is in this environment that HIs and possibly wearable MEDs (as eye visors, other kind of monitors, earbuds, phone clips, etc.) will operate.

The problem is hence dual. Not only it is necessary to monitor and prevent the EMI generated from inside the device and targeting parts of the device itself, compromising the performance: but as soon as we consider two devices connected by the communication function as a unique system, it shall be taken into account the potential impact of EMI generated outside the products themselves. Therefore, a system solution has to take care of both aspects: first, how to design an antenna that maximizes the likelihood of having a reliable E2E connection; and how we can design an antenna, or transmission system, that preserves a quality EMC environment inside the device.

We can relate both points to the characteristics of a good EMC environment. In fact, it is beneficial under many aspects: to ensure systems coexistence by minimizing

coupling and crosstalk, e.g., between two systems operating at different frequencies; to minimize the coupling to internal components, such as the battery or the electronics of a MED; to minimize the specific absorption rate (SAR), intended as a measure of the energy that is wasted heating the human body, i.e., it is not transmitted. In fact, it is necessary to identify which antenna design parameters lead to a result that is less prone to EMI and has overall higher reliability characteristics. In fact, the EM field distribution surrounding the antenna will have an impact over the final EMC performance of both the single device and the system. It is therefore necessary to boil down this qualitative considerations to a specific set of requirements, in order to act effectively on them and obtain a clearly measurable result.

A few key parameters must then be taken into account. In particular, those following are considered of paramount importance.

Total radiation efficiency η_{tot}. This is the product of two terms: the antenna radiation efficiency η_{rad} and the mismatch loss at the input terminals of the antenna ML, given by

$$\eta_{\text{tot}} = \eta_{\text{rad}} \quad \text{ML} \tag{3.1}$$

In turn, the latter is a function of the input reflection coefficient Γ:

$$\text{ML} = (1 - |\Gamma|^2) \tag{3.2}$$

The total radiation efficiency can be calculated in an approximate form from measurements in a radioanechoic chamber through the cabled measurement of the total radiated power TRP. In fact, in the chamber it is possible to measure the equivalent isotropic radiated power EIRP, which after being compensated for the actual transmitted power and cable losses equals the antenna gain G in a given direction. The TRP is then given by its average over the solid sphere Ω as

$$TRP = \frac{1}{4\pi} \int_{\Omega} EIRP(\theta, \phi)\ \mathrm{d}\Omega \tag{3.3}$$

Writing the solid angle in extended form according to its components θ and ϕ and separating the EIRP in its vertical and horizontal polarization component, as measured by the chamber probe, gives

$$TRP = \frac{1}{4\pi} \int_0^{2\pi} \int_0^{\pi} \big(EIRP_V(\theta, \phi) + EIRP_H(\theta, \phi)\big) \sin\theta\ \mathrm{d}\theta\mathrm{d}\phi \tag{3.4}$$

which can be approximated by a summation as

$$TRP \approx \frac{\pi}{2NM} \sum_{i=0}^{N-1} \sum_{j=0}^{M-1} \big[EIRP_V(\theta_i, \phi_j) + EIRP_H(\theta_i, \phi_j)\big] \sin\theta_i \tag{3.5}$$

Furthermore, an high on-body TRP can be related to a good specific absorption rate (SAR) performance. Even though the link among the TRP and SAR is not uniquely defined, it is commonly accepted given the fact that the radiation losses happen in the antenna itself (which includes conductor losses, but refers mostly to lossy parts such as, e.g., plastic supports) and in the user head (in the form of absorbed energy, that is subsequently dissipated as thermal energy). Therefore, minimizing the latter

is directly improving the SAR performance. Generally, SAR is regarded as not critical in most wearable applications, as the extremely low levels of transmitted power fall well below any regulatory threshold [43, 44].

Polarization P. Key parameter, as it directly impacts the ear-to-ear path gain PG_{E2E} [45–49]. In fact, only the **E**-field component polarized normally to the body surface is able to effectively excite creeping waves. Or, in other words, the tangentially-polarized component decays much faster with distance on NLOS links. The normally-polarized component coincides with the common definition of θ-component when the reference coordinate system is oriented with the XY-plane tangential to the user body and the z-axis oriented normal to it. The importance of polarization is secondary with regard to LOS off-body links.

Radiation pattern. There is no ultimate agreement on the ideal radiation pattern for on-body devices, which depends as well on each specific application. There are nevertheless a few common-sense assumptions that can be made. An omnidirectional radiation pattern is the most natural target for a small antenna, as its directivity tends to that of a small dipole, i.e., $D_0 = 1.5$ for a small antenna with $ka \ll 1$ and without a ground plane [50]. On the other side, in the HI application a radiation pattern resembling that of a Huygens source could assist in improving the PG_{E2E} [45].

Bandwidth BW. As the definition of bandwidth is not unique, it is important to specify to which reference level it actually refers to. In this study are used both the impedance 10-dB bandwidth $BW_{10\mathrm{dB}}$ and the impedance 6-dB bandwidth $BW_{6\mathrm{dB}}$. These values are referred to the return loss level, thus the bandwidth is given by the subset of frequencies for which the return loss is equal or higher the specified value. In the set of applications which MEDs and HIs belong to, the antennas are typically electrically-small and have rather high losses: therefore, $VSWR \leq 3$ is generally considered the acceptable limit [51]. The bandwidth can be related to the antenna Q factor around a resonant angular frequency $\omega_0 = 2\pi f_0$ by [52, Equation 87]

$$Q(\omega_0) \approx \frac{2\sqrt{\beta}}{FBW_{\mathrm{V}}(\omega_0)} \tag{3.6}$$

where $FBW_{\mathrm{V}}(\omega)$ is the fractional matched $VSWR$ bandwidth and β is a constant, with $\sqrt{\beta} = 1$ for the half-power $VSWR$ bandwidth [52].

Ear-to-ear path gain $\mathbf{PG_{E2E}}$. This parameter is a high-level, or system, metric. In fact, it summarizes (and is a function of) many of the parameters discussed so far. It expresses how much of the power presented at the input terminal of an antenna actually reaches the reference port of a second antenna, which is placed on the other ear in a symmetric set-up in the case of HIs. The ear-to-ear (E2E) connection can be seen like a specific demanding on-body link, but the antenna design parameters as discussed here can be applied to a broader set of applications without loss of generality. It is also important to notice that the PG_{E2E} is not a single-point value, but it has the characteristics of a statistical distribution, and it varies according to different factors as could be the on-body placement repeatability and the user-to-user anatomical variation [45]. Nevertheless, for a given set-up, for ease of comparison is reasonable to provide a single value.

3.2 Antenna Design-for-EMC

Concept

As seen so far, there are many possible interactions between the antenna of a MED and the other electronics components. Beyond the antenna-specific parameters discussed in Section 3.1 there are therefore a set of characteristics that define an antenna 'optimal' from an EMC perspective. In fact, it is desirable that the antenna is resilient to the detuning caused by the user's body: for HIs, it is the shape of the ear that matters. In case of applications such as in-the-ear (ITE) HIs, their shape is determined by that of the concha and outer ear canal of each individual user. This variation impacts the antenna performance across users [45]. Furthermore, even though this is of no real concern in HIs due to the extremely low level of output power involved, it is desirable to ensure a low level of SAR in the user tissues nearby the antenna [53]. An additional constraint is that the antenna shall maximize the room available to the rest of the electronics, this including the PCB, battery, etc. In order to reach this result, it is advisable that the **E**-field generated by the antenna is localized as much as possible, and confined in an area far from absorbers (such as the user's body) and from the rest of the electronics (to avoid EM coupling).

Therefore, to fulfill these various sets of requirements, a novel concept based on a hemispherical ground plane, shown in Figure 3.1, was introduced [P7, P8, P10]. The hemisphere is representative of the concha shape in a generalized form. In its simplest form, the radiating element is created by the use of an inverted-F antenna (IFA) arm. Therefore, the radiating principle is analogous to that of an IFA over a small ground plane, or equivalently of a $\lambda/4$ slot [54–58]. The orientation of the **E**-field is shown in the diagram of Figure 3.1b and confirmed by the numerical simulation shown in Figure 3.1c. It is of particular importance to understand how the placement and orientation of the **E**-field subsequently impact many of the key parameters, including polarization and efficiency. In this case, the **E**-field is confined to the edge of the device, a good radiation efficiency is obtained, and a reduced-coupling area is created within the hemispherical shape of the device itself. A more detailed description of the antenna can be found in [P10].

A key feature of the antenna is the use of the hemispherical cavity as the ground plane itself. This allows to maximize the volume available for the design, and helps in overcoming some of the limitations typical of small antennas: in fact, it allows for a lower Q factor, or equivalently for improved impedance match and radiation efficiency [52, 59]. Moreover, the ground plane partly act as a shield and reduces the energy lost by the antenna in the human head [60]. It can be seen in Figure 3.2a and 3.2b that, when transitioning to a less general shape, obtained from the shape of a user concha and outer ear canal, the currents and fields continue to be mostly confined between the antenna arm and the edge of the ground plane. There is therefore only little loss of generality. The orientation of the currents running on the shorting pin and of the **E**-field impacts the radiation pattern and the polarization of the radiated fields. Figure 3.2c shows the gain radiation pattern on the plane tangential to the user head, whereas the coordinate system with respect to the antenna is still that showed in Figure 3.1b: the θ-component is normal to the head and is the most critical to excite creeping waves along the head surface [10].

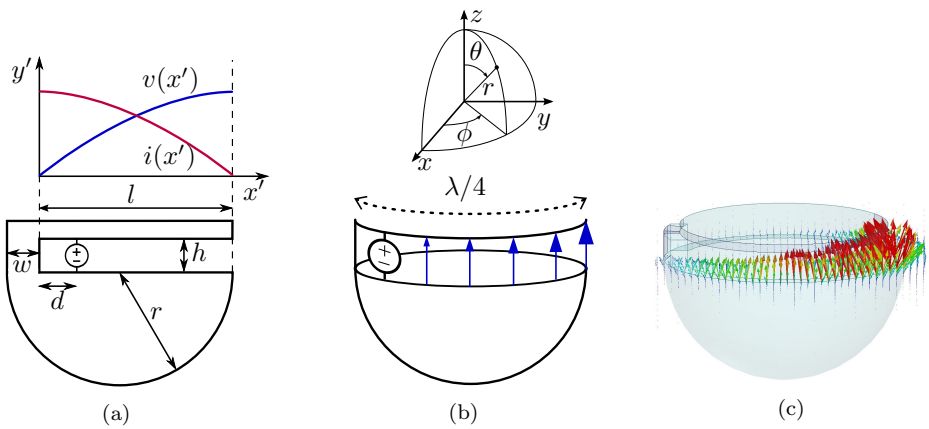

Figure 3.1. Antenna concept [P10]: (a) side view diagram; (b) perspective view diagram and coordinate system; (c) perspective view with simulated **E**-field.

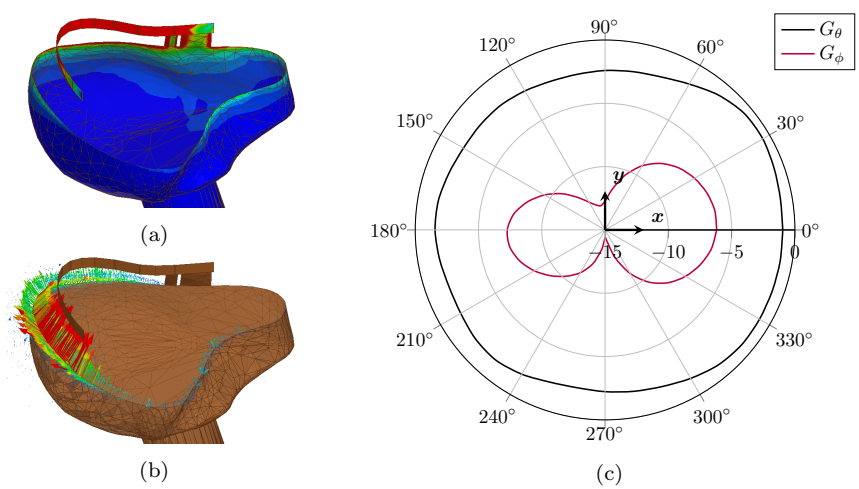

Figure 3.2. Simulation of the ear-conformal shell antenna [P10]. (a) Surface currents. (b) Simulated **E**-field on the cavity edge plane. (c) Gain pattern divided into its polarization components.

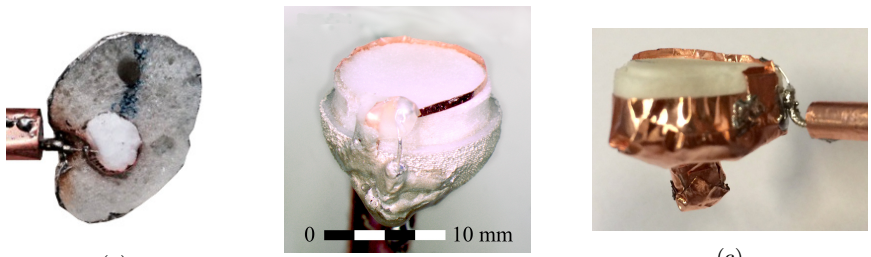

(a) (b) (c)

Figure 3.3. Antenna prototype evolution. (a) Planar feed structure, ear conformal cavity shape, implemented on styrofoam [P7]. (b) Extruding feed structure, hemispherical cavity shape, implemented on 3D-printed substrate [P8]. (c) Extruding feed structure, ear conformal shape, implemented on 3D-printed substrate [P10].

The localization of the **E**-field along the edge of the device allows to maximize the distance between the antenna and any components that may be placed inside the cavity itself. In fact, this antenna exhibits an overall convex, self-contained shape. Therefore, the space inside the shell cavity can be used to host additional MED components, such as a battery, a PCB, etc. The low field intensity within the cavity decreases the risk of unwanted coupling to the antenna. In particular, it was researched how a large metal frame, representative of a battery, may impact the antenna performance [P9]. It was observed that the impact is relatively light, especially on the device efficiency. Of course, limitations apply.

Implementation

The custom shape of the antenna poses some serious prototyping challenges. In fact, as the outer shell acts as the ground plane, it does impact the antenna performance. The shape has to be such to be fit inside the ear of a SAM head for on-body reference testing. Therefore, in order to implement the antenna, 3D printing technology has been selected. This flexible approach allows easy modification of the prototype shape, and is thus viable for future applications on real human ears. Nevertheless, due to the novelty of the technology and its scarce characterization at RF, it has been necessary to choose and characterize a specific 3D printing process. The different aspects of the manufacturing process have been analyzed and numerically modeled [P8]. This included analysis of different conductors for the implementation of the shell (i.e., aluminum foil, solid copper, multi-layered polycrystalline silver paint), determination of the feed structure (i.e., baked conductive epoxy, mechanical contact, tin soldering), and characterization of the 3D printing processes (i.e., synthetic laser or heat sintering and stereolithography) as compared to injection-molded plastics. The prototypes shown in Figure 3.3 illustrates the evolution of the technique.

After the evaluation of the different processes, a prototyping technique based on synthetic heat sintering (SHS) 3D-printed plastics and solid copper has been selected, as it exhibits contained losses and is mechanically robust and easy to handle. In particular, the dielectric frame was characterized by the use of the cavity perturbation method, with the custom-made cavity shown in Figure 3.4a [61]. The impact

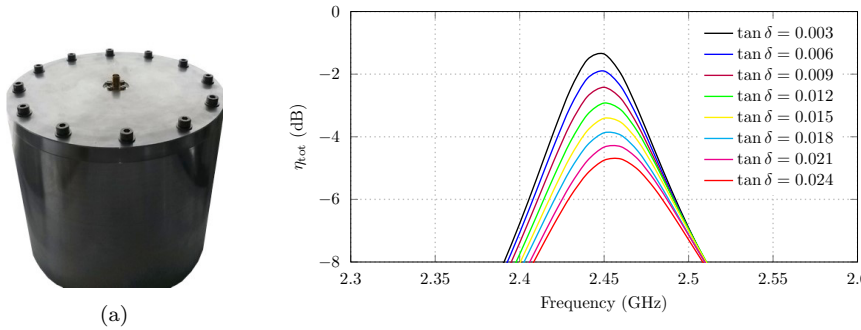

(a) (b)

Figure 3.4. (a) Cavity perturbation set-up for dielectric parameter measurements [61]. (b) Substrate's loss tangent impact on the hemispherical antenna's total radiation efficiency in free space.

Table 3.1. HI antennas review. '*' marks varying observation conditions.

reference	type	BW (MHz)	η_{tot} (%)	**P**	a (mm)	ε_{r}	$\tan\delta$	PG_{E2E} (dB)
[62]	BTE	80*	—	∥	5	1.1	0.000	−80
[63]	ITE	76	5.3	⊥	10*	6.0	0.002	−73*
[64]	ITE	10*	0.3*	⊥*	7*	3.6	0.003	−89*
[46]	BTE	240*	—	⊥	11	1.1	0.000	−50
3.3a [P7]	ITE	48	29	⊥	16.5	1.1	0.000	—
3.3b [P8]	ITE	55*	50*	⊥	7.5	2.4	0.012	—
3.3c [P10]	ITE	149	22	⊥	12	2.4	0.012	−63
3.8b [P12]	ITE	155	13.6	⊥	1	2.4	0.012	−60*

of the loss tangent of the dielectric frame on the total antenna efficiency is shown in Figure 3.4b: it can be seen how it is the dominant loss mechanism in free space. The numerical modeling based on measured material properties was proven very accurate [P8]. In synthesis, rapid prototyping allows for reliable implementation of antenna frames, once the process is characterized in terms of electrical parameters.

Performance

A summary of the antenna performance is shown in Table 3.1 and is compared to other literature results. As there is no universal agreement on the way of measure or express some of the parameters, or they can be computed but are not directly reported by the authors, the numbers shall be compared with care. This is highlighted by an asterisk '*', which denotes different observation conditions.

Overall, the performance of the shell antenna is rather remarkable. In particular, the final prototype exhibits a very large 6-dB bandwidth when worn ITE, high

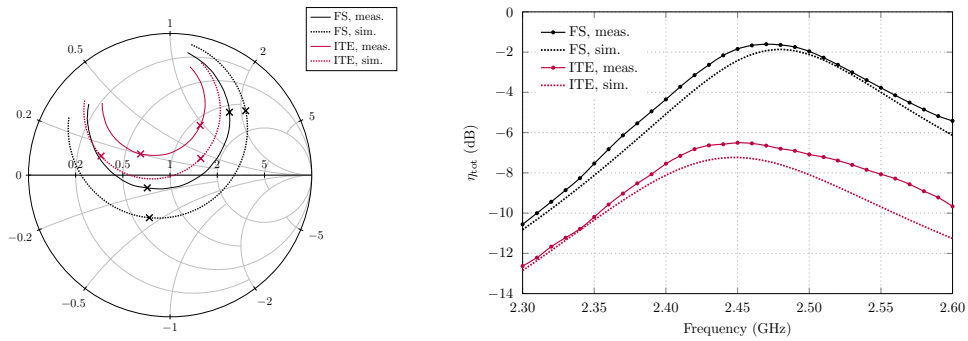

(a) (b)

Figure 3.5. Antenna simulated and measured performance, (a) reflection coefficient and (b) total radiation efficiency η_{tot}.

radiation efficiency for the application as compared to other designs, good radiation pattern and polarization characteristics, resilience to detuning and coupling to internal parts. From the Smith chart shown in Figure 3.5a it can be seen how the antenna impedance is loaded by the presence of the user body when worn, but the change magnitude is small. The total radiation efficiency shown in Figure 3.5b shows as well a really good agreement between simulation and measurements. The frequency shift of the peak efficiency due to the detuning is small. The design privileges the performance on-body, as this is the only one that is representative of the actual use of the device. The decrease in magnitude shows one of the main issues when designing ITE antennas, as they are placed deeply into the user body, which acts as an energy absorber. Nevertheless, the shell antenna grants a good efficiency performance also when worn. Both plots highlights how the numerical simulation allows for a really good modeling of the antenna, in a way that is useful to evaluate and predict the impact of design choices.

Overall, these results allows for a good E2E performance. The PG_{E2E} was measured in an anechoic shielded environment with the set-up shown in Figure 3.6a. This value was compared to both numerical and analytic results as shown in Figure 3.6b. It is worth noticing how close to the numerical simulation is the analytic calculation, computed as in [45]. The measurements confirm both the trend and the magnitude of the E2E simulated results, where the additional path loss may be rooted in the different dimensions of the SAM head with respect to the simulation model.

3.3 Body-Coupled Communications

One of the key challenges that the described antenna faces is to ensure a stable E2E link. This performance is directly affected from a multitude of factors, such as the inherent link loss, the antenna design, and the propagation environment. In particular, it was discussed in Section 2.3 how the multipath fading can increase the link PER in given environmental conditions: from a system EMC standpoint, it is desirable to transmit on a link as much stable as possible, in order to ensure a constant and reliable performance in every user case scenario. Another issue posed by

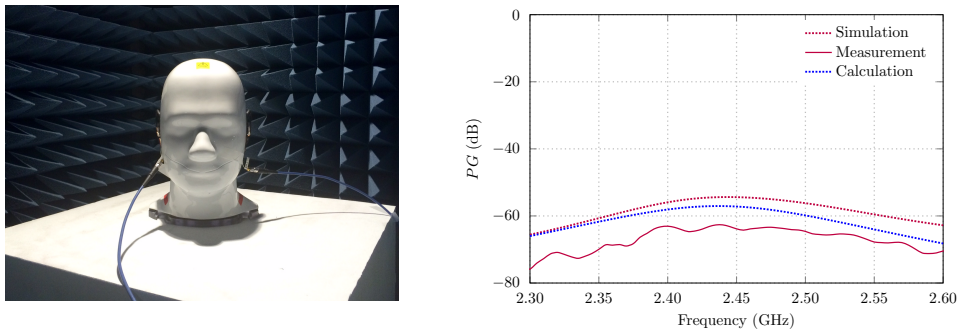

Figure 3.6. E2E performance of the shell antenna [P10]: (a) measurement set-up; (b) comparison of analytic, numerical, and measured results.

the necessity of guaranteeing the E2E link is the power demand of the RFIC, which causes additional stress to the system electronics and in particular to the PDN as discussed in Section 2.2. Nevertheless, the radio spectrum occupancy allows for other options. There are relevant propagation studies [32] that can assist in exploring and comparing among them different options. In particular, a lower power consumption is extremely appealing in MEDs, as it would both benefit the lifetime and reduce the risk on internal EMI. An additional benefit of exploring alternative frequencies for this link is that it is resilient to the increasing crowding of the 2.4 GHz ISM band. In fact, as this frequency band is exploited by more and more devices, it is an eventuality that at a future point the band crowding could start interfering with the operation of the E2E link. In order to make the link less sensitive to this source of EMI, other options may be explored in order to implement it.

Therefore, an alternative approach to the implementation of the E2E link is explored in this section. In fact, an interesting possibility is given by body-coupled communications (BCC), also called intra-body communications (IBC), where the human body itself is used as the medium to transmit the information signal. In this case the electromagnetic energy is mostly confined inside and immediately around the body, and allows for low-power operation [65, 66]. An additional benefit that may be mentioned is the fact that this kind of communications assists in protecting the privacy for the user, because the EM fields carrying the information are present only in close proximity of the body [67]. This may create possible advantages in the future from a regulatory standpoint, as privacy is an aspect of critical importance when dealing with medical devices and data. The majority of the scientific work focused so far on the investigation of BCC links in specific application contexts, that for the largest part revolve around links on the human torso and arms [68–72]. For applications such as HIs, the different application scenario demanded for an investigation of the BCC link around the human head. Therefore, a characterization of the E2E propagation channel together with an electrode system able to support the communication through it was carried out [P11].

The characterization of the electrode system and relative communication path has been experimental. The used set-up is shown in Figure 3.7a. The electrodes were

galvanic coupled to the human body and head, as the link was proven to be more stable with respect to that, which could be obtained with a capacitive coupling [73]. In particular, the latter approach does not present a uniquely define ground return path and is therefore affected by the environment where the measurements take place; for the same reason, it also varies in a greater magnitude according to the user motion. The galvanic configuration is here intended as having both electrodes in contact with the human skin, whereas with capacitive coupling it is intended that the ground electrode is left floating.

An important element to avoid the creation of artifacts in the measurements is the use of baluns. In fact, the electrode system is inherently balanced, and is therefore necessary to transition from the unbalanced reference of the VNA: otherwise, there is the risk for a conducted ground return path to mask the measured results. Further measurement precautions are the use of ferrite beads on the VNA measurement cables, as the inherently mismatched electrode system causes a high *VSWR* on them; the control of the environment (i.e., shielded, anechoic, laboratory), as according to the frequency range studied there might be external interference (e.g., AM/FM radio); it is typically necessary to verify the internal isolation among ports of the VNA, as the examined frequencies are typically close to the lower operation limit of the instrument; and to lower the noise floor by using averaging and reducing the IF bandwidth.

The measured results are shown in Figure 3.7b as a comparison between the link measured between the human ears (red curve) and a comparable distance on the human arm, as emerged from anatomical studies [74]. The latter allows for comparison with other studies [65, 68]. The measured insertion gain fall in the high end, as compared to other studies. This is at least partly influenced by the large electrode dimensions, that are squared patches with an area $A = 625$ mm^2 each and a separation between them $d = 20$ mm. It is useful to recall that the reference port is at the interface between the electrode system feed and the VNA cable: therefore, the measurements include both the system and the channel. The comparison of the insertion gain among the two scenarios is particularly interesting, as it highlights an important difference of the head environment as compared to the arm. An hypothesis based on this observation is that the high water content of the head is more conductive than the arm tissues. Beyond calling for a different modeling of the link, the value of the ear-to-ear path gain makes BCC promising for applications such as head-wearables (eye visors, smart glasses, headsets, HIs, etc.) [P11]. A future step would include measurements with active devices, so to entirely remove the possible influence of the measurement instrumentation.

3.4 Dual-frequency System Coexistence

If BCC low-frequency operation appeals for its greater power saving and link characteristics, on the other side radio operation in the 2.4 GHz ISM band presents many other advantages that cannot be traded. In particular, it is essential due to its worldwide availability, good range for both off-body and on-body links, and interoperability, as there are many well-established communication protocols operating in this band. Even though the trade-off between power consumption and range at 2.4 GHz is rather satisfactory, an overall lower-power transmission could be developed by operating two systems separately. In fact, it may be possible to save power on the critical E2E link

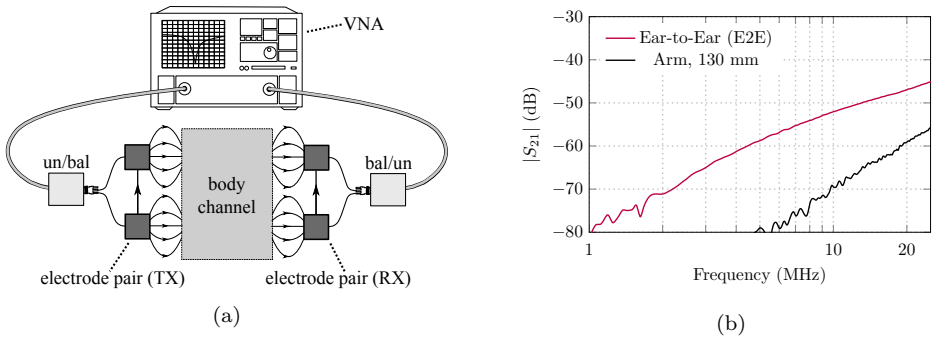

Figure 3.7. (a) Set-up for measurements of the BCC link. (b) Comparison of measurements on the head and on a arm. [P11]

developing an alternative system targeted only to this communication channel; and maintain a 2.4 GHz system for off-body communications and less demanding on-body links. Additional power savings may even come from a possible decrease of the output power of the RFIC.

An option to implement this, which is technologically mature but that is deemed limiting and overall not appealing, is to use near-field magnetic induction (NFMI). This typically requires the introduction of an external device to bridge the E2E link. This is often implemented with a loop that couples separately to the device placed at each ear. Therefore, it is necessary to address the question of how it is possible to implement an alternative system, based on body-coupled communications (BCC) and able to separate the communication links: that is, a system that grants power-efficient, reliable E2E communication via an electrode system, and a power-optimized connection to external accessories thanks to an antenna that exhibits high total radiation efficiency. In the previous sections these two functions has been studed separately. As seen, integration is often a key challenge in MEDs: in order to assess the feasibility, the technology has to be evaluated taking into consideration the actual assembly of a dual-frequency system.

A diagram of the invented combined antenna-electrode system [P12] is shown in Figure 3.8, together with the front and back picture of a custom-shaped prototype. Figure 3.8a illustrates the orientation of the **E**-field in the two operation modes: on the left is shown the main field distribution in the high-frequency (2.4 GHz) mode, analogous to the principles discussed in Section 3.2; on the right is shown the operation of the shell as a differential pair of electrodes in the low-frequency mode (megahertz-range), as discussed in Section 3.3. The prototype is then developed with a custom shape to be fit inside the ear of a SAM head.

The performance in the high-frequency operation mode is shown if Figure 3.9. Figure 3.9a and 3.9b shows the 3D on-body radiation pattern for the combined system when it is fit in the right ear of the SAM head. This highlights how the body impacts the radiation pattern, reflecting part of the energy toward the $+x$ and $+y$ directions, while it shadows the $-x$ direction where the other device is placed in the case of binaural HIs operation [75, 76]. This nearly-omnidirectional pattern is desirable to establish effective off-body or undemanding on-body links with other devices. The

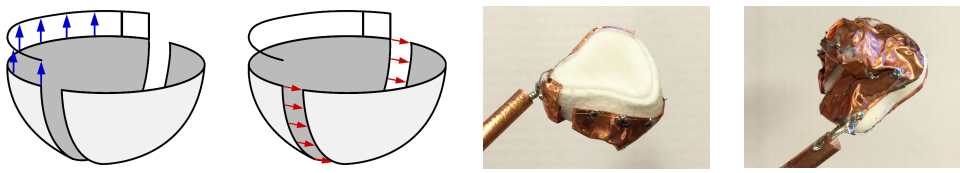

Figure 3.8. Combined antenna-electrode system [P12]. (a) Diagram, with highlighted **E**-field in the case of high-frequency operation (left) and in the case of low-frequency operation (right). (b–c) Picture of the prototype, front and back, respectively.

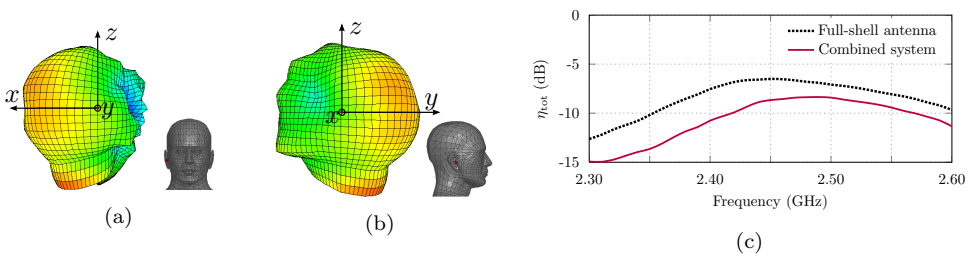

(a) (b) (c)

Figure 3.9. Radiation performance of the combined system operated in the high-frequency mode [P12]. (a–b) Measured radiation pattern when the device is placed in the right ear. (c) Total radiation efficiency η_{tot} of the combined system (red solid curve) as compared to the full-shell antenna (black dotted curve).

decrease in efficiency between the full-shell antenna described in Section 3.2, marked by the black dotted curve in Figure 3.9c, and the performance of the combined system, marked by the solid red curve in the same figure, can be justified with the reduction of the dimensions of the ground plane. In fact, the Wheeler's sphere radius decreases from $a = 12$ mm to $a' = 10$ mm, and therefore the overall electrical size of the two antennas differs. A workaround that still needs to be investigated may be the placement of RF shorting capacitors to 'stitch' the two electrodes in the high-frequency mode, while maintaining them electrically separate in the low-frequency mode.

The ear-to-ear link is enabled by the low-frequency operation mode. The simulated **E**-field distribution on a plane crossing the ears is shown in Figure 3.10a. As known, differently from what happens at 2.4 GHz where the main energy propagation happens around the head in form of creeping waves [42, 76], the potential difference is carried by the human body to reach the second electrode pair. It can be seen in Figure 3.10b how the magnitude of the path gain is lower than what was studied in Section 3.3. This is because the actual application puts a strong constraint on the electrode shape and separation. It is possible to notice how the simulation is effective in predicting both the trend and the magnitude of the link gain.

3.5 Summary

In this chapter a novel wearable shell antenna based on a cavity-backing principle is introduced. The main antenna parameters are translated into requirements for on-body applications, and in the specific for HIs. The link between the requirements and

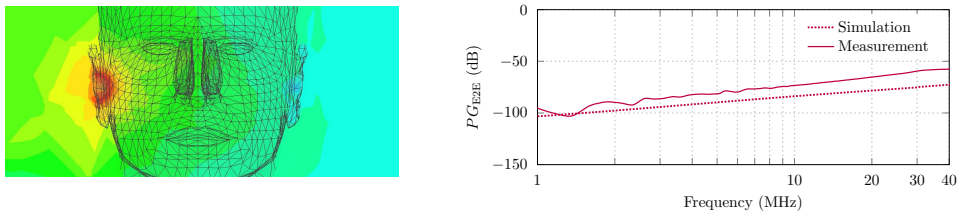

(a) (b)

Figure 3.10. E2E performance of the combined antenna-electrode system [P12]: (a) simulated **E**-field across the homogeneous human head model; (b) comparison of numerical and measured results.

the design choices and the way those are reflected on the final antenna parameters is highlighted.

The antenna design principle is explained for the case of an hemispherical ground plane and an IFA arm extruding above the cavity edge. It is shown that the cavity can then be shaped without loss of generality in a way conformal to the shape of the concha and outer ear canal of a human ear. The ear shape used, developed according to anatomical measurements, allows for measurements on a SAM head with RF ear for characterization of the on-body performance. The importance of developing EMC considerations early in the design stage is highlighted. The evolution of the antenna prototyping technique is described. In particular, it is highlighted how a modern 3D printing process can be characterized for effective use with electromagnetic numerical simulation tools. The performance of the antenna was thoroughly measured in free space and on-body and compared to other results available in literature. In particular, the key parameter PG_{E2E} is studied by the mean of analytic and numeric simulations and measurements.

Given the critical importance of the E2E link and the possible future impact of EMI on its reliability, the possibility of using an electrode system to support it is highlighted. The use of BCC would allow to reduce the stress on the system electronics and mitigate EMI issues caused by the high power demand of the 2.4 GHz link. Therefore, it is proposed the first characterization of BCC around the human head, which highlighted a noticeable difference with respect to the conventional models available in the literature that are based on propagation links around the human torso and arms. The higher values of the path gain around the head environment looked promising for an effective implementation in a HI system.

Therefore, a combined system that would allow both kinds of communication was invented and proposed. The two operation modes are EMC-friendly thanks to their frequency separation. It is shown how the decrease in efficiency caused by the electrode system introduction in the shell antenna design is compensated by the possibility of using the electrode pair to establish the demanding E2E link. This solution allows for an overall lower power consumption, decreasing the risk of the device generating EMI, while is able to establish both off-body and on-body links.

4

Conclusion

The impact of EMI in miniature complex devices was investigated in this work, and a set of actions in order to mitigate it was undertaken. The potential of improving the general EM environment for MEDs and HIs was explored in different directions, spanning from intra-device sensitivity and self-jamming issues to inter-device system design.

The solutions must be extremely compact physically- and electrically-wise [P1]. In addition, they must be easy to integrate in a traditional PCB design, and efficiently suppress the target radiation in all directions [P2]. Furthermore, they need to have high selectivity, act on a source located within a given area, and do not disturb other integrated transmission lines carrying, e.g., digital signals that share the same physical space on the PCB. A strongly-subwavelength structure inspired by metamaterial research was developed and integrated in a PCB. This structure was proven able to couple effectively to interference sources placed in its near field and suppress the narrowband spurious radiation coming from them. The structure is directional, and hence preserves the SI performance when intelligent routing is applied—also across the structure itself [P3]. It was also shown that it is possible to exploit the properties of similar metamaterial-inspired structures to shrink the antenna dimensions while providing rejection of interference coupled to the antenna itself [P4].

A controlled intra-system EM environment allowed for a study of the noise figure in a traditional receiving chain. This highlighted the potential for an ultra-low-power, compact LNA to decrease the PER along the E2E channel transmission. It was found that the LNA supplied from a low voltage can be implemented with only a few discrete components, while being able to improve the receiver sensitivity [P5]. As the LNA is to be operated in the context of an on-body device, which is subject to antenna detuning due to the user interaction, the impact of the Q factor of the input matching network was studied. It was found that a high-Q profile can further deteriorate the performance of the whole system when the LNA is also present [P6].

Internal EM noise is not the only issue that needs to be taken into account by devices that are designed to communicate with each other. A careful system architecture starts from an antenna design that is able to address the specific challenges of the EM environment where it is intended to operate. This consideration started the design and development of a novel antenna for binaural HIs: in fact, the antenna uses a conductive cavity to maximize its volume and efficiency, while shielding the user body from the radiation [P7]. The antenna exhibits optimal radiation pattern and polarization, high efficiency, and large impedance bandwidth [P10]. Due to the

modern prototyping process (3D-printing) that was investigated to implement it [P8], it was found how numerical simulations can be effectively used by the designers to predict the prototype behavior from early stage concept phase—and hence start acting immediately on potential EMC issues. Due to the design that concentrates the electrical fields at the edge of the cavity, the antenna is resilient to loss introduced by metallic parts in its volume such as the battery or a PCB assembly [P9]. This de-coupling allows the antenna to be less sensitive to possible interference problems originated in the device electronics.

With regards to EMI generated outside the device, consistent future spectrum crowding may hinder the reliable functioning of medical devices communications, especially in the 2.4 GHz ISM band, which is widely used world-wide. Hence, a study of a link that operates through electrodes at a few megahertz was outlined in that particular environment that is the human head—with consideration for the user own EM environment [P11]. The way actual electrodes can be placed in a small device was studied. A unique, joint system had to be developed in order not to interfere with the operations at 2.4 GHz. In order to ensure an interference-free E2E link and to improve the other on-body and off-body links, the possibility to place the electrodes in conjunction with the novel antenna design introduced for optimal EM performance was studied [P12].

To summarize, both intra- and inter-system EM noise problems were taken into account, and multiple strategies to deal with EMI in such applications were invented. It is the hope that this work will continue to inspire the research in techniques to manage the electromagnetic interference in compact and miniature electronic devices in a world of size-shrinking electronics, and succeeded in stressing the need of a full-system approach to the matter.

Bibliography

[1] B. C. Kirkwood, S. A. Hallenbeck, and T. Stender, "How can wireless data exchange in hearing instruments contribute to binaural hearing?", *Hearing Review*, vol. 19, no. 10, pp. 52–55, 2012.

[2] B. Archambeault, "Review of printed-circuit-board level EMI/EMC issues and tools", *IEEE Trans. Electromagn. Compatibility*, vol. 52, no. 2, pp. 455–461, 2010.

[3] S. Shahparnia and O. M. Ramahi, "Electromagnetic interference (EMI) reduction from printed circuit boards (PCB) using electromagnetic bandgap structures", *IEEE Trans. Electromagn. Compatibility*, vol. 46, no. 4, pp. 580–587, 2004.

[4] Z. Yu, X. Dong, J. Mix, K. Slattery, and J. Fan, "Analysis of noise coupling from printed circuit board to shielding enclosure", in *2008 Elect. Performance Electron. Packag. (EPEP)*, 2008, pp. 149–152.

[5] R. Abhari and G. V. Eleftheriades, "Metallo-dielectric electromagnetic bandgap structures for suppression and isolation of the parallel-plate noise in high-speed circuits", *IEEE Trans. Microw. Theory Techn.*, vol. 51, no. 6, pp. 1629–1639, 2003.

[6] "American national standard dictionary of electromagnetic compatibility (EMC) including electromagnetic environmental effects (E3)", *ANSI C63.14-2014 (Revision of ANSI C63.14-2009)*, pp. 1–76, Dec. 2014.

[7] X. Chen, N. Chavannes, G. Ng, Y. Tay, and J. Mosig, "Analysis and design of mobile device antenna–speaker integration for optimum over-the-air performance", *IEEE Antennas Propag. Mag.*, vol. 57, no. 1, pp. 97–109, Feb. 2015.

[8] A. Abidi, "Direct-conversion radio transceivers for digital communications", *IEEE J. Solid-State Circuits*, vol. 30, no. 12, pp. 1399–1410, 1995.

[9] B. Razavi, "Design considerations for direct-conversion receivers", *IEEE Trans. Circuits Syst. II, Analog Digit. Signal Process.*, vol. 44, no. 6, pp. 428–435, 1997.

[10] S. H. Kvist, S. Özden, J. Thaysen, and K. B. Jakobsen, "Improvement of the ear-to-ear path gain at 2.45 GHz using parasitic antenna element", in *Proc. of 6th European Conf. Antennas Propag. (EuCAP)*, vol. 2, 2011, pp. 944–947.

[11] M. Kim, K. Koo, C. Hwang, *et al.*, "A compact and wideband electromagnetic bandgap structure using a defected ground structure for power/ground noise suppression in multilayer packages and PCBs", *IEEE Trans. Electromagn. Compatibility*, vol. 54, no. 3, pp. 689–695, Jun. 2012.

[12] O. M. Ramahi, V. Subramanian, and B. Archambeault, "A simple finite-difference frequency-domain (FDFD) algorithm for analysis of switching noise in printed circuit boards and packages", *IEEE Trans. Adv. Packag.*, vol. 26, no. 2, pp. 191–198, 2003.

[13] I. Claesson and A. Rossholm, "Notch filtering of humming GSM mobile telephone noise", in *5th Int. Conf. Information Communications and Signal Processing*, 2005, pp. 1320–1323.

[14] M. Skopec, H. Boom, C. Robinson, *et al.*, "Hearing aid electromagnetic interference from digital cellular telephones", in *Proc. 18th Annu. Int. Conf. IEEE Engineering in Medicine and Biology Society*, vol. 1, 1997, pp. 409–410.

[15] "American national standard methods of measurement of compatibility between wireless communications devices and hearing aids", *C63.19-2011 (Revision of ANSI C63.19-2007)*, May 2011.

[16] P. G. Huray, *The foundations of signal integrity.* Wiley, IEEE Press, 2010.

[17] M. B. Hyrup, "Probes for magnetic near-field measurements", Bachelor Thesis, DTU Technical University of Denmark, 2013.

[18] M. M. Bait-Suwailam and O. M. Ramahi, "Ultrawideband mitigation of simultaneous switching noise and EMI reduction in high-speed PCBs using complementary split-ring resonators", *IEEE Trans. Electromagn. Compatibility*, vol. 54, no. 2, pp. 389–396, Apr. 2012.

[19] J. Qin, O. M. Ramahi, and V. Granatstein, "Novel planar electromagnetic bandgap structures for mitigation of switching noise and EMI reduction in high-speed circuits", *IEEE Trans. Electromagn. Compatibility*, vol. 49, no. 3, pp. 661–669, 2007.

[20] F. De Paulis and L. Raimondo, "Compact configuration for common mode filter design based on planar electromagnetic bandgap structures", *IEEE Trans. Electromagn. Compatibility*, vol. 54, no. 3, pp. 646–654, 2012.

[21] J. Baena and J. Bonache, "Equivalent-circuit models for split-ring resonators and complementary split-ring resonators coupled to planar transmission lines", *IEEE Trans. Microw. Theory Techn.*, vol. 53, no. 4, pp. 1451–1461, 2005.

[22] R. Marqués, F. Medina, and R. Rafii-El-Idrissi, "Role of bianisotropy in negative permeability and left-handed metamaterials", *Phys. Rev. B*, vol. 65, no. 14, p. 144 440, Apr. 2002.

[23] P. D. Imhof, R. W. Ziolkowski, and J. R. Mosig, "Highly subwavelength unit cells to achieve epsilon negative (ENG) metamaterial properties", in *IEEE Antennas Propag. Soc. Int. Symp. (APSURSI)*, vol. 2, 2006, pp. 1927–1930.

[24] A Erentok and R. Ziolkowski, "Metamaterial-inspired efficient electrically small antennas", *IEEE Trans. Antennas Propag.*, vol. 56, no. 3, pp. 691–707, 2008.

[25] R. W. Ziolkowski, P. Jin, and C.-C. Lin, "Metamaterial-inspired engineering of antennas", *Proc. IEEE*, vol. 99, no. 10, pp. 1720–1731, 2011.

[26] C. C. Lin, P Jin, and R. W. Ziolkowski, "Single, dual and tri-band-notched ultrawideband (UWB) antennas using capacitively loaded loop (CLL) resonators", *IEEE Trans. Antennas Propag.*, vol. 60, no. 1, pp. 102–109, 2012.

[27] R. W. Ziolkowski and A. D. Kipple, "Causality and double-negative metamaterials", *Phys. Rev. E*, vol. 68, no. 22, p. 026 615, Aug. 2003.

[28] D. Pozar, *Microwave Engineering*. John Wiley & Sons, 2005.

[29] J. Liang and H. D. Yang, "Radiation characteristics of a microstrip patch over an electromagnetic bandgap surface", *IEEE Trans. Antennas Propag.*, vol. 55, no. 6, pp. 1691–1697, 2007.

[30] H. Mosallaei and K. Sarabandi, "Antenna miniaturization and bandwidth enhancement using a reactive impedance substrate", *IEEE Trans. Antennas Propag.*, vol. 52, no. 9, pp. 2403–2414, 2004.

[31] K. H. Kim and J. E. Schutt-ainé, "Design of EBG power distribution networks with VHF-band cutoff frequency and small unit cell size for mixed-signal systems", *IEEE Microw. Wireless Components Letters*, vol. 17, no. 7, pp. 489–491, 2007.

[32] P. S. Hall *et al.*, "Antennas and propagation for on-body communication systems", *IEEE Antennas Propag. Mag.*, vol. 49, no. 3, pp. 41–58, 2007.

[33] H. Liu and J. L. Nielsen, "An efficient interference mitigation method for wireless hearing instruments network", in *IEEE Int. Symp. Person. Indoor Mobile Radio Commun. (PIMRC)*, 2012, pp. 620–624.

[34] Z. Li, L. Chen, and H. Zhang, "Design and optimization of CMOS LNA with ESD protection for 2.4 GHz WSN application", *Journal of Semiconductors*, vol. 32, no. 10, 2011.

[35] J. L. Gonzalez, H. Solar, I. Adin, D. Mateo, and R. Berenguer, "A 16-kV HBM RF ESD protection codesign for a 1-mW CMOS direct conversion receiver operating in the 2.4-GHz ISM band", *IEEE Trans. Microw. Theory Techniques*, vol. 59, no. 9, 2011.

[36] J.-M. Wu and Y.-T. Lin, "A solar-powered 2.4-GHz LNA RFIC", *Microw. Optical Technology Letters*, vol. 55, no. 10, pp. 2377–2380, 2013.

[37] F. Belmas, F. Hameau, and J. Fournier, "A 1.3mW 20dB gain low power inductorless LNA with 4 dB noise figure for 2.45 GHz ISM band", in *IEEE Radio Frequency Integrated Circuits Symposium*, 2011.

[38] R. Fiorelli, F. Silveira, and E. Peralías, "MOST moderate-weak-inversion region as the optimum design zone for cmos 2.4-GHz CS-LNAs", *IEEE Trans. Microw. Theory Techniques*, vol. 62, no. 3, pp. 556–566, 2014.

[39] Z. Li *et al.*, "A 2.4 GHz ultra-low-power current-reuse CG-LNA with active Gm-boosting technique", *IEEE Microwave and Wireless Components Letters*, vol. 4, no. 5, pp. 348–350, 2014.

[40] V. Aaron *et al.*, "A subthreshold low-noise amplifier optimized for ultra-low-power applications in the ISM band", *IEEE Trans. Microw. Theory Techniques*, vol. 56, no. 2, pp. 286–292, 2008.

[41] P. Popovski, H. Yomo, and R. Prasad, "Dynamic adaptive frequency hopping for mutually interfering wireless personal area networks", *IEEE Transactions on Mobile Computing*, vol. 5, no. 8, pp. 991–1003, 2006.

[42] S. H. Kvist, "Antennas and propagation for body-centric wireless communications", Ph.D. Thesis, DTU Technical University of Denmark, 2013.

[43] Federal Communications Commission, "RF exposure procedures and equipment authorization policies for mobile and portable devices", version 6, *447498 D01 General RF Exposure Guidance*, Oct. 2015.

[44] Bluetooth Special Interest Group, "Bluetooth low energy regulatory aspects", version 10, Apr. 2011.

[45] S. H. Kvist, J. Thaysen, and K. Jakobsen, "Ear-to-ear on-body channel model for hearing aid applications", *IEEE Trans. Antennas Propag.*, vol. 63, no. 1, pp. 344–352, Jan. 2015.

[46] S. H. Kvist, J. Thaysen, and K. B. Jakobsen, "Design and measurement of a 2.45 GHz on-body antenna optimized for hearing instrument applications", in *34th Annu. Antenna Meas. Techn. Assoc. Symp. (AMTA)*, 2012, pp. 33–37.

[47] R. Chandra and A. J. Johansson, "A link loss model for the on-body propagation channel for binaural hearing aids", *IEEE Trans. Antennas Propag.*, vol. 61, no. 12, pp. 6180–6190, 2013.

[48] T. Alves, B. Poussot, and J.-M. Laheurte, "Analytical propagation modeling of ban channels based on the creeping-wave theory", *IEEE Trans. Antennas Propag.*, vol. 59, no. 4, pp. 1269–1274, 2011.

[49] A. Vasylchenko, C. Hennemann, and R. Dubrovka, "Characterization of the ear-to-ear propagation channel using microstrip dipole antennas", in *Proc. 8th Int. Conf. Antenna Theory Techn. (ICATT)*, 2011, pp. 202–204.

[50] S. Best, "Integrated antennas for wireless personal communications", in *Modern Antenna Handbook*, C. A. Balanis, Ed., John Wiley & Sons, Inc., 2007, pp. 475–528.

[51] Y. Rahmat-Samii, J. Guterman, A. A. Moreira, and C. Peixeiro, "Integrated antennas for wireless personal communications", in *Modern Antenna Handbook*, C. A. Balanis, Ed., John Wiley & Sons, Inc., 2007, pp. 1077–1142.

[52] A. D. Yaghjian and S. R. Best, "Impedance, bandwidth, and q of antennas", *IEEE Trans. Antennas Propag.*, vol. 53, no. 4, pp. 1298–1324, 2005.

[53] CTIA Certification, *Test plan for wireless device over-the-air performance*, v3.3.2, Sep. 2014.

[54] C. Balanis, *Antenna theory: Analysis and design*, 3rd. John Wiley, 2005.

[55] M. C. Huynh and W. Stutzman, "Ground plane effects on planar inverted-F antenna (PIFA) performance", *IEE Proc. Microw. Antennas Propag.*, vol. 150, no. 4, pp. 209–213, 2003.

[56] D. Liu and B. Gaucher, "The inverted-F antenna height effects on bandwidth", in *Proc. IEEE Antennas Propag. Symp.*, vol. 2, 2005, pp. 367–370.

[57] C. R. Cockrell, "The input admittance of the rectangular cavity-backed slot antenna", *IEEE Trans. Antennas Propag.*, vol. 24, no. 3, pp. 288–294, 1976.

[58] N. Haga, M. Takahashi, K. Saito, and K. Ito, "A cavity-backed slot antenna for on-body BAN devices", in *Proc. IEEE Int. Workshop Antenna Technol. (IWAT)*, 2008, pp. 510–513.

[59] H. Wheeler, "The radiansphere around a small antenna", *Proc. IRE*, vol. 47, no. 8, pp. 1325–1331, 1959.

[60] M. Jensen and Y. Rahmat-Samii, "Em interaction of handset antennas and a human in personal communications", *Proc. IEEE*, vol. 83, no. 1, pp. 7–17, 1995.

[61] T. N. Bjerre, "Constitutive parameter measurement system", Master Thesis, DTU Technical University of Denmark, 2015.

[62] N. Kammersgaard, S. H. Kvist, J. Thaysen, and K. Jakobsen, "In-the-ear spiral monopole antenna for hearing instruments", *Electronics Letters*, vol. 50, no. 21, pp. 1509–1511, Oct. 2014.

[63] W. H. Yatman, L. K. Larsen, S. H. Kvist, J. Thaysen, and K. B. Jakobsen, "In-the-ear hearing-instrument antenna for ISM-band body-centric ear-to-ear communications", in *Loughborough Antennas Propag. Conf. (LAPC)*, 2012.

[64] L. Huitema, S. Sufyar, C. Delaveaud, and R. D'Errico, "Miniature antenna effect on the ear-to-ear radio channel characteristics", in *Proc. of 6th European Conf. Antennas Propag. (EuCAP)*, 2012, pp. 3402–3406.

[65] K. Ito, N. Haga, M. Takahashi, and K. Saito, "Evaluations of body-centric wireless communication channels in a range from 3 MHz to 3 GHz", *Proc. IEEE*, vol. 100, no. 7, pp. 2356–1363, 2012.

[66] K. Ito, "Compact dual-mode antenna for body-centric wireless communications", in *Proc. European Conf. Antennas Propag. (EuCAP)*, 2015.

[67] M. Fujikawa and M. Nishigaki, "A study of prevention for social engineering attacks using real/fake organization's uniforms: application of radio and intra-body communication technologies", *Proceedings of the 6th International Conference on Availability, Reliability and Security (ARES 2011)*, pp. 597–602, 2011.

[68] T. C. W. Schenk, N. S. Mazloum, L. Tan, and P. Rutten, "Experimental characterization of the body-coupled communications channel", *IEEE International Symposium on Wireless Communication Systems (ISWCS 2008)*, pp. 737–742, 2008.

[69] N. Haga and K. Ito, "Equivalent circuit of intra-body communication channels based on a lossy conductor model", *IEEE Antennas and Propagation Society International Symposium (Digest)*, pp. 672–675, 2012.

[70] K. Fujii, M. Takahashi, and K. Ito, "Electric field distributions of wearable devices using the human body as a transmission thannel", *IEEE Transactions on Antennas and Propagation*, vol. 55, no. 7, pp. 2080–2087, 2007.

[71] K. Partridge, B. Dahlquist, A. Veiseh, *et al.*, "Empirical measurements of intrabody communication performance under varied physical configurations", *UIST (User Interface Software and Technology): Proceedings of the ACM Symposium*, pp. 183–190, 2001.

[72] H. Baldus, S. Corroy, A. Fazzi, K. Klabunde, and T. Schenk, "Human-centric connectivity enabled by body-coupled communications", *IEEE Communications Magazine*, vol. 47, no. 6, pp. 172–178, 2009.

[73] M. Amparo Callejon, D. Naranjo-Hernandez, J. Reina-Tosina, and L. M. Roa, "A comprehensive study into intrabody communication measurements", *IEEE Transactions on Instrumentation and Measurement*, vol. 62, no. 9, pp. 2446–2455, 2013.

[74] S. Pehrson, S. H. Kvist, K. B. Jakobsen, and J. Thaysen, "Morphological investigation of the differences on the ear-to-ear path gain and the packet loss at 2.45 GHz", *34th Annu. Antenna Meas. Techn. Assoc. Symp. (AMTA)*, pp. 43–48, 2012.

[75] N. P. I. Kammersgaard, S. H. Kvist, J. Thaysen, and K. B. Jakobsen, "Pinna model for hearing instrument applications", in *Loughborough Antennas Propag. Conf. (LAPC)*, 2014, pp. 141–143.

[76] N. P. I. Kammersgaard, S. H. Kvist, S. Özden, J. Thaysen, and K. B. Jakobsen, "Body-worn antennas for body-centric wireless communications", in *Loughborough Antennas Propag. Conf. (LAPC)*, 2014.

Paper 1

"Metamaterial-inspired Near-field Resonant Parasitic Structure for Directional Suppression of Narrow-band EMI/RFI in Compact Systems"

A. Ruaro, J. Thaysen, and K. B. Jakobsen

[P1] A. Ruaro, J. Thaysen, and K. B. Jakobsen, "Metamaterial-inspired near-field resonant parasitic structure for directional suppression of narrow-band EMI/RFI in compact systems", in *Proceedings of the Antennas and Propagation Symposium / International Union of Radio Science (AP-S/URSI)*, 2013.

Metamaterial-inspired Near-field Resonant Parasitic Structure for Directional Suppression of Narrow-band EMI/RFI in Compact Systems

Andrea Ruaro*[1,2], Jesper Thaysen[2], and Kaj B. Jakobsen[1]

[1] DTU Elektro, Technical University of Denmark, DK-2800 Lyngby
[2] GN ReSound A/S, Lautrupbjerg 7, DK-2750 Ballerup, Denmark

This paper describes the application of an electrically small, metamaterial-inspired, near-field resonant parasitic (NFRP) element in a nearly space-less design for suppression of narrowband radio-frequency interference (RFI) and its higher-order harmonics. The design of the NFRP structure is inspired by results presented in the existing literature. The possibility of using it as a notch filter as a design integrated in a Printed Circuit Board (PCB) and its advantages over known solutions like electromagnetic bandgap (EBG) or defected ground (DGS) structures are discussed; the results for different orientations are shown. The coupling mechanism of the structure to transmission lines is briefly presented.

To comply with the EMC regulations worldwide is of utmost importance for the diffusion of electronic products. Designers are nowadays facing new issues due to factors like increased clock speed, coexistence of audio and analogue systems, shrinking of PCB dimensions, etc. In most cases, especially for devices where the space is critical as are hand-held terminals or medical implants, there is no room to apply traditional solutions as proper grounding, filtering, and shielding. Furthermore, there is an interest to attenuate a single frequency and its higher-order harmonics: a problem arises when a transmission line needs filtering for a frequency that is very close to the operating frequency.

The filtering effect is here achieved due to the resonant behavior of the NFRP element. The results are obtained by the use of FEM-based simulations. The design of the NFRP element is based on the existing literature, and in particular on the work of Ziolkowski *et al.* The structure is implemented directly in the substrate, in a layer between the signal tracks and the ground (or power) layer. Two orientations of the structure are analyzed, and the importance of the directionality in complex environments is highlighted. An electric-coupled electric-inspired element is shown here and is able to provide narrowband attenuation of a signal travelling on a microstrip line of more than 10 dB for one orientation, while it is 2 dB only when the structure is rotated by 90°.

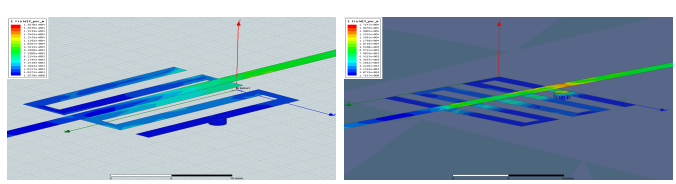

Paper 2

"Mitigation of Unwanted Forward Narrow-band Radiation from PCBs with a Metamaterial Unit Cell"

A. Ruaro, J. Thaysen, and K. B. Jakobsen

[P2] A. Ruaro, J. Thaysen, and K. B. Jakobsen, "Mitigation of unwanted forward narrow-band radiation from PCBs with a metamaterial unit cell", in *Proceedings of the European Microwave Conference (EuMC)*, 2013.

Mitigation of Unwanted Forward Narrow-band Radiation from PCBs with a Metamaterial Unit Cell

Andrea Ruaro*†, Jesper Thaysen*, and Kaj B. Jakobsen†

*GN ReSound A/S, Lautrupbjerg 7, DK-2750 Ballerup, Denmark
†Department of Electrical Engineering, Technical University of Denmark, DK-2800 Lyngby, Denmark

***Abstract*—Mitigation of EMI from a PCB is obtained through the use of a metamaterial unit cell. The focus is on the reduction of narrow-band radiation in the forward hemisphere when the resonant element is etched on a layer located between the source of radiation and the ground plane. As opposed to previous publications in the literature, the aim of this work is the application of a filter to scattered radiation, generalizing the former characterizations based solely upon transmission lines' insertion loss. The radiating area accounts for traces and components placed on the top layer of a PCB and is simulated via a patch antenna. The study exhibits how the radiation pattern and the electric field on the patch antenna change within and outside the resonance bandwidth of the parasitic element. An EMC assessment provides experimental verification of the operating principle.**

***Index Terms*—Metamaterial filters; planar filters; electromagnetic interference (EMI); electromagnetic compatibility (EMC); printed circuit boards (PCB)**

I. Introduction

The traces on a printed circuit board (PCB) can act as radiation sources, and thus be at the origin of electromagnetic interference (EMI) problems. The primary consequence of this is products that interferes with nearby devices and ultimately that cannot be commercialized. In high-density, complex environments where radio and digital subsystems coexist, high-speed traces necessarily cross the RF circuitry. Most of these devices are severely space-constrained — e.g., hearing aids, mobile phones and handsets, medical implants, and the like.

In this context there is an interest in further suppressing the narrow-band EMI generated by RFICs, like power amplifier (PA) harmonics or local oscillator (LO) leakage [1], [2], in order to fulfil the EMC regulations. In particular, when the unwanted frequency is close to that which a system is intended to operate at, traditional techniques (e.g., decoupling capacitors) are not an effective solution if the desired signal has to be safeguarded. When the radiation source is placed on the top layer, or is anyway not shielded by, e.g., a power plane, the action traditionally takes place on the radiation path placing extra shields. Additional shields are costly, of complex implementation production-wise, and in particular can seriously compromise the functioning of small antennas nearby, as in the case of hearing aids.

Among filter techniques, electromagnetic bandgap (EBG) structures [3]–[6] cannot be used in space-constrained devices due to their dimensions, not even in a planar implementation. The use of mu-negative (MNG) resonators as filters for transmission lines was explored in the past [7], but coupling to microstrip lines demands complementary designs, e.g., complementary split-ring resonators, due to the direction of the fields necessary to excite the resonators [8]. Nevertheless, this kind of complementary designs [9] or in general defected ground structures (DGS) affects the currents running on the PCB, degrading the signal integrity performance and potentially creating EMC problems. A further performance worsening is even possible when the PCB is connected to a $\lambda/4-$monopole antenna that ideally requires a solid ground plane. The epsilon-negative (ENG) structure used here was introduced in [10] and it has been used in the literature mostly to enhance the radiation characteristics of electrically-small antennas [11], [12].

Therefore the issue is to reduce the radiation in the forward hemisphere without acting directly on the radiation path. For this purpose, this work makes use of a metamaterial-inspired near-field resonant parasitic (NFRP) element etched in an inner layer. The implementation allows to mitigate narrow-band EMI in electrically- and physically-small devices, where the rejection frequency is close to the signal frequency, the actual radiation source is unknown within a certain area, and where to preserve a solid ground is necessary to satisfy the antenna needs. A drawback of the implementation is the dedicated use of a part of an inner layer, which results in an increased PCB design complexity.

The article is organized as follows. Section II defines the problem geometry and describes the physical mechanism that the device is grounded on. Section III provides the full design data, as well as the simulation results and discussion. Section IV characterizes the effects of the structure on the EMC performance. Finally, Section V summarizes the findings.

II. Geometry and Theory

The stack-up, shown in Fig. 1, is on three layers: on the top layer there is a radiation source, namely a number of PCB traces randomly oriented within a certain area; on the inner

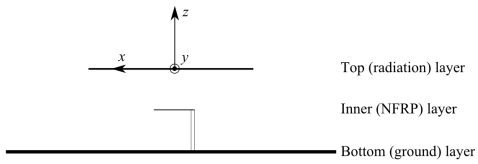

Fig. 1: PCB side view showing the radiation layer, the layer where the filtering structure can be implemented, and the ground plane.

layer there is a near-field resonant parasitic (NFRP) element connected to ground through a via; the third layer is a solid ground plane.

The forward hemisphere is defined with the coordinate system centred at the radiation source plane with the z axis oriented normal to the surface.

A patch antenna model is used to account for the PCB lines acting as radiation sources. This choice allows currents to run freely (and then be visualized) on a 2-D conductive surface, i.e., beyond the boundaries of a single line.

The NFRP element consists of a closely meandered line acting as an ENG metamaterial unit cell. It is chosen here for its marked sub-wavelength dimensions. It has been preferred over a MNG metamaterial unit cells due to its effective coupling mechanism to the target sources under examination, and to exploit the potential of directional filtering [13].

As known from the cavity model [14], the main radiation sources in a patch antenna are two equivalent magnetic dipoles along the patch width, with the electric field oriented normal to the ground plane. The NFRP structure is excited by such a field and drives the radiation to ground through the via connection. The resonator is thus placed in close proximity to one of the radiating slots in order to maximize the coupling. Even though most of the radiation comes from these equivalent sources, they are not the only parts of the patch actually radiating: the antenna is thus considered representative of scattered radiation, where the two radiating slots have dominant behaviour. This can easily recall the scenario of a PCB, with a microstrip line radiating as the major contributor and any other, differently oriented, acting as secondary contributors.

The structure fulfils the implementation requirements, namely to be physically- and electrically-small, to leave substantially unaltered the ground plane, and to have a narrow-frequency transition band.

III. Simulation Set-up and Results

A. Set-up

The geometry is shown in Fig. 2. The circuit is simulated with Ansys HFSS [15] and fabricated on a FR-4 substrate with a dielectric constant $\varepsilon_{\mathrm{r}} = 4.4$. The height of the inner layer over the ground layer is $h_{\mathrm{in}} = 0.8$ mm, while the height of the top layer with respect to the same reference is $h_{\mathrm{top}} = 1.6$ mm. The ground plane dimensions are 150 mm $\times$ 150 mm.

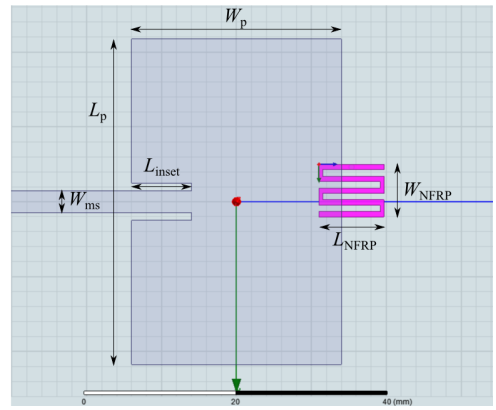

Fig. 2: Top view, with geometry outlined.

TABLE I: Patch antennas dimensions (in mm)

	2.45 GHz	2.85 GHz
W	43.5	37.4
L	28.0	24.2
W_{ms}	3.0	3.0
L_{inset}	8.0	7.0

The metallization is made of copper with thickness $t = 35$ μm.

Two patch antennas are designed to account for two signals with different frequencies. The desired signal frequency is chosen at 2.45 GHz, so that it falls within the ISM band, while the rejection frequency is chosen to be 2.85 GHz. The latter is the frequency at which the NFRP element is resonant. The patch antenna dimensions can be found in Table I. The feed is via a recessed microstrip transmission line.

The NFRP element counts 5 strips and 4 gaps. Its overall dimensions are $L_{\mathrm{NFRP}} = 8.67$ mm $\times$ $W_{\mathrm{NFRP}} = 7.04$ mm, with a microstrip width of $W_{\mathrm{NFRP,ms}} = 0.72$ mm and a gap width of $W_{\mathrm{NFRP,gap}} = 0.86$ mm.

B. Results

The goal of the results presented in this section is twofold: first, to show that the NFRP structure effectively suppress the interference emitted by a radiation source in the forward hemisphere; and second, to examine the effect that the same structure has on a frequency close to the one that has to be cancelled.

The two patch antennas have similar radiation characteristics. Table II shows their maximum directivity D_0 and their radiation efficiency e_{rad}. This similarity between the two structures can as well be noticed by comparing the electric field distributions in Fig. 3a and Fig. 4a and the radiation patterns (solid line in Fig. 5a and Fig. 5b).

When the NFRP structure is inserted in the inner layer, it can be seen in Fig. 3b that the distribution of the electric field

TABLE II: Directivity and radiation efficiency

		2.45 GHz	2.85 GHz
w/o NFRP	D_0	5.71	4.89
	e_{rad}	0.42	0.45
w/ NFRP	D_0	5.53	4.91
	e_{rad}	0.42	0.09

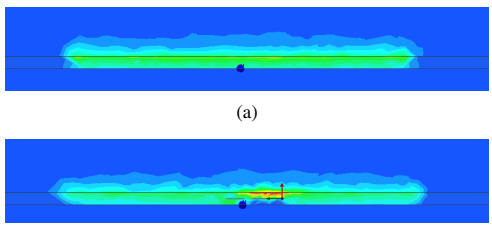

(a)

(b)

Fig. 3: Simulated electric field in the xz plane at the patch edge at 2.45 GHz, without (a) and with (b) the NFRP structure, respectively.

at 2.45 GHz is locally modified, getting stronger nearby the element. This is mostly due to the fact that the same field strength is confined in a smaller volume, since the NFRP has the same potential as the ground (especially close to the via connection). This does not influence the radiation pattern in a significant way, as read in Fig. 5a, nor the radiation efficiency reported in Table II.

On the contrary, when the element is inserted below a source at the frequency that is intended to cancel, it reduces the electric field strength along the radiation slot as can be seen in Fig. 4b. This does not affect the overall directivity in itself but rather the radiation efficiency of the patch, which is noticeably reduced by a factor of 5, and thus ultimately the radiation pattern as shown by the dotted line in Fig. 5b.

This shows the effectiveness of the NFRP in reducing the forward gain, and that the element is practically invisible outside the band that it is intended to reject.

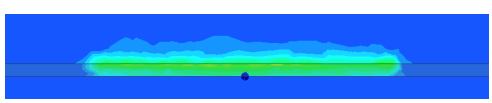

(a)

(b)

Fig. 4: Simulated electric field in the xz plane at the patch edge at 2.85 GHz, without (a) and with (b) the NFRP structure, respectively.

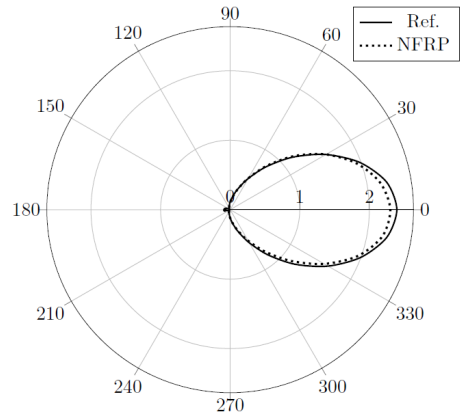

(a)

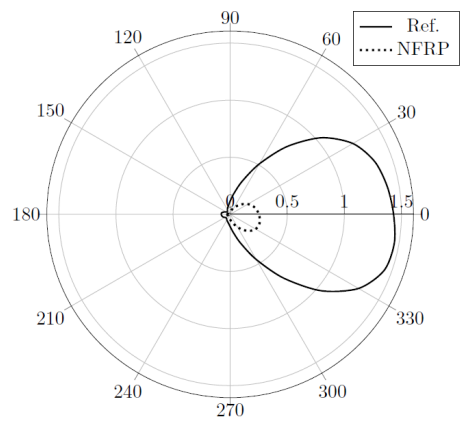

(b)

Fig. 5: Simulated gain pattern in the xz plane for the 2.45 GHz (a) and the 2.85 GHz (b) patch antenna with (dotted line) and without (solid line) the NFRP structure beneath.

IV. EMC Performance

A study of the effectiveness of the structure to reduce the EMI from the board has been performed as experimental verification. The source of EMI radiation, namely any signal trace on PCBs, is again modelled via a patch antenna. This permits to have a significant radiation at the frequency of interest, allowing for better measurements. It has the drawback of acting as an actual antenna, and thus to be loaded by the presence of the resonator. The patch is tuned to the resonance frequency of the ENG element. The measured values are afterwards normalized with respect to the frequency of interest for the sake of comparison with the results from the previous section. A reference board, comprising of the same radiation

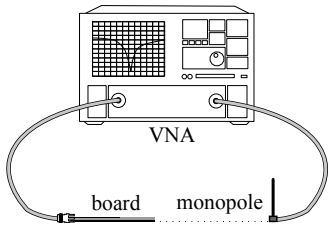

Fig. 6: Measurement setup for the study of radiation leakages in the xy (edge) plane.

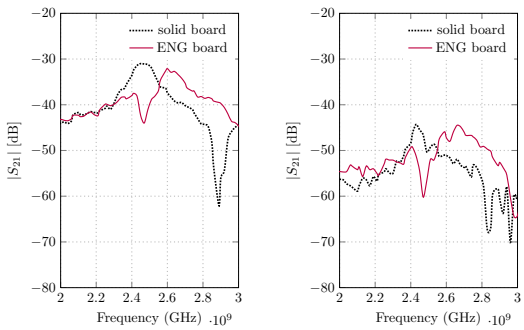

Fig. 7: Leakage radiation in the xy (edge) plane, with the probe placed 5 cm (a) and 40 cm (b) away from the edge of the PCB, respectively.

source but without the ENG resonator, is used for comparison purposes. That being so, the results should be understood in a qualitative way.

The radiated fields are measured by the use of a monopole antenna at different positions and distances from the board in the xy (board edge) plane. The results in Fig. 7a and Fig. 7b are sampled at the edge plane with the setup shown in Fig. 6, progressively increasing the distance from the board. The valley caused by the resonator, that reduces the unwanted frequency of approximately 6 to 8 dB, is clearly visible. This is due to fact that the fields diffracted from the source edge are strongly coupled to the ENG structure and then dissipated in the ground plane. It is of interest to notice that they are not re-radiated along the edge plane, as has been observed in the literature for some EBG designs [6], [9]: thus the system is effectively reducing the radiation at the target frequency.

Due to the specific setup used here, i.e., a patch antenna as a radiation source, a noticeable shift in the frequency of the radiation peak is observed. This is most likely due to the loading effect of the ENG resonator on the patch, that changes its effective electrical length and the way that the device radiates—the actual attenuation has been corrected for this dependency of the setup. Please note, this frequency shift would not be compatible with the case of a radiating line.

V. Conclusion

In this work it was shown that it is possible to reduce the narrow-band EMI of a radiating source, in this case modelled via a patch antenna, through the use of a metamaterial-inspired near-field resonant parasitic element. The result is achieved with an extremely small structure that leaves substantially unaltered the ground plane characteristics. This accounts for an actual filtering not only as referred to the insertion loss of a line, but for the part radiated by a line and thus it qualifies as a way to reduce the interference radiated by transmission lines on boards.

References

[1] A. Abidi, "Direct-conversion radio transceivers for digital communications," *IEEE Journal of Solid-State Circuits*, vol. 30, no. 12, pp. 1399–1410, 1995.

[2] B. Razavi, "Design considerations for direct-conversion receivers," *IEEE Transactions on Circuits and Systems II: Analog and Digital Signal Processing*, vol. 44, no. 6, pp. 428–435, 1997.

[3] S. Shahparnia and O. Ramahi, "Electromagnetic interference (EMI) reduction from printed circuit boards (PCB) using electromagnetic bandgap structures," *IEEE Transactions on Electromagnetic Compatibility*, vol. 46, no. 4, pp. 580–587, 2004.

[4] M. Kim, K. Koo, C. Hwang, Y. Shim, J. Kim, and J. Kim, "A Compact and Wideband Electromagnetic Bandgap Structure Using a Defected Ground Structure for Power/Ground Noise Suppression in Multilayer Packages and PCBs," *IEEE Transactions on Electromagnetic Compatibility*, vol. 54, no. 3, pp. 689–695, Jun. 2012.

[5] F. D. Paulis and L. Raimondo, "Compact Configuration for Common Mode Filter Design based on Planar Electromagnetic Bandgap Structures," *IEEE Transactions on Electromagnetic Compatibility*, vol. 54, no. 3, pp. 646–654, 2012.

[6] J. Qin, O. Ramahi, and V. Granatstein, "Novel planar electromagnetic bandgap structures for mitigation of switching noise and EMI reduction in high-speed circuits," *IEEE Transactions on Electromagnetic Compatibility*, vol. 49, no. 3, pp. 661–669, 2007.

[7] J. Baena and J. Bonache, "Equivalent-circuit models for split-ring resonators and complementary split-ring resonators coupled to planar transmission lines," *IEEE Transactions on Microwave Theory and Techniques*, vol. 53, no. 4, pp. 1451–1461, 2005.

[8] R. Marqués, F. Medina, and R. Rafii-El-Idrissi, "Role of bianisotropy in negative permeability and left-handed metamaterials," *Physical Review B*, vol. 65, no. 14, p. 144440, Apr. 2002.

[9] M. M. Bait-Suwailam and O. M. Ramahi, "Ultrawideband Mitigation of Simultaneous Switching Noise and EMI Reduction in High-Speed PCBs Using Complementary Split-Ring Resonators," *IEEE Transactions on Electromagnetic Compatibility*, vol. 54, no. 2, pp. 389–396, Apr. 2012.

[10] P. D. Imhof, R. W. Ziolkowski, and J. R. Mosig, "Highly subwavelength unit cells to achieve epsilon negative (ENG) metamaterial properties," *IEEE Antennas and Propagation Society International Symposium 2006*, vol. 2, no. 1, pp. 1927–1930, 2006.

[11] A. Erentok and R. Ziolkowski, "Metamaterial-inspired efficient electrically small antennas," *IEEE Transactions on Antennas and Propagation*, 2008.

[12] C. Lin, P. Jin, and R. Ziolkowski, "Single, Dual and Tri-Band-Notched Ultrawideband (UWB) Antennas Using Capacitively Loaded Loop (CLL) Resonators," *IEEE Transactions on Antennas and Propagation*, vol. 60, no. 1, pp. 102–109, 2012.

[13] A. Ruaro, J. Thaysen, and K. B. Jakobsen, "Metamaterial-inspired Near-field Resonant Parasitic Structure for Directional Suppression of Narrow-band EMI/RFI in Compact Systems," in *2013 IEEE Antennas and Propagation Society International Symposium (APSURSI 2013)*, 2013.

[14] C. A. Balanis, *Antenna Theory: Analysis and Design*, 3rd ed. John Wiley & Sons, Inc., 2005.

[15] Ansys®, HFSS, Release 13.0.

Paper 3

"Directional EMI Reduction on PCB Transmission Lines via a Near-Field Parasitic Resonator"

A. Ruaro, J. Thaysen, and K. B. Jakobsen

[P3] A. Ruaro, J. Thaysen, and K. B. Jakobsen, "Directional EMI reduction on PCB transmission lines via a near-field parasitic resonator", *IEEE Transactions on Electromagnetic Compatibility*, 2016, submitted for publication.

Directional EMI Reduction on PCB Transmission Lines via a Near-Field Parasitic Resonator

Andrea Ruaro, Jesper Thaysen, and Kaj B. Jakobsen

***Abstract*—The design and application of a very compact metamaterial-inspired near-field parasitic resonator (NFPR) for reduction of electromagnetic interference (EMI) from high-density printed circuit boards (PCB) is detailed in this work. The structure is described and developed for miniature, highly-integrated electronic devices. The filter presents unique characteristics of directional filtering and very small dimensions while being placed in between the radiation source and the ground plane, thus is suitable for high-density, mixed-signals compact PCBs. Both the electromagnetic compatibility (EMC) and the signal integrity (SI) performance of a PCB where the NFPR is integrated are presented. The filtering effect, achieved when the element is placed in the near-field of the source, is studied by the radiation that originates from the board and on a microstrip transmission line. The radiation is studied with a patch antenna setup. The structure exhibits narrow-band suppression of a single frequency and its harmonics, as can be generated, e.g., by a power amplifier or by local oscillator leakages in a direct-conversion receiver. Simulations and measurements based on a PCB with the resonator and its comparison with a reference board are presented.**

***Index Terms*—Electromagnetic compatibility (EMC); planar filters; printed circuit boards (PCB); signal integrity (SI).**

I. Introduction

MINIATURE electronic devices confront printed circuit boards (PCB) with challenges related to the complexity of the highly-integrated environment. In fact, PCBs are often placed into equipment where the space available is severely constrained as in, e.g., mobile phones and handsets, medical devices as hearing instruments (HI) or cochlear implants, and the like. In particular, the space comes at a premium in wearable electronics, as the overall objects dimensions are very important for the user. Since compliance with EMC legislation is compulsory for product commercialization, all these devices must respect the EMI emission limits. In such small devices, the ground plane quality is often degraded, for example because it is divided in island to ensure separation between digital and analog signals; another reason is that the ground plane may be too electrically small in order to have a sufficiently low impedance, and therefore acts as a radiator. This is even more complex in high-density environments with both radio and digital subsystems as are the HIs, since the high-speed or power supply traces has no other option but to cross the RF lines.

Andrea Ruaro and Jesper Thaysen are with GN ReSound A/S, Lautrupbjerg 7, DK-2750 Ballerup, Denmark (e-mail: aruaro@gnresound.com, jtahysen@gnresound.com).

Kaj B. Jakobsen is with the Department of Electrical Engineering, Electromagnetic Systems, Technical University of Denmark, Ørsteds Plads, Building 348, DK-2800 Kgs. Lyngby, Denmark (e-mail: kbj@elektro.dtu.dk).

The overall dimensions bring in close physical and electrical proximity aggressors and victims, and hence require a strict control over the EMI environment. For instance, the traces on a PCB, especially if they form loops, may be excited by a source like a switched-mode power supply (SMPS) and couple noise into the loudspeaker or audio parts of a handset. In such contexts, where specific issues may arise, it is of interest to mitigate the narrowband EMI as may be generated by radio-frequency integrated circuits (RFIC). Noise sources include power amplifier (PA) harmonics and local oscillator (LO) leakage [**?**], [**?**].

It is not always possible or sufficient to apply traditional techniques, such as the use of decoupling capacitors on transmission lines. The space on the PCB may not be sufficient, or they could hinder the signal quality if they are not selective enough, i.e., if the frequency of operation is too close to the frequency that has to be rejected. The use of capacitors may furthermore be limited to the sub-GHz range [**?**]. As well, the introduction of electrically-small shielding cans does not represent a straightforward solution as it can complicate the electromagnetic environment [**?**]. Furthermore, their implementation may be really complex from a manufacturing perspective, is not possible in some applications, and it adds considerable cost.

Planar filtering structures, like defected ground structures (DGS) and electromagnetic bandgap (EBG) filters are widely used in electronic devices for suppression of EMI [**?**], [**?**], [**?**], [**?**]. In PCB design, filters are often a necessary choice [**?**], whereas the target radiation may be wideband or restricted to some specific frequencies. This article focuses on narrowband interference suppression, as is the case for the noise generated by specific harmonics of high-speed digital lines and interconnections, or from analogue devices as PAs or LOs. These requirements are fulfilled by a notch filter. EBG solutions are hindered in the context of space-constrained devices due to their dimensions that stays considerable even in planar implementations [**?**], [**?**]. In order to realize transmission line filters with sub-wavelength dimensions, the applications of metamaterial-inspired mu-negative (MNG) structures were studied in the past [**?**]. Nevertheless, in order to couple to microstrip lines a complementary design is needed, such as complementary split-ring resonators (CSRR), due to the orientation of the field required to excite the elements [**?**].

A serious drawback of DGSs, or equivalently of complementary designs, is that they require to be etched on the ground plane, or on a solid layer if available, respectively. Highly-integrated environments, moreover, may be even more complicated by the presence of an antenna, where the PCB

works as the ground plane of an unbalanced antenna. This requires a solid ground plane in order not to jeopardize the antenna performance. Cuts in the ground plane can, in fact, impact the current flow across the PCB and therefore impact parameters like, among others, the antenna polarization [**?**], [**?**].

To summarize, there is a need to mitigate the narrow-band EMI radiated by a source placed above an electrically-small ground plane, without the possibility of either compromising the solidity of the latter due to antenna needs, or introducing any other solid plane above it. The filter needs to have strongly sub-wavelength dimensions, have high selectivity, and act on multiple radiation sources confined within a certain area; this without affecting the digital transmission line routed nearby. This work considers a recently developed [**?**] epsilon-negative (ENG) metamaterial-inspired near-field parasitic resonator (NFPR) and develops it as a filter. The structure was originally intended for a different purpose. It has primarily been used to enhance the radiation characteristics of electrically-small antennas [**?**], [**?**], [**?**]. The preliminary study of the NFPR application in this configuration is reported in [**?**], [**?**].

The paper is structured as follows. Section II details the resonator geometry and the coupling mechanism, whereas Section III discusses its design and implementation. Section IV addresses the EMI radiation and includes a presentation of the setup used for the characterization. In Section V the focus is on the SI performance with eye diagrams shown for different positions and directions of a transmission line located near the resonator. Conclusions are given in Section VI.

II. Resonator and Coupling Mechanism

The resonator structure is realized as a tightly meandered line as shown in Fig. 1. This results in an epsilon-negative (ENG) resonator, which is a highly subwavelength structure that exhibits a dielectric constant with a negative real part at given design frequencies [**?**]. Such resonators were originally studied to be used as a unit cell in metamaterial implementations [**?**]. In the present case, a similar structure is used in a different way: in fact, it is placed above a ground plane and is connected to ground with a vertical interconnect access (VIA). This changes the way that the structure behaves and gets excited. It allows the currents that are induced on the structure to propagate and spread on the ground plane. Since the solid ground plane has a very low impedance, it significantly lowers the amount of radiation caused by the currents that propagates on it.

The element itself is designed as a tightly meandered transmission line. With reference to Fig. II, it consists of a number n of branches, each of length l and width w. The branches are spaced by an amount s and are connected at alternative ends by a short line of width t. The termination of the NFPR is an open circuit ($O.C.$) at the non-short-circuited end. This implementation has the huge advantage of an easy integration in the PCB manufacturing process, as it makes use of the same copper deposition technique.

Given the electrical dimensions of the structure, the main behavior that is studied here is an actual resonance along the

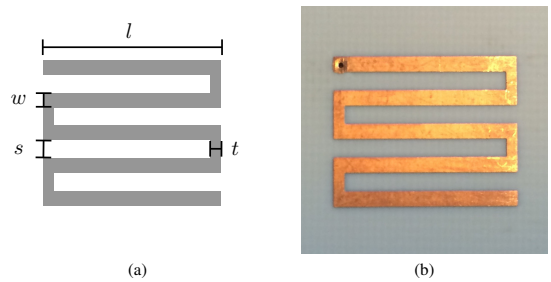

(a) (b)

Fig. 1. Element geometry, with dimensions. (a) Diagram and (b) picture, respectively.

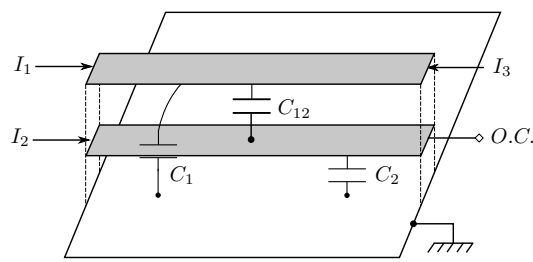

Fig. 2. Broadside-coupled lines above a common ground plane.

structure; hence the NFPR denomination is preferred over that of ENG-structure. The resonant frequency of the element is determined by the total distributed effective capacitance and inductance of the element. When this structure is isolated, it can be excited by an electromagnetic varying field. When it is placed in close proximity to a ground plane, the **E**-fields induced on it are aligned to those of a microstrip line, i.e., they are normal to the plane where the structure lays. In such way, the element is effectively excited from the quasi-TEM mode propagating on a microstrip line. The proximity to the ground plane ensures that the structure itself does not radiate, i.e., it is an inefficient radiator [**?**].

The coupling mechanism can be described by analogy to the traditional planar coupled-line microwave couplers [**?**]. In fact, it can be seen as a directional coupler with a terminated port that works selectively at a given frequency. The geometry is shown in Fig. 2. A microstrip line is capacitively broadside-coupled to it. As microstip transmission lines support a quasi-TEM propagation mode, each line can be described by the velocity of propagation v and by an equivalent distributed capacity to ground, C_1 and C_2, respectively; and a distributed capacity in between them, C_{12}. A third conductor, i.e., the ground plane, is necessary in order to support the propagation mode on the transmission lines. The filtering effect is hence achieved due to the resonant behavior of the NFPR. The current I_1 flows on the microstrip above the element and induces a second current I_2 that, in turn, excites the NFPR. The current then propagates to the ground through the electrical connection.

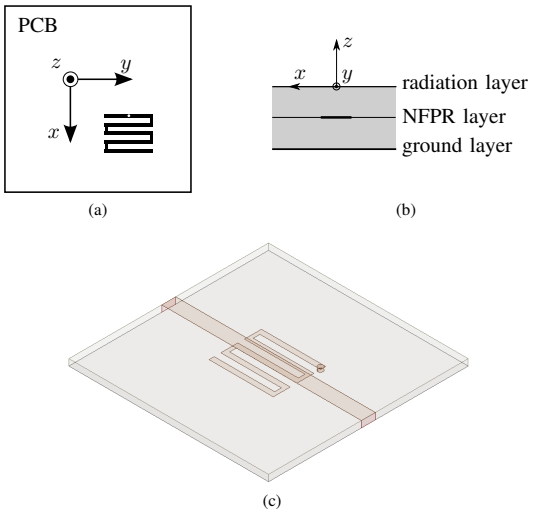

Fig. 3. Board geometry. (a) Top, (b) side, and (c) perspective view, respectively.

III. NFPR Design

In a high-density environment as the flex PCB of a HI, there is a multitude of traces routed on each layer, and space is of outmost importance. If there is a radiation source interfering with the functioning of the device, it is not possible to simply route the traces far away from it. This is made possible by the NFPR as it has a structure that is not rotationally symmetric: this allows the traces to be drawn in one direction to be filtered by the structure, while other traces, e.g., placed on different layers, can be drawn in a different direction and subsequently not be affected by the filter. The structure is strongly sub-wavelength, being only $0.13\lambda \times 0.11\lambda$ in size.

One of the most important aspects of this structure is its placement in the PCB stack-up. In fact, different solutions that were already proposed must have the interference source placed in between solid planes, or need at least two full solid planes. Instead, here the radiation source sits on the top layer as shown in Fig. 3. Therefore it cannot be shielded with an extra power or ground plane, nor with a shielding can. In this paper the structure is etched on a PCB inner layer and VIA-connected to ground. It is manufactured on a $h = 0.8$ mm thick substrate. One test board was realized on a Rogers RO4003 substrate for evaluation purposes with an operating frequency of 1.5 GHz, while a second board with an operating frequency of 3.25 GHz was built on FR-4 for lab testing. The ground plane is a $d \times d$ square. The radiation source is either a patch antenna as in Section IV or a microstrip transmission line as in Section V, and it is implemented on a second layer with the same thickness $h = 0.8$ mm. The NFPR is implemented directly in the substrate, in a layer between the signal tracks and the ground layer. The dimensions of the two boards, including the NFPR dimensions, are given in Table I. A 50 Ω microstrip transmission line crosses the center of the NFPR structure at a height $2h = 1.6$ mm above the ground plane, i.e., at a height $h = 0.8$ mm above the NFPR structure. The dimensions of the structure are given in Fig. 1 and Table I. Different characteristic of the NFPR working principles and design are addressed below.

TABLE I
NFPR Board Design Parameters

	RO4003	FR-4
l	16.1 mm	8.7 mm
w	1.3 mm	0.7 mm
s	1.7 mm	1.1 mm
t	0.9 mm	0.5 mm
n	5	5
h	0.8 mm	0.8 mm
d	50 mm	150 mm
ε_r	3.55	4.4
$\tan\delta$	0.0027	0.02

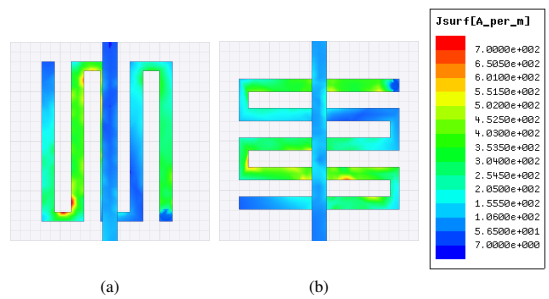

Fig. 4. Top view of the simulated current magnitude on a PCB trace and on the NFPR. (a) Co-directional set-up and (b) cross-directional set-up.

1) Directionality: The structure is designed to act as a notch filter, i.e., to reject the propagating signal for a narrow band only. Given the extremely high density of interconnects on physically-small PCBs, it is necessary that the signal is preserved on the transmission lines where the filter is not desired. Hence, it is of critical importance that the filter acts mainly for specific lines. A way to do this is to make the filter dependent upon the direction of the incoming lines, so that the designers can decide which specific transmission lines to filter by choosing their orientation. The difference in the current and **E**-field distribution for the co- and cross-directional set-up is shown in Fig. 4 and Fig. 5, respectively.

Due to the **E**-field coupling mechanism, the NFPR is able to provide attenuation of a signal travelling on a co-directional microstrip line of more than 18 dB as shown in the measurements in Fig. 6. This is approximately 11 dB over the rejection of the same signal traveling on a microstrip line orientated cross-directional to the structure. Furthermore, in order to select the amount of rejection, it is possible to act also on the relative offset of the PCB lines from the center of the NFPR, as highlighted further on in Section V.

2) Tuning: The resonator can be tuned to operate at a desired frequency, i.e., it allows to choose the frequency that must be rejected. This can be achieved by selecting the scaling

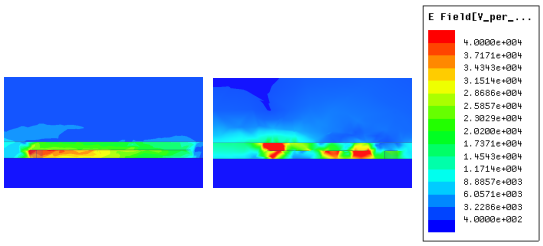

(a) (b)

Fig. 5. Side view of the simulated **E**-field on the PCB trace and on the NFPR. (a) Co-directional set-up and (b) cross-directional set-up.

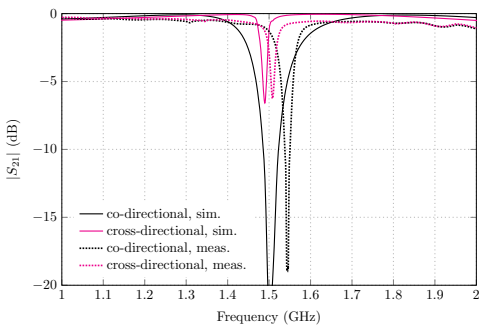

Fig. 6. Simulation (solid line) and measurement (dotted line) of the transmission coefficient $|S_{21}|$ of a single 50 Ω microstrip transmission line that crosses the NFPR element, for both the co-directional (black) and cross-directional (red) case.

of the structure as shown in Fig. 7, where l is the reference dimension. Furthermore, even though it is not explored in this study there is the possibility to introduce a series variable capacitance for active frequency tuning, e.g., a varactor, a switched capacitor bank, or the like.

It is possible to add a series resistance R to the direct electrical connection to ground, i.e., the VIA, at the grounding point of the NFPR. This impacts the amount of current running

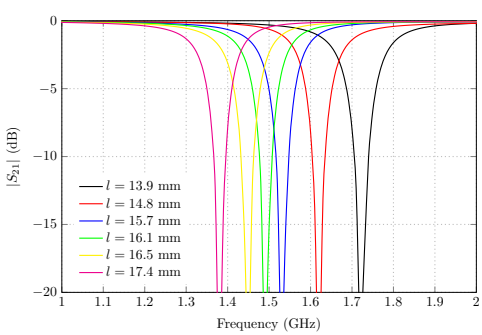

Fig. 7. Tunability of the NFRP structure as a function of the scaling, expressed though the branch length l.

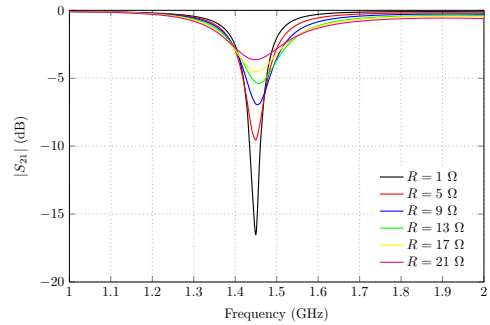

Fig. 8. Resistor tuning in 4 Ω steps through the range $1 - 21$ Ω.

on the structure and the total resistive losses. In fact, this additional loss makes it possible to increase the rejection bandwidth of the NFRP. This comes at a price, since the insertion loss IL of the filter is decreased as the self-resonance of the NFPR element is not as strong any longer. A trade-off shall be carefully studied by the designer according to the specific application. An example, with resistors in the range $1 - 21$ Ω, is shown in Fig. 8.

IV. EMC Performance

When a planar filter design is proposed, its performance is usually characterized for use in purely microwave systems (like radio front-ends), and thus most of the times the description is limited to S-parameters data. Though, when it needs to be implemented and integrated into a complex product, there are further instances that have to be taken into account. In fact planar filters can be used also in consumer electronics devices for different purposes, and it is thus necessary to characterize such filters from an EMC and SI point of view. In high-density and mixed-signals environments there are PCB traces carrying digital signals that cross or are located near the RF sub-system, and eventually to the filter. This is the reason why filters that aim to be implemented not only in a purely analogue front-end should be additionally characterized, as can be seen, e.g., in [**?**]. Indeed, the use in high-density, complex environments calls for a characterization that goes beyond the single insertion loss information. The behavior of a PCB containing the mentioned resonator is thus analyzed probing the radiation from the board and with eye diagrams, which are representative for the EMC and SI performance, respectively. The EMC results are informative of the behavior of the board at different distances both in the near-field and in the far-field. It certifies if the use of the resonator for EMI suppression is effective, or if the radiation is instead simply re-radiated by the ground plane. The SI results are necessary to allow the actual implementation of the filter in mixed-signal environments, as is the case for most of consumer electronics products. The SI analysis is critical when selecting the best position of the lines that carry high-speed digital and clock signal nearby the resonant structure.

The EMI source, i.e., the signal traces on the PCBs, is modeled here by the use of a patch antenna. This makes it possible

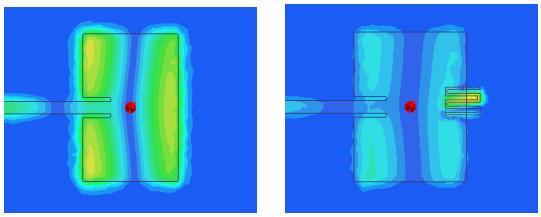

(a) (b)

Fig. 9. Simulated **E**-field of the patch antenna, (a) reference and (b) coupling to the NFPR.

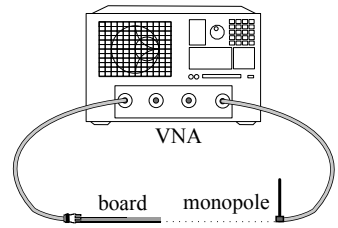

Fig. 10. Measurement setup for the study of radiation leakages in the xy-plane (edge).

to have significant radiation at the frequency of interest, which makes the measurements more clear. Furthermore, it makes it easier to understand the radiation mechanism, since it is well known for such a device [**?**]. The fields radiated by the patch, in fact, couple well to the NFPR, as can be seen by the **E**-field plots shown in Fig. 9. Hence, the radiation source acts as an actual antenna, and thus may be detuned by the presence of the resonator. The patch is tuned to 3.25 GHz in order to match it to the resonance frequency of the NFPR. A reference board, that comprises of the same radiation source but without the NFPR is used for comparison purposes. That being so, the results should be understood in a qualitative way.

The radiated fields are measured with a monopole probe, and sampled at different positions and distances from the board on the xy-plane (board edge) and on the xz-plane. The setup reported in Fig. 10 is used to sample the results shown in Fig. 11 on the edge plane, where the distance from the board is progressively increased. The setup shown in Fig. 12 is used to sample the results shown in Fig. 13 at a height of 100 mm above the board.

In Fig. 11 it is clearly visible that the valley caused by the resonator reduces the unwanted frequency of approximately 6 to 8 dB. This is due to the fact that the fields diffracted from the source edge are strongly coupled to the NFPR structure and then dissipated in the ground plane. It is of interest to notice that they are not re-radiated along the edge plane, as has been observed in the literature for some DGS designs [**?**], [**?**]: thus the system effectively reduces the radiation at such a frequency. Due to the specific setup used here, i.e., the use of a patch antenna as a radiation source, a shift in the frequency of the radiation peak is noticed. This is most likely due to the loading effect of the NFPR on the patch that changes its effective electrical length and the way that the device radiates—the actual attenuation has been corrected for this dependency in the setup. Please note, this frequency shift would not be compatible with the case of a radiating line.

In the plane on the top of the PCB, 100 mm above the surface, the phenomenon is not as evident. Even though, the resonance of the NFPR structure at 3.25 GHz is in any case visible in Fig. 13. The same behaviour can be observed as well in the measurements conducted by placing the boards in a gigahertz transverse electromagnetic (GTEM) cell, which are shown in Fig. 14.

V. SI Analysis

The effect of the NFPR on the SI performance is presented in this section. The geometry is the same as the one used in Fig. 3, where a transmission line runs on the layer above the resonator. The transmission line is implemented as a 3 mm wide microstrip with a characteristic impedance of 50 Ω. The line is 150 mm long on a 1.6 mm high FR-4 substrate, hence with a rather significant loss tangent. The structure is analyzed with Ansys HFSS, whereas the eye diagram is computed with Ansys Designer. The S-parameters matrix used in the co-simulation is densely sampled over a broad range of frequencies. The pulse signal source is a pseudorandom bit sequence of length $2^7 - 1$ bits, and a probe is placed at the other end of the transmission line. The bit sequence has the low logic level equal to 0 V, high logic level equal to 1 V, and is coded at 2 Gb/s with rise and fall times of 10 ps.

The eye diagram for the transmission line on the reference board without the resonator is shown in Fig. V. In Fig. V the transmission line crosses the center of the structure along the y-direction: a worsening in the jitter, signal-to-noise ratio, etc., is visible, but the eye opening is well preserved. In Fig. V the transmission line is again aligned in the y-direction, but it is displaced at an offset of 1.5 mm from the edge of the resonator structure. It can be seen that the performance is substantially unaltered. The same applies to the case of a transmission line that crosses the center of the structure along the x-direction. The result can be seen in Fig. V.

It can thus be inferred how the NFPR degrades the signal integrity only along the y-direction, and only for traces directly above it. This is the case for which the insertion loss is larger, too. This allows margins for routing the high-speed digital traces around the structure and along the x-direction, without fearing any harm to the digital signals from the device. Ultimately, this allows to take the NFPR into consideration for implementation in high-density, compact, and mixed-signal systems.

VI. Conclusion

A novel planar filter structure for use in highly-integrated miniature devices has been proposed in this work. The strongly sub-wavelength metamaterial-inspired near-field parasitic resonator allows for directional filtering of microstrip transmission lines on PCBs. The structure demonstrated in simulations and measurements to be able to improve the PCB's EMC performance while ensuring a good SI level. The design

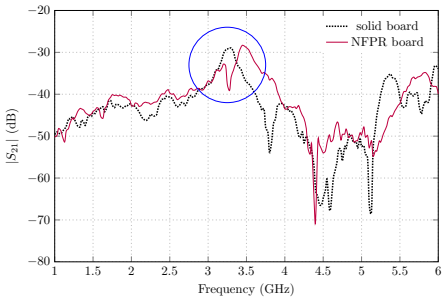

(a)

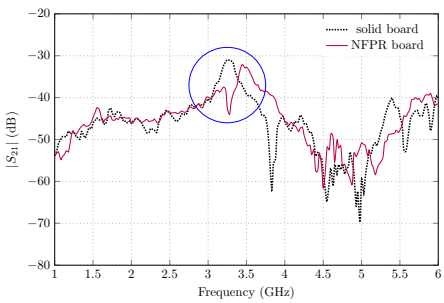

(b)

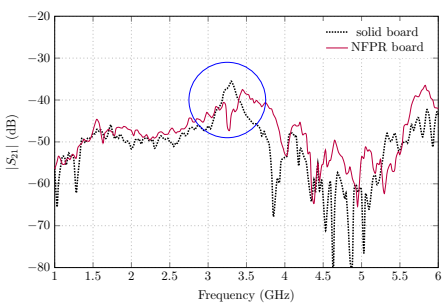

(c)

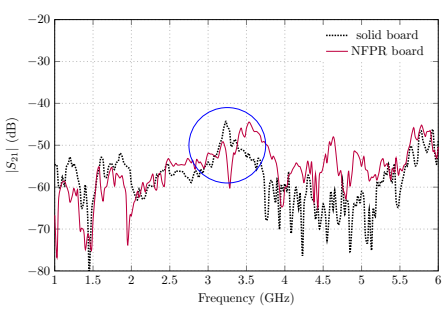

(d)

Fig. 11. Leakage radiation in the xy-plane (edge), with the probe placed at a given distance from the edge of the PCB at (a) 20 mm, (b) 50 mm, (c) 100 mm, and (d) 400 mm.

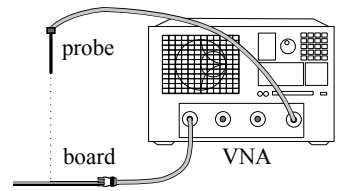

Fig. 12. Measurement setup for the study of radiation leakages in the xy plane, 100 mm above the board.

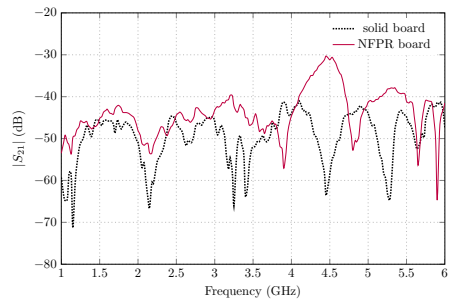

(a)

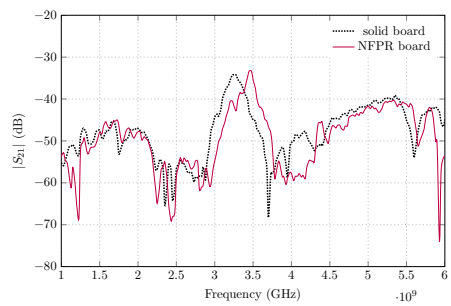

(b)

Fig. 13. Leakage radiation on the top of the PCB edge, at a distance of 100 mm from the PCB, (a) on the top of the radiation source and (b) on the top of the PCB edge.

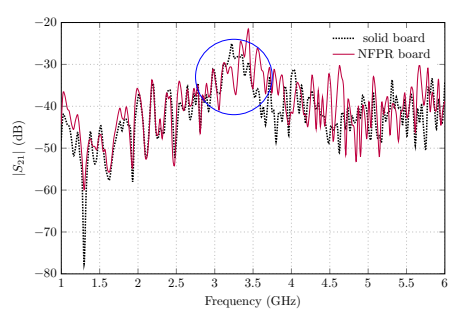

Fig. 14. GTEM cell cabled measurements of the DUT.

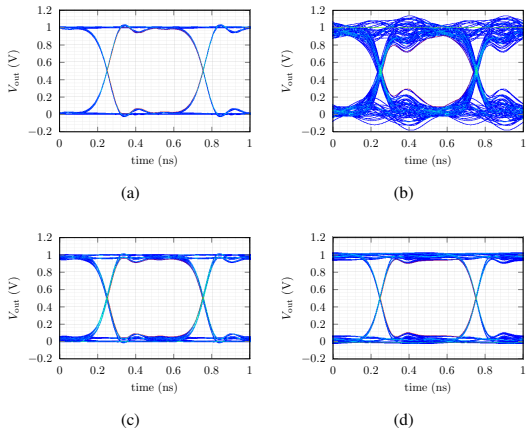

Fig. 15. Eye diagram for different orientations and offset (different positions) of the trace: (a) reference board; (b) y-aligned, centred; (c) y-aligned, offset; (d) x-aligned.

of the structure is detailed and the coupling mechanism to transmission lines is illustrated. The use of the resonator within the PCB for suppression of narrowband EMI radiation is outlined and its consequences are characterized from a radiation point of view along the main (edge) plane at the level of and above the PCB. It is seen that the NFPR is able to reduce unwanted radiation by approximately 6 to 8 dB. The SI performance has been assessed through simulated eye diagrams. It is clearly seen how traces that runs at a short distance offset from the NFPR are not affected by it, as well as traces that crosses it in a perpendicular direction—that is, when the coupling is loose. This shows how the filtering effect can be obtained for RF transmission lines in a compact PCB, while high-speed digital lines can be routed around the structure or crossing it in a perpendicular way. This structure may find use in high-density, mixed signal boards to mitigate narrow-band EMI, in electrically- and physically-small devices like hearing instruments.

Andrea Ruaro was born in Venezia, Italy, in 1988. He received the B.Sc. degree in Information Engineering from the University of Padova in 2010, and the M.Sc. degree in Electrical Engineering from the Technical University of Denmark in 2012. He is currently working toward the Ph.D. degree at the Technical University of Denmark. Since 2012 he has been affiliated with GN ReSound A/S, a leading hearing instrument manufacturer.

His research interests include electromagnetic interaction and coupling, EMC, and on-body antennas and propagation.

Jesper Thaysen received the B.Sc., M.Sc., and Ph.D. degrees in electrical engineering from the Technical University of Denmark in 1998, 2000 and 2005, respectively. Since 2008 he has been employed at GN ReSound A/S, a Danish hearing instrument manufacturer, where he currently acts as the Director of the Radio Systems group in R&D.

His research interests include small antennas and on-body antennas and propagation. Dr. Thaysen has overseen more than 40 B.Sc. and M.Sc. students, as well as 3 Ph.D. students, as the company representative in university-industry cooperative projects.

Kaj B. Jakobsen received the B.Sc.EE and the M.Sc.EE degree from the Technical University of Denmark, Kgs. Lyngby, in 1985 and 1986, respectively, the Ph.D. degree in Electrical Engineering from University of Dayton, Dayton, OH, in 1989, and the HD in Organization and Management, Copenhagen Business School, Copenhagen in 2000. From 1986-1989 he was a Fulbright Scholar at the Department of Electrical Engineering, University of Dayton, OH. Since 1990 he has been with the Department of Electrical Engineering, Technical University of Denmark, Kgs. Lyngby, where he is Associate Professor.

His research interests are in body-centric wireless network, wireless body area network, and body sensor network. He received in 1989 the NCR Stakeholder Award, Ohio, USA, and was appointed Teacher-of-the-Year at the Technical University of Denmark in 1994.

(19) Europäisches Patentamt
European Patent Office
Office européen des brevets

(11) EP 2 733 962 A1

(12) EUROPEAN PATENT APPLICATION

(43) Date of publication:
21.05.2014 Bulletin 2014/21

(51) Int Cl.:
H04R 25/00 *(2006.01)* ***H04B 15/02*** *(2006.01)*

(21) Application number: **12193225.5**

(22) Date of filing: **19.11.2012**

(84) Designated Contracting States:
AL AT BE BG CH CY CZ DE DK EE ES FI FR GB GR HR HU IE IS IT LI LT LU LV MC MK MT NL NO PL PT RO RS SE SI SK SM TR
Designated Extension States:
BA ME

(71) Applicant: **GN ReSound A/S**
2750 Ballerup (DK)

(72) Inventor: **Ruaro, Andrea**
2400 København NV (DK)

(74) Representative: **Zacco Denmark A/S**
Hans Bekkevolds Allé 7
2900 Hellerup (DK)

(54) **A hearing aid having a near field resonant parasitic element**

(57) A hearing aid is provided comprising a microphone, a signal processor for processing an incoming audio signal to compensate a hearing loss of a user of the hearing aid, a speaker that is connected to an output of the signal processor to provide a sound signal to a user, a transceiver connected to the signal processor for wireless data communication interconnected with an antenna for emission and reception of an electromagnetic field, an electrical circuitry comprising at least one of the signal processor, the transceiver, interconnecting transmission lines, antenna structures and/or further electrical components, the electrical circuitry extending over an area of a support substrate. The hearing aid further comprises a resonant element being provided within the near field of the electrical circuitry to terminate and dissipate unwanted electromagnetic radiation from at least a part of the area. The resonant element implements a notch filter filtering the unwanted electromagnetic radiation and may be positioned outside any signal paths of the electrical circuitry.

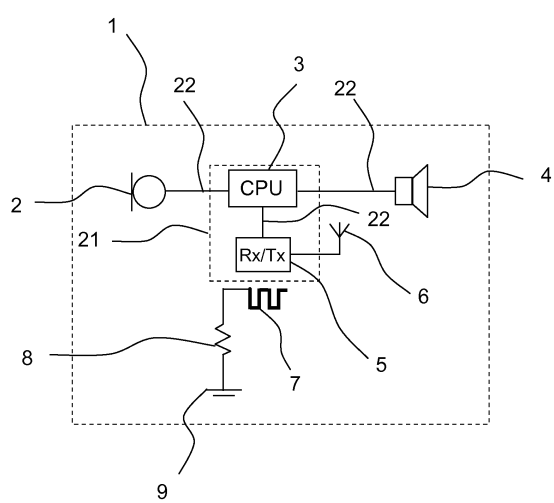

Fig. 1

EP 2 733 962 A1

Printed by Jouve, 75001 PARIS (FR)

US 20140140554A1

(19) **United States**

(12) **Patent Application Publication**

RUARO

(10) **Pub. No.: US 2014/0140554 A1**

(43) **Pub. Date: May 22, 2014**

(54) **HEARING AID HAVING A NEAR FIELD RESONANT PARASITIC ELEMENT**

(71) Applicant: **Andrea RUARO**, Kbh. NV (DK)

(72) Inventor: **Andrea RUARO**, Kbh. NV (DK)

(21) Appl. No.: **13/682,632**

(22) Filed: **Nov. 20, 2012**

(30) **Foreign Application Priority Data**

Nov. 19, 2012 (DK) ..... PA 2012 70715
Nov. 19, 2012 (EP) 12193225

Publication Classification

(51) **Int. Cl.**
H04R 25/00 (2006.01)

(52) **U.S. Cl.**
CPC ***H04R 25/554*** (2013.01)
USPC **381/315**

(57) **ABSTRACT**

A hearing aid includes: a microphone for reception of sound and conversion of the received sound into a corresponding first audio signal; a signal processor for processing the first audio signal into a second audio signal compensating a hearing loss of a user; a speaker connected to an output of the signal processor for converting the second audio signal into an output sound signal; a transceiver connected to the signal processor for wireless data communication; and an antenna for emission and reception of an electromagnetic field, the antenna coupled with the transceiver; wherein the signal processor, the transceiver, the antenna, and interconnecting transmission lines form a circuitry extending over an area of a support substrate, and wherein the hearing aid further comprises a resonant element within a near field of the circuitry to terminate and dissipate unwanted electromagnetic radiation from at least a part of the area.

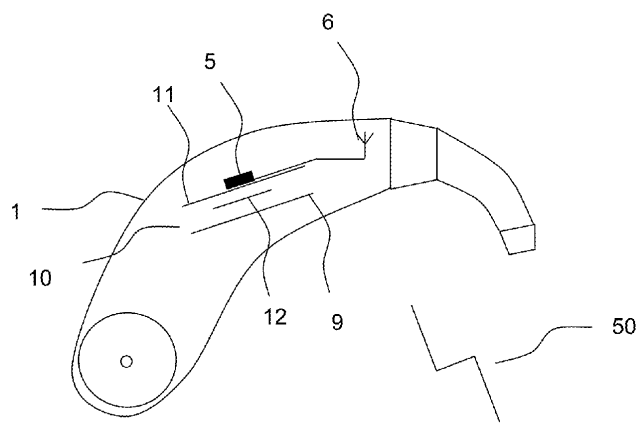

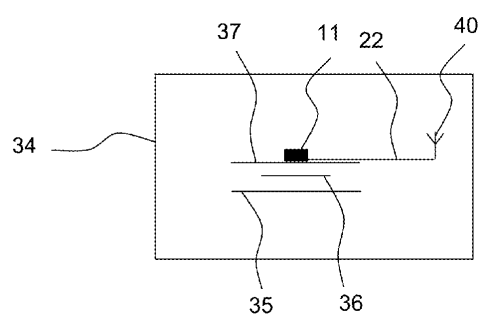

Paper 4

"Simultaneous Out-of-band Interference Rejection and Radiation Enhancement in an Electronic Product via an EBG Structure"

A. Ruaro, J. Thaysen, and K. B. Jakobsen

[P4] A. Ruaro, J. Thaysen, and K. B. Jakobsen, "Simultaneous out-of-band interference rejection and radiation enhancement in an electronic product via an EBG structure", in *Proceedings of the International Microwave Symposium (IMS)*, 2014.

Simultaneous Out-of-band Interference Rejection and Radiation Enhancement in an Electronic Product via an EBG Structure

Andrea Ruaro*†, Jesper Thaysen*, and Kaj B. Jakobsen†

*GN ReSound A/S, Lautrupbjerg 7, DK-2750 Ballerup, Denmark
†Department of Electrical Engineering, Technical University of Denmark, DK-2800 Lyngby, Denmark

***Abstract*—This work presents an application of a planar electromagnetic band gap (EBG) structure with a perspective product implementation in the back of the mind. The focus is on the integration of such structure under the constraint of space and system coexistence. It is discovered that it is possible to achieve simultaneously both the enhancement of the antenna radiation efficiency and the shrinking of its dimensions, while making the device more resilient to out-of-band electromagnetic interference (EMI). The patterning of the ground plane allows, in fact, to effectively suppress higher-order resonances (alternatively, parallel plate noise) and decrease the radiation efficiency of the structure forbidding higher-order modes to propagate and subsequently be diffracted by the ground plane.**

***Index Terms*—Electromagnetic interference (EMI); electromagnetic compatibility (EMC); electromagnetic band gap (EBG) structures; small antennas; printed circuit boards (PCB)**

I. Introduction

Electronic products such as handsets, mobile phones, wireless medical devices [1], etc..., are subjected to regulation concerning their electromagnetic compatibility (EMC) performance. Since their either main or accessory function is to communicate, they are substantially composed by at least a radio system comprising of a radio circuit and an antenna, and of a digital signal processor (DSP). In most cases, their dimensions and integration are constrained following the directions given by different industrial functions such as other engineers, mechanical designers, and marketing. For the electronics, this translates into a high level of integration, with all the functions confined on a small printed circuit board (PCB). Fig. 1 shows as an example all the space available in a given wireless medical device. The mutual proximity eases the jamming among sub-systems, in particular the analogue signals of the radio and the digital signals of the DSP can couple to antenna feed, power distribution network, high-speed interconnects, etc..., and ultimately be radiated as spurious emissions.

EBG structures, either planar or three-dimensional, have been proven able to filter EM noise from transmission lines and PCBs [2]–[4]. In fact, either the lines couple to the resonant structures of the EBG so that the energy of the propagating unwanted mode is reduced, or the EBG proves able to suppress the parallel plate resonance possibly occurring,

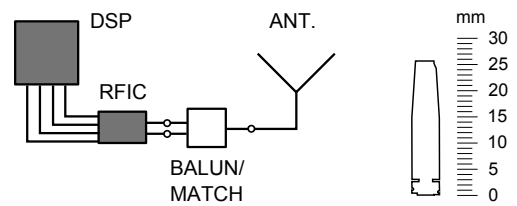

Fig. 1: Diagram (a) and PCB outline example (b), with related scale, of a compact-size electronic product having a wireless interface.

e.g., between the power and ground planes [5]. Alternatively, when the application demanded, defected ground structures (DGS) or metamaterial-inspired structures [6]–[8] have also been deployed with success to reduce interference, either from a full board or from scattered radiation sources confined on an area of the PCB. These signals are in general spread over a wide frequency spectrum.

On the other hand, EBG structures have been used in recent years to enhance radiation properties of antennas [9], [10]. Nevertheless, these works do not include considerations on their integration or performance versus EMI. A patch antenna is strongly dependent upon its ground plane structure, and therefore its radiation characteristics are notably influenced by it. The parameters that are mostly impacted are physical dimensions, directivity, bandwidth, and efficiency.

It has been left unanswered by literature studies if, choosing carefully the design of the EBG structure, the designer can simultaneously obtain an enhancement of the antenna radiation efficiency and bandwidth, while suppressing the noise coming from other transmission lines and the PCB itself. This work focuses on the design of an antenna with improved out-of-band spurious emissions performance, and brings the example of a device that has an alarming level of radiated power due to the power amplifier harmonics.

The article is organized as follows. Section II explains the set-up and the ground for its modelling. Section III presents and elaborates the results from FEM simulations. Finally,

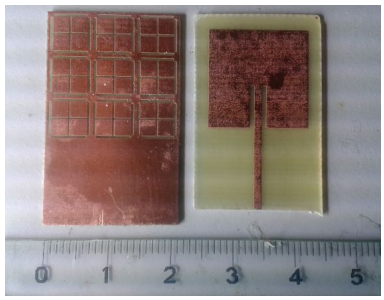

Fig. 2: Picture of the prototype antenna and its ground plane.

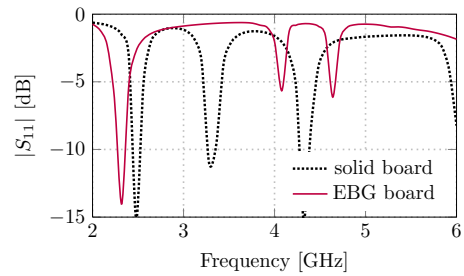

Fig. 3: Reflection coefficient for the two configurations.

Section IV summarizes the findings.

II. Theory and Set-up

A square patch antenna is chosen as the active element. Even though it can be objected that this configuration is not the most common one found in compact electronics devices, its advantages are many: a well-known radiation model; the amount literature on the interaction of plates with EBG structures; and its being compatible with product needs (cost, weight, mechanical integration, ...). Furthermore, the discussion can easily be extended without loss of generality to the parallel plate noise emitted from PCBs, due to the similar radiation mechanism, so to include resonances rooted into the geometry of ground and power planes, etc....

The modified antenna uses a ground plane on which is periodically etched a Jerusalem Cross pattern in a complementary fashion, as visible from the prototype picture in Fig. 2. This is a known planar implementation of an EBG structure, and allows a significant shrinking of the antenna dimensions. A simple model of EBG is used for design purposes [11], whereas tuning is left to parametric studies accomplished via software simulation [12]. Cost and space constraints, common to all mass produced products, dictates the use of a planar structure for the EBG implementation. The square patch antenna has a dimension of 16.3×16.3 mm and operates in the 2.4 GHz ISM band, it is fed via a recessed microstrip line, and it is implemented on a 0.8 mm thick FR-4 substrate. The work uses as reference a traditional patch antenna with a small solid ground plane.

The peculiarity, compared to other studies in the sector, of making use of an antenna as a radiation source, instead of a simple metal plate, find its reason in the focus on unwanted signals, e.g., power amplifier (PA) harmonics, coupled at the input of a structure actually intended to radiate and therefore potentially more critical for the EMC performance.

A major drawback of the set-up is that is not possible to focus on the radiation pattern. In fact, the latter is markedly different at the center frequency between the two configuration and is therefore not eligible to represent a comparison term. Nevertheless, in small antennas the metric of most interest is the antenna efficiency – that can be similarly expressed through the total radiated power (TRP):

$$TRP = P_{\text{cond}} \cdot \eta_{\text{rad}} \quad , \tag{1}$$

where P_{cond} is the conducted power of the radio and η_{rad} the radiation efficiency of the antenna. The results are therefore compared in terms of the radiation efficiency of the structure. This is defined as the power radiated by an antenna over the power accepted at its terminals, therefore the result is independent from the matching condition. Even though TRP is not necessarily the most indicative metric with respect to EMC testing, since it doesn't take into account the directionality of the radiation, it is the most effective in the present context.

III. Simulation Results

Fig. 3 shows the reflection coefficient for the two configurations. It is clearly noticeable how the EBG structures affects the resonance frequencies of the patch. It can also be read a slight improvement in bandwidth.

Fig. 4 shows the comparison between the simulated efficiency of the two antennas versus the frequency. The radiation efficiency is satisfactory in the operating band for both geometries, but it is appears clearly that the antenna based on the EBG substrate is more performing. At a certain point in frequency, the two curves assume the same value and for the whole frequency range above the EBG structure radiates instead less effectively. This is desirable, since it is going to reduce the level of the spurious emissions above the crossing frequency, in a more or less marked fashion as compared to the reference design.

A patch supports higher-order resonances, that radiates according to its characteristic modes. In proximity of these frequencies the impedance match improves and the radiation efficiency increases, but emissions are undesirable. On the other side, the efficiency decrement of the EBG patch attenuates these frequencies when the higher-order modes occur.

Fig. 5 shows the suppression factor as the ratio of the two different efficiencies, highlighting how the EBG based solution provides an improvement of over 1 dB within the 2.4 GHz ISM band (marked in blue), while it rejects frequencies above $f_{\text{c}} = 3.05$ GHz from a minimum of 1 up to over 10 dB. The higher-order resonances of the structures makes it radiating

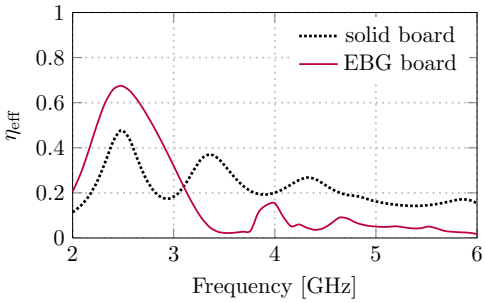

Fig. 4: Efficiency versus frequency for the two antennas: solid ground (solid line) and EBG ground (dashed line).

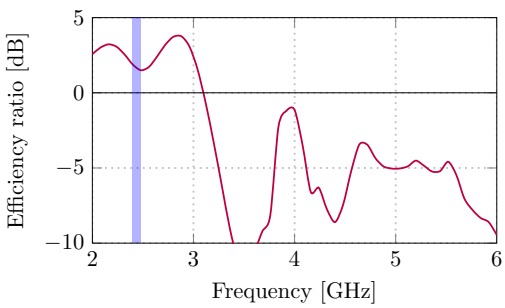

Fig. 5: Another representation of the maximum rejection achievable, with the ratio between the EBG plane over the solid plane expressed in dB. The 2.4 GHz ISM band is highlighted in blue.

far beyond the required frequency range. On the contrary, the EBG plane effectively inhibits such mechanism.

This apparently contradicts the praxis, that wants solid ground planes to be one of the most robust solution to decrease the risk of EMC issues from PCB boards. Instead, in cases in which direct coupling to the antenna feed or parallel plate noise can arise, an EBG etched layer can improve such performance attenuating the higher-order resonances. Nevertheless, we shall not forget that in an integrated product, the same ground plane is shared by other functions, as can be ICs or audio components, so that further investigation with focus on signal integrity performance is necessary before prematurely drawing the above-mentioned conclusion.

IV. Conclusion

A patch antenna implemented on an EBG ground plane was investigated in this paper, and its advantages for product integration examined. In particular, it was noted that such an antenna may obtain higher efficiency while dimensions are shrunk as compared to a traditional design. The advantage is strengthen by the fact that the antenna is more frequency selective, i.e., it attenuates frequencies above a certain frequency f_c. This helps both into attenuating higher order harmonics and other unwanted radiation of an amount from a few dB up to 10 and above. Implementation in compact electronic products is advised, when complemented by a careful signal integrity analysis.

References

[1] S. H. Kvist, J. Thaysen, and K. B. Jakobsen, "Improvement of the Ear-to-Ear Path Gain At 2.45 GHz Using Parasitic Antenna Element," *6th European Conference on Antennas and Propagation*, vol. 2, pp. 944–947, 2011.

[2] F. D. Paulis and L. Raimondo, "Compact Configuration for Common Mode Filter Design based on Planar Electromagnetic Bandgap Structures," *IEEE Transactions on Electromagnetic Compatibility*, vol. 54, no. 3, pp. 646–654, 2012.

[3] S. Shahparnia and O. Ramahi, "Electromagnetic interference (EMI) reduction from printed circuit boards (PCB) using electromagnetic bandgap structures," *IEEE Transactions on Electromagnetic Compatibility*, vol. 46, no. 4, pp. 580–587, 2004.

[4] J. Qin, O. Ramahi, and V. Granatstein, "Novel planar electromagnetic bandgap structures for mitigation of switching noise and EMI reduction in high-speed circuits," *IEEE Transactions on Electromagnetic Compatibility*, vol. 49, no. 3, pp. 661–669, 2007.

[5] M. Kim, K. Koo, C. Hwang, Y. Shim, J. Kim, and J. Kim, "A Compact and Wideband Electromagnetic Bandgap Structure Using a Defected Ground Structure for Power/Ground Noise Suppression in Multilayer Packages and PCBs," *IEEE Transactions on Electromagnetic Compatibility*, vol. 54, no. 3, pp. 689–695, Jun. 2012.

[6] M. M. Bait-Suwailam and O. M. Ramahi, "Ultrawideband Mitigation of Simultaneous Switching Noise and EMI Reduction in High-Speed PCBs Using Complementary Split-Ring Resonators," *IEEE Transactions on Electromagnetic Compatibility*, vol. 54, no. 2, pp. 389–396, Apr. 2012.

[7] A. Ruaro, J. Thaysen, and K. B. Jakobsen, "Metamaterial-inspired Near-field Resonant Parasitic Structure for Directional Suppression of Narrow-band EMI/RFI in Compact Systems," in *2013 National Radio Science Meeting (NRSM) (Joint with AP-S Symposium)*, 2013.

[8] ——, "Mitigation of Unwanted Forward Narrow-band Radiation from PCBs with a Metamaterial Unit Cell," in *2013 European Microwave Conference (EuMC)*, 2013.

[9] J. Liang and H. D. Yang, "Radiation Characteristics of a Microstrip Patch Over an Electromagnetic Bandgap Surface," *IEEE Transactions on Antennas and Propagation*, vol. 55, no. 6, pp. 1691–1697, 2007.

[10] H. Mosallaei and K. Sarabandi, "Antenna Miniaturization and Bandwidth Enhancement Using a Reactive Impedance Substrate," *IEEE Transactions on Antennas and Propagation*, vol. 52, no. 9, pp. 2403–2414, 2004.

[11] K. H. Kim and J. E. Schutt-ainé, "Design of EBG Power Distribution Networks With VHF-Band Cutoff Frequency and Small Unit Cell Size for Mixed-Signal Systems," *IEEE Microwave and Wireless Components Letters*, vol. 17, no. 7, pp. 489–491, 2007.

[12] Ansys®, HFSS, Release 13.0.

Paper 5

"Compact and Ultra-Low-Power 2.4 GHz LNA for On-body Communication Devices"

A. Ruaro, S. Gülstorff, J. Thaysen, and K. B. Jakobsen

[P5] A. Ruaro, S. Gülstorff, J. Thaysen, and K. B. Jakobsen, "Compact and ultra-low-power 2.4 GHz LNA for on-body communication devices", in *Proceedings of the Radio and Antenna Days of the Indian Ocean (RADIO)*, 2015.

Compact and Ultra-Low-Power 2.4 GHz LNA for On-body Communication Devices

Andrea Ruaro*†, Steen Gülstorff*, Jesper Thaysen*, and Kaj B. Jakobsen†

*GN ReSound A/S, Lautrupbjerg 7, DK-2750 Ballerup, Denmark
†Department of Electrical Engineering, Technical University of Denmark, DK-2800 Lyngby, Denmark

***Abstract*—The development and characterization of an extremely compact, ultra-low-power, and detuning-robust Low Noise Amplifier (LNA) for Wireless Body Area Network (WBAN) applications is presented in this paper. The amplifier is designed and then implemented with only seven high-density surface-mount components. The noise figure is as low as 1.5 dB with an associated power gain of 6.2 dB while it consumes less than 1 mW drawn from a 1 V supply. The input third-order intercept point ($\mathrm{IIP_3}$) and the 1-dB compression point ($\mathrm{P_{1dB}}$) are -11 and -9 dBm, respectively. The input and output return loss are better than 6 dB and 14 dB, respectively, in the 2.45 GHz ISM band.**

I. Introduction

Hearing Instruments (HI) joined the wireless connected world and are among the emerging applications in the Wireless Body-Area Networks (WBAN) sector. In general, wearable electronics and on-body sensors drew much interest in recent times from both the scientific community and the industry. According to the characteristics of the specific link that has to be ensured and on the devices' form factor, some applications are particularly demanding, as is the case of the Ear-to-Ear (E2E) link [1]. Devices that are to be wireless connected, wearable, and unobtrusive face serious challenges in power consumption and size. A well known trade-off is that between the receiver sensitivity and power consumption. Here, a key parameter is the noise figure NF of the receiver chain that directly affects the overall effectiveness of the receiver.

At present, taken into consideration the whole set of applications, there are limits to the possibility of achieving very low noise figure with RF CMOS technology [2]–[8]. The state-of-the-art values, reported in Table I, are unsuitable for the on-body applications demand as, e.g., in the case of the hearing instruments. This is due to the characteristic of the on-body channel that calls for an enhanced receiver sensitivity. Thus, unlike other amplifier designs, a solution that aims to achieve low noise figure together with ultra-low-power operation and that ensures a sufficient robustness to antenna detuning has to be implemented through the use of high-density surface-mount components—even if this sets strong limitations on the design complexity and size.

For the first time in literature, is proposed in this study a design that optimizes the noise figure with reduced power consumption while it uses a limited amount of components and improves the robustness to antenna detuning.

TABLE I
State-of-the-art CMOS LNAs

NF (dB)	P_{DC} (mW)	V_{DD} (V)	G_{a} (dB)	IIP_3 (dBm)	Node (nm)	Year (-)	Ref. (-)
1.6	7.2	1.8	14.1	$+1$	180	2011	[2]
2.7	0.4	1.2	22.8	$+3$	180	2011	[3]
2.9	1.1	0.6	10.9	0	180	2013	[4]
4.0	1.3	1.2	20.0	-12	130	2011	[5]
4.4	0.7	1.2	9.7	-4	90	2014	[6]
4.8	0.6	1.8	14.7	$+2$	180	2014	[7]
5.2	0.9	1.5	21.4	-11	180	2008	[8]
1.5	1.0	1.0	6.2	-11	n/a	This work	

II. Circuit Design

The sensitivity of the receiver is a function of many parameters, among others: demodulator properties, bandwidth, and noise figure. According to well-known Friis formula, it is possible to improve the latter through the placement of an amplifier with low noise figure in front of the receiver chain. The present study comprises of the development and characterization of a Low Noise Amplifier (LNA) where the aim is to achieve a noise figure as low as possible, and in any case below 2 dB, while draining a maximum power of 1 mW.

The prototype is implemented on a FR-4 custom PCB with commercially available components. It is constructed by one transistor (Q_1, Renesas Electronics NESG3031M14) and only six lumped elements with the architecture shown in Fig. 1. In particular, an inductively-degenerated common-source topol-

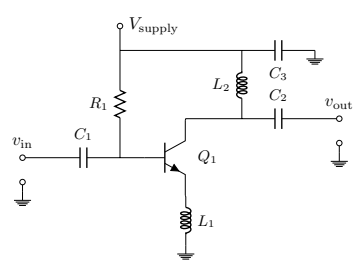

C_1	22	pF
C_2	0.7	pF
C_3	1.5	pF
L_1	0.9	nH
L_2	3.2	nH
R_1	75	kΩ

Fig. 1. Diagram of the compact LNA and list of component values.

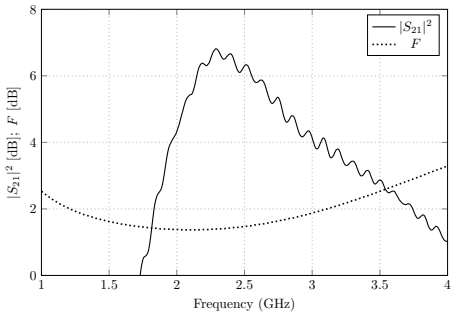

Fig. 2. Measured insertion power gain (solid line) and computed noise figure (dotted line) for the LNA in a wide frequency interval including the 2.45 GHz ISM band.

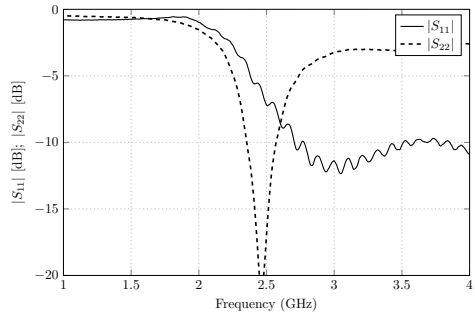

Fig. 3. Input and output reflection coefficients (solid and dotted line, respectively) of the compact LNA.

ogy has been chosen for its good noise performance while it eases the device stabilization with a limited amount of components. A single source inductor is used. A passive bias circuit has been preferred in order to meet the power limitations. The device is designed for low-voltage operation, thus to make it suitable for battery applications down to as low as 1.0 V only. The output is impedance matched. Please note, a tuned circuit has been discarded due to the fact that at least two more components were needed in order to obtain a high-Q network. In fact, the LNA can ultimately be fitted in a very small area.

The overall transceiver performance can be seriously affected by the detuning of the antenna, in particular in the case where an LNA is the first block at the receiver. The impedance can move in an unpredictable way as seen at the input port of the transistor. This worsens the trade-off made between noise and impedance matching carefully chosen by the designer. A low-Q input matching network was proven able to maintain a certain degree of robustness to detuning [9] and has thus been preferred here.

III. Measurement Results

The measured insertion power gain performance and the computed noise figure of the device are shown in Fig. 2. The measured noise figure of the LNA is $NF < 1.5$ dB in the whole 2.45 GHz ISM band. The wideband profile is henceforth determined. The uncertainty on the noise figure is ± 0.4 dB, mainly due to the high $VSWR$ at the input of the measurement system. The associated gain is $G_{\mathrm{a}} = 6.2$ dB, with an in-band peak-to-peak difference below 0.6 dB.

The input and output reflection coefficients are plotted in Fig. 3 and show the wide bandwidth covered by the input matching network at the price of accepting higher values of S_{11}. The input reflection coefficient is below -6 dB for the frequencies above 2.4 GHz, while the output reflection coefficient is below -14 dB in the 2.45 GHz ISM band. The linearity performance of the amplifier is satisfactory, i.e., $IIP_3 = -11$ dBm and $P_{1\mathrm{dB}} = -9$ dBm.

IV. Conclusion

The inadequacy of CMOS technology for high-performance ultra-low-power applications required by emerging on-body communications devices has been discussed. A suitable LNA space-saving design has been proposed. The compact, ultra-low-power amplifier has been implemented with high-density surface-mount components and fulfils the requirements. The current drain is 1 mA from a 1.0 V supply only. The design uses a total of only 7 components with an overall sum of component surface of 2.04 mm^2, that can be fitted into an area as small as 2.5 mm $\times$ 1.5 mm.

References

[1] B. C. Kirkwood, S. A. Hallenbeck, and T. Stender, "How can wireless data exchange in hearing instruments contribute to binaural hearing?," *Hearing Review*, Vol. 19, No. 10, pp. 52–55, 2012.

[2] Z. Li, L. Chen, and H. Zhang, "Design and optimization of CMOS LNA with ESD protection for 2.4 GHz WSN application," *Journal of Semiconductors*, Vol. 32, N. 10, 2011.

[3] J. L. Gonzalez, H. Solar, I. Adin, D. Mateo, and R. Berenguer, "A 16-kV HBM RF ESD Protection Codesign for a 1-mW CMOS Direct Conversion Receiver Operating in the 2.4-GHz ISM Band", *IEEE Transactions on Microwave Theory and Techniques*, Vol. 59, N. 9, 2011.

[4] Jian-Ming Wu and Yan-Tsang Lin, "A Solar-Powered 2.4-GHz LNA RFIC," *Microwave and Optical Technology Letters*, Vol. 55, N. 10, pp. 2377–2380, 2013.

[5] F. Belmas, F. Hameau, and J. Fournier, "A 1.3mW 20dB Gain Low Power Inductorless LNA with 4 dB Noise Figure for 2.45 GHz ISM Band," in *IEEE Radio Frequency Integrated Circuits Symposium*, 2011.

[6] R. Fiorelli, F. Silveira, and E. Peralas, "MOST moderate-weak-inversion region as the optimum design zone for CMOS 2.4-GHz CS-LNAs," *IEEE Transactions on Microwave Theory and Techniques*, Vol. 62, N. 3, pp. 556–566, 2014.

[7] Zhiqun Li *et al.*, "A 2.4 GHz Ultra-Low-Power Current-Reuse CG-LNA With Active Gm-Boosting Technique," *IEEE Microwave and Wireless Components Letters*, Vol. 4, N. 5, pp. 348–350, 2014.

[8] V. Aaron *et al.*, "A Subthreshold Low-Noise Amplifier Optimized for Ultra-Low-Power Applications in the ISM Band," *IEEE Transaction on Microwave Theory and Techniques*, Vol. 56, N. 2, pp. 286–292, 2008.

[9] A. Ruaro, S. H. Kvist, S. Gülstorff, J. Thaysen, and K. B. Jakobsen, "Influence of the Antenna Impedance Variation and Input Matching Network Q on LNA Key Figures," in *Loughborough Antennas and Propagation Conference (LAPC)*, 2012.


IEEE RADIO 2015
IEEE RADIO AND ANTENNA DAYS OF THE INDIAN OCEAN
21 – 24 SEPTEMBER 2015, MAURITIUS
This acknowledges that
Andrea RUARO
has received, in recognition of the quality, originality and significance for the work entitled
Compact and ultra –low-power 2.4 GHz LNA for on-body communication devices
co-authored with
Steen Gulstorff, Jesper Thaysen and Kaj B. Jakobsen
the
Second Prize
for the
Best Student Paper Award
Prof. Vikass Monebhurrun
General Chair, IEEE RADIO 2015
24 September 2015

Paper 6

"Influence of the Antenna Impedance Variation and Input Matching Network Q on LNA Key Figures"

A. Ruaro, S. Kvist, S. Gülstorff, J. Thaysen, and K. B. Jakobsen

[P6] A. Ruaro, S. Kvist, S. Gülstorff, J. Thaysen, and K. B. Jakobsen, "Influence of the antenna impedance variation and input matching network Q on LNA key figures", in *Proceedings of the Loughborough Antennas and Propagation Conference (LAPC)*, 2012.

Influence of the Antenna Impedance Variation and Input Matching Network Q on LNA Key Figures

Andrea Ruaro*, Søren H. Kvist*†, Steen Gülstorff†, Jesper Thaysen†, and Kaj B. Jakobsen*
*Department of Electrical Engineering, Technical University of Denmark, DK-2800 Lyngby, Denmark
†GN ReSound A/S, Lautrupbjerg 7, DK-2750 Ballerup, Denmark

***Abstract*—In this paper we present an analysis of the behaviour of a 2.4 GHz Low Noise Amplifier (LNA) for Wireless Body Area Network (WBAN) applications facing antenna-detuning issue. An amplifier with ultra-low power, low voltage, and with reduced component count is prototyped to validate simulation results, then the behaviour is analyzed through simulations based on data measured on real users.**

The analysis shows that the designed LNA is stable to the antenna impedance variation expectable in most cases, while highlights the possible risks associated to a high-Q input matching network when used in a context prone to antenna detuning risk.

I. Introduction

The scientific and commercial interest in wireless body-area network (WBAN) is steadily growing in recent years. In general, today the healthcare, consumer and military industry is acting as a driver for the study of body-centric communications. Compared to other communication systems, these applications hold distinctive features due to the behavior of the channel and thus require specific, highly-efficient antenna solutions [1], [2]. In particular, the Hearing Instruments (HI) industry is concerned in on-body communications, i.e., those occurring between two sensor nodes placed in close proximity to the body, since it is of high interest for manufacturers to transmit data packages between two devices each placed at one ear. Among the major issues that have to be faced, are the characterization of the channel, not line-of-sight communications performance, and multipath fading in indoor environments [3]. Furthermore, the front-end of such devices has to be robust to detuning of the antenna, a well-known issue present in other application sectors like RFID tags and handheld antennas, e.g., for the mobile industry [4], [5].

The consequences of the variation of the antenna input impedance on an LNA performance have to be evaluated in the case of a simple input matching network of arbitrary loaded quality factor Q. Usually, the choice of the Q factor value is based on circuit requirements: a high-Q network, for instance, enhances the rejection of out-of-band interference, while a low-Q network is less subjected to variation in production (due to components' uncertainty) and requires a lower number of component, resulting thus cheaper. It is then interesting to structure a study of the influence of the antenna impedance variation on an LNA key figures as a function of the Q-factor of the amplifier input matching network.

II. Circuit Design and Validation

The receiver sensitivity, that the designed LNA is called to enhance, is a function of many parameters, like demodulator properties, bandwidth, and noise figure. It is possible to improve the latter according to well-known Friis formula, i.e., placing an amplifier with low noise figure F_1 and high available gain G_1 in front of the receiving chain:

$$F_{\text{sys}} = F_1 + \frac{F_2 - 1}{G_1}, \tag{1}$$

where F_2 is the noise figure of the receiver itself. Hence the need to develop an LNA robust to antenna detuning and with a significantly low noise figure. According to the state-of-the-art performance collected by the authors, in fact, the lowest measured noise figure achieved with RF CMOS technology in the 2.4 GHz ISM band with an ultra-low power consumption, intended here as less or approximately equal to 1 mW, is 2.7 dB [6]; whereas, a noise figure of approximately 1.6 dB is found only at a consistently higher $P_{\text{DC}} = 7$ mW [7].

The amplifier presented here is designed for low-voltage operation, thus to make it suitable for battery applications down to 1.0 volt. This value is a worst-case representative of the whole span of voltage that the batteries provide during their active life. Equally important, the operating time of such devices is strictly connected to the power consumption, hence the need of an ultra-low power design. Furthermore, in the HI application the overall occupied space is of primary importance, and space shrinking for a device implemented through high-density surface-mounts components has to pass through the reduction of the parts count.

The LNA has been implemented in order to validate the simulation results, that were subsequently adjusted to fit measurements. The main parameters, simulated and measured, are reported in Table I. The tuned simulation proved to be reliable and thus the simulated results based on actual test-user data are considered trustworthy, when read in a qualitative way.

A. Input Matching for Detuning Robustness

Detuning of the antenna is an issue that can seriously affect the performance, in particular in the case where an LNA is directly connected to the antenna. The source impedance can move in an unpredictable way as seen at the input port of the transistor. This worsens the trade-off made between noise and impedance matching even when it is carefully chosen by

978-1-4673-2220-1/12/$31.00

TABLE I
COMPARISON OF SIMULATED AND MEASURED IN-BAND VALUES FOR THE COMPACT LNA.

	Sim.	Meas.	Unit
G_a	6.3	6.2	dB
F	1.4	1.5	dB
$P_{1\text{-dB}}$	—	-9	dBm
IIP_3	—	-11	dBm
Input RL	>6	>6	dB
Output RL	>14	>14	dB

the designer. Active approaches (non-Foster and auto-tuning) have been investigated in the past but are not suitable in the present application due to their physical dimension and power consumption [4]. Therefore, the choice made was to implement a low-Q input matching in order not to affect the antenna bandwidth, so to maintain a certain degree of robustness to detuning [5]. The input is noise matched, where the antenna impedance is determined with the least squares method from data measured on different test users.

A change in the source impedance modifies the input impedance, or equivalently the input admittance, as seen from the transistor through the input matching network. This $\Delta Y_\mathrm{S} = \Delta G_\mathrm{S} + \Delta B_\mathrm{S}$ difference may then possibly cause a worsening in the associated gain ΔG_a and in the noise figure ΔF, given in the case of a 2-port network by:

$$F = F_\mathrm{min} + \frac{R_\mathrm{N}}{G_\mathrm{S}}|Y_\mathrm{S} - Y_\mathrm{opt}|^2, \tag{2}$$

with the terms defined as usual [8]. The variation of the noise figure due to a source admittance $Y_\mathrm{S} = Y_\mathrm{opt} + \Delta Y_\mathrm{S}$ is easily quantifiable to be:

$$\Delta F = \frac{R_\mathrm{N}}{G_\mathrm{S} + \Delta G_\mathrm{S}}|\Delta Y_\mathrm{S}|^2, \tag{3}$$

whereas the consequences on the associate gain are not so straightforward due to the involvement of other parameters in the 2-port network in the transducer gain formula [8].

III. RESULT DISCUSSION

Differently from handheld devices, where is the position of the user hand that characterize the impedance at the antenna terminals, in the HIs this is determined by the physical shape of the user head and ears, and by the fitting position. At present no proof of a correlation between it and the user head shape has been shown. The impedance at the antenna terminals varies in both real and imaginary part, and this differentiates the antenna performance for every single user, as can be seen from Fig.1, where is displayed the input impedance of an HI antenna from measurement on different test users.

Due to the small dimensions of the antenna, the system is too sensitive to external factors (e.g., the mechanics) to allow accurate measurements of the setup including the LNA.

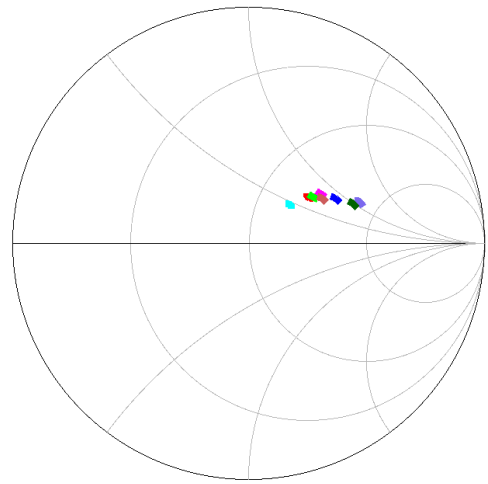

Fig. 1. Antenna impedance values extrapolated from measurements on several test users.

Specific loads could be built to emulate the known user impedance values, but this solution is as well not viable since they can't be characterized with enough precision. Furthermore, due to its magnitude the influence on the system is not easily measurable, thus a simulation is the only way to proceed in order to provide a qualitative analysis of the LNA behaviour.

Table II presents the worst-case deviation of the noise figure and gain from the designed value for 8 test-users, i.e., the maximum worsening to which the noise figure is subjected and the lowest gain relative value within the 2.4 GHz ISM band. The noise figure is compared to the minimum achievable noise figure, while the associated gain deviation takes into account the different gain profile due to the different matching networks. The subscript '$-$', '0', or '$+$' indicates if the maximum worsening occurs at lower band edge, center band, or upper band edge, respectively. It is noticed that in most cases (six over eight) the worsening is small in absolute value, thus confirming the robustness of the LNA's key figures to variation of the source impedance. The table also shows that the worst-case noise figure is associated in all the cases with the high-Q matching network, together with a decrease in the gain occurring at least in a fraction of the band. Case 5 exhibits the highest worsening in noise figure between the two matching networks, where the difference is more than 0.3 dB. It is possible to obtain improvement in the gain (the amplifier is noise matched): cases 4 ans 8 have a comparable noise figure worsening, but significantly different behaviour for what concern the gain. With an *a priori* knowledge of the impedance variation, it would be possible to design an LNA that takes advantage of this feature. In two cases (users 5 and 7), where the antenna impedance is markedly different, there

TABLE II
WORST-CASE DEVIATION OF NOISE FIGURE AND ASSOCIATED GAIN FOR DIFFERENT TEST USERS. THE SUBSCRIPT '−', '0', OR '+' INDICATES IF THE MAXIMUM WORSENING OCCURS AT LOWER BAND EDGE, CENTER BAND, OR UPPER BAND EDGE, RESPECTIVELY.

	$\Delta F_{\max}$ [dB]		$\Delta G_{\mathrm{a,min}}$ [dB]	
User	Low Q	High Q	Low Q	High Q
1	0.15_{+}	0.39_{-}	-0.10_{+}	-0.66_{-}
2	0.06_{+}	0.22_{-}	$+0.29_{+}$	-0.46_{0}
3	0.09_{+}	0.30_{-}	$+0.14_{+}$	-0.56_{0}
4	0.06_{+}	0.28_{+}	$+0.44_{+}$	-0.50_{+}
5	0.29_{+}	0.60_{-}	-0.61_{+}	-0.48_{0}
6	0.07_{+}	0.25_{-}	$+0.24_{+}$	-1.34_{-}
7	0.26_{+}	0.53_{-}	-0.46_{+}	-1.12_{-}
8	0.09_{0}	0.25_{-}	$+0.11_{+}$	-0.50_{0}

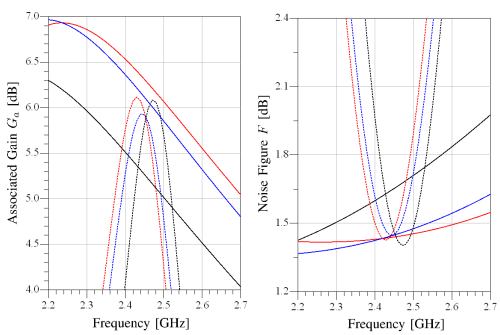

Fig. 2. Gain (left) and noise figure (right) for the LNA with the designed input matching network (solid line) and with a high-Q input matching network (dotted line, loaded Q equal to $Q_1 = 15$). The curves refer to test user 3 (red line), 4 (blue line) and 5 (black line).

is instead a significant worsening in both figures.

In Fig. 2 the key figures of the amplifier for test users 3, 4, and 5 are shown. The two families of curves are representative of the cases of a low-Q and of a high-Q input matching network. Values can be read directly from the plots. Even though the variation of the input impedance is not directly dependent on the Q-factor of the matching circuit, it can be noticed that if the matching is wideband, then the roll-off of the gain and noise figure curves is also wideband. This means that for a high-Q network, when the source is mismatched the worsening in the amplifier key figures due to the different reflection coefficient can become severely more marked due to the steepness of the curves.

IV. CONCLUSION

An ultra-low power, low voltage and reduced-size LNA for use in 2.4 GHz on-body communications application has been developed and characterized. The behaviour of the specific amplifier design has been analyzed with respect to the source impedance variation caused by the detuning of the antenna, showing how a low-Q input matching network allows to obtain only slight worsening in the majority of cases.

It is thus recommended, when dealing with the design of LNAs in association with antenna detuning risk, to take into consideration the influence on noise figure and gain of the input network Q factor. In fact, even though the variation of the key parameters shown here is not necessarily critical in itself, it can be enhanced by the high roll-off profile of the noise figure and gain curves associated with high-Q narrowband networks.

V. ACKNOWLEDGEMENTS

The authors would like to thank Birol Akdeniz for providing test-user measurement data.

REFERENCES

[1] P. S. Hall, Y. Hao, "Antennas and Propagation for Body Centric Communications", *European Conference on Antennas and Propagation*, 2006.

[2] Y. Hao, A. Alomainy, P. S. Hall, Y. I. Nechayev, C. G. Parini, C. C. Constantinou, "Antennas and Propagation for Body Centric Wireless Communications". In: *IEEE/ACES International Conference on Wireless Communications and Applied Computational Electromagnetics*, 2005.

[3] Søren H. Kvist, Jesper Thaysen, Kaj B. Jakobsen, "Ear-to-Ear On-Body Channel Fading in the ISM-band for Tangentially-Polarized Antennas", *Loughborough Antennas and Propagation Conference*, 2011.

[4] Kevin Boyle, Theo Bakker, Maurice de Jongh, Andre van Bezooijen, "Real-time Adaptation of Mobile Antenna Impedance Matching", *Loughborough Antennas and Propagation Conference*, 2010.

[5] Jingtian Xi and Terry T. Ye, "Wideband and Material-insensitive RFID Tag Antenna Design Utilizing Double-tuning Technique". In: *IEEE International Symposium on Antennas and Propagation (APSURSI)*, pp. 545-548, 2011.

[6] J.L. Gonzalez, H. Solar, I. Adin, D. Mateo, and R. Berenguer, "A 16-kV HBM RF ESD Protection Codesign for a 1-mW CMOS Direct Conversion Receiver Operating in the 2.4-GHz ISM Band", *IEEE Transactions on Microwave Theory and Techniques*, Vol. 59, N. 9, 2011.

[7] Zhiqun Li, Liang Chen, and Hao Zhang, "Design and optimization of CMOS LNA with ESD protection for 2.4 GHz WSN application", *Journal of Semiconductors*, Vol. 32, N. 10, 2011.

[8] D. M. Pozar, *Microwave Engineering*. John Wiley and Sons, Inc., 3 ed.

Paper 7

"Cavity-backed on-body antenna for custom hearing instrument applications"

A. Ruaro, J. Thaysen, and K. B. Jakobsen

[P7] A. Ruaro, J. Thaysen, and K. B. Jakobsen, "Cavity-backed on-body antenna for custom hearing instrument applications", *IET Electronics Letters*, 2015.

Cavity-backed on-body antenna for customised hearing instrument applications

A. Ruaro, J. Thaysen and K.B. Jakobsen✉

A novel on-body antenna targeted for 2.45 GHz customised in-the-ear hearing instrument applications is designed, implemented, and measured. The antenna is designed to use the maximum volume available in the user's ear canal and to provide isolation from the user's body. The polarisation is primarily normal to the surface of the head to ensure the best on-body path gain. Efficiency and *S*-parameters from measurements in free space and on a specific anthropomorphic mannequin head endowed with ears are presented.

Introduction: Wearable devices connected into wireless body area networks are key enablers of the Internet of things. The scientific interest in their operation and related applications has significantly grown in recent years. These devices demand solutions within the 2.4 GHz ISM band, and their form factor (low profile and small size) is very challenging from the perspective of the antenna design. In particular, the hearing instrument industry is looking into solutions to connect two devices placed on the opposite sides of the head, i.e. to establish an ear-to-ear link. This would allow real-time data exchange between the devices and thus directly benefit the end users [1]. Recently, a few solutions have been proposed [2, 3]; however, it will be shown in the following that the radiation efficiency can be improved even further, with a direct impact on the link budget and power consumption. To the best of the authors' knowledge, it is the first time that a cavity-backed design is proposed for a head-worn antenna. This antenna satisfies the requirement of high radiation efficiency when placed inside a user's ear.

Design and implementation: The novel antenna concept is shown in Fig. 1 in a generalised geometry. The main radiating element consists of a curled wire lying on, or parallel above, the *xy*-plane. When the antenna is placed on-body the *z*-axis is normal to the head surface, i.e. it defines the θ-component with respect to the *xy*-plane.

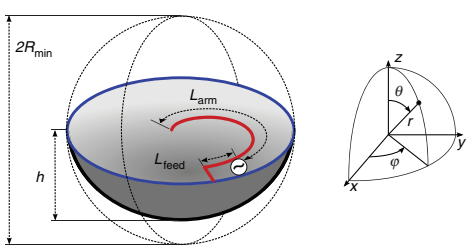

Fig. 1 *Novel antenna concept shown in three-dimensional perspective*

The wire radiator is bent over a hemispherical ground plane. The additional capacitance, due to the reduced distance to the ground plane, is balanced by the introduction of a shorting pin that acts as a parallel inductance. The wire, the feed, and the shorting pin are coplanar. The distance and the width of the shorting pin are chosen in order to improve the impedance bandwidth. The antenna arm is slightly shorter than $\lambda/4$. By experimentation it was determined that a length $L_{\text{feed}} = 3$ mm was the optimal distance for a proper impedance match. The result is an antenna that is well matched at its centre frequency f_{centre}.

The design is such that the location of the maximum *E*-field is placed above a current minimum on the ground plane. The structure is therefore equivalent to a small electrical dipole oriented along the *z*-axis. This allows for a creeping wave to be launched on the body surface in an optimal way.

The shape of a customised in-the-ear (ITE) hearing instrument is based on the morphology of each user's ear canal. An impression of the ear is taken, and based on its negative mould a plastic part is then cast. To reproduce such a process, in this experiment an expanding foam has been injected into a specific anthropomorphic mannequin (SAM) ear. Given the high concentration of air bubbles in the foam, the relative dielectric constant is assumed to be close to that of air, i.e. $\varepsilon_{\text{r,foam}} \approx \varepsilon_{\text{r,air}} = 1$. This cast is less of an ideal case with respect to the model previously described, but on the other hand it allows for measurements on the SAM head and is much closer to the actual implementation. The foam shape is then conformally covered with a conductive layer of aluminium, whereas the active arm is made of copper. This allows for the use of all the available volume and thus increases that occupied by the antenna within the sphere of a given radius encompassing it. The height h is set to the depth of the ear canal. This results in an overall lower Q factor, i.e. wider bandwidth [4].

The design parameters for the antenna are given in Table 1. The radius of the minimum sphere encompassing the active element is $R_{\text{min,arm}} = 7$ mm, whereas the whole antenna fits in a sphere of radius $R_{\text{min}} = 16.5$ mm. The antenna is fed via a semi-rigid coaxial cable. A $\lambda/4$ bazooka balun is soldered on the cable in order to suppress spurious radiation caused by the currents that may flow on the outer conductor of the cable. The antenna profile, shown in Fig. 2, is low on the ear and does not exceed its depth. This is a realistic representation of customised ITE hearing instruments. A photograph of the prototype is also shown in Fig. 2.

Table 1: Antenna design parameters (in millimetres)

R_{min}	16.5
h	10.0
L_{arm}	24.0
L_{feed}	3.0

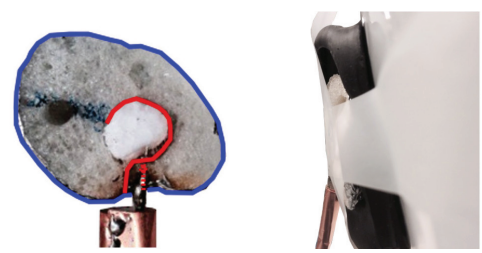

Fig. 2 *Prototype photograph, front view (left) and fitting profile of antenna when placed in SAM phantom ear, side view (right)*

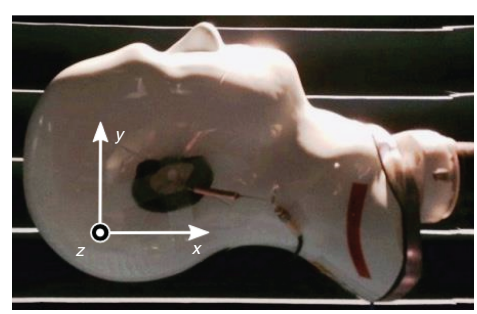

Fig. 3 *Photograph of measurement setup, with antenna coordinate system*

Measurement results: The proposed antenna was measured in an anechoic chamber in two different configurations: in free space, for reference; and on-body, as it is meant to operate on an actual user. A SAM head endowed with ears is used in the latter case. The SAM's ears are made of a material with RF properties similar to those of real ear tissues. The measurement coordinate system is centred at the antenna, with the *z*-axis normal to the head surface. The probe is located in the antenna far-field. The antenna is fitted within the SAM's ear, with the feed cable directed towards the pinna along the *x*-axis as can be seen from Fig. 3. The measured reflection coefficient and radiation efficiency are shown in Figs. 4 and 5, respectively.

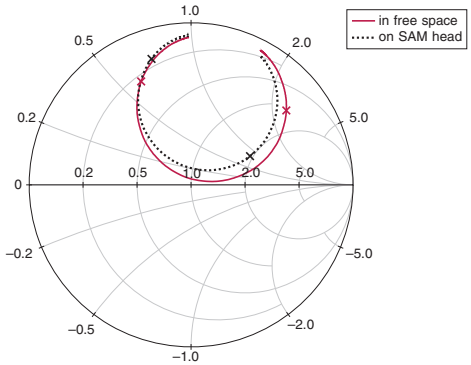

Fig. 4 *Antenna reflection coefficient in free space (black dotted line) and on SAM head (red solid line) shown on Smith chart (normalised to 50 Ω). Frequency range spans from 2.3 to 2.6 GHz, whereas markers (×) delimit the 2.45 GHz ISM band*

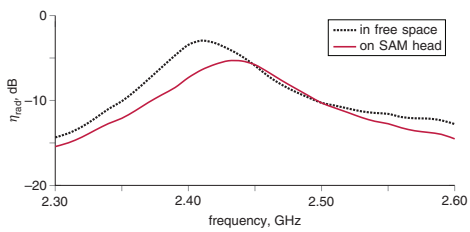

Fig. 5 *Antenna radiation efficiency in free space (black dotted line) and on SAM head (red solid line)*

The antenna has a medium bandwidth. This is due to the fact that most of the energy is confined within the antenna's volume, which results in an increased Q factor. Further results on the antenna's performance can be found in Table 2.

Table 2: Antenna performance

	In free space	On SAM head	
$BW_{6\ dB}$	44.0	48.5	MHz
f_{centre}	2.41	2.43	GHz
η_{peak}	51%	29%	—

Conclusion: A novel conformal cavity-backed antenna for ITE use is introduced. The antenna exhibits high radiation efficiency when measured on-body due to the shielding effect provided by the ground plane. The on-body efficiency peaks at −5.3 dB (29%).

Submitted: *17 March 2015*
doi: 10.1049/el.2015.0899
One or more of the Figures in this Letter are available in colour online.

A. Ruaro and K.B. Jakobsen (*DTU Electrical Engineering, Technical University of Denmark, DK-2800 Kongens Lyngby, Denmark*)

✉ E-mail: kbj@elektro.dtu.dk

J. Thaysen (*GN ReSound A/S, DK-2750 Ballerup, Denmark*)

References

1 Kirkwood, B.C., Hallenbeck, S.A., and Stender, T.: 'How can wireless data exchange in hearing instruments contribute to binaural hearing?', *Hear. Rev.*, 2012, **19**, (10), pp. 52–55
2 Yatman, W.H., Larsen, L.K., Kvist, S.H., Thaysen, J., and Jakobsen, K. B.: 'In-the-ear hearing-instrument antenna for ISM-band body-centric ear-to-ear communications'. Loughborough Antennas and Propagation Conf. (LAPC), Loughborough, UK, November 2012
3 Kammersgaard, N.P.I., Kvist, S.H., Thaysen, J., and Jakobsen, K.B.: 'In-the-ear spiral monopole antenna for hearing instruments', *Electron. Lett.*, 2014, **50**, (21), pp. 1509–1511
4 Yaghjian, A.D., and Best, S.R.: 'Impedance, bandwidth, and Q of antennas', *IEEE Trans. Antennas Propag.*, 2005, **53**, (4), pp. 1298–1324

Paper 8

"Rapid Prototyping Analysis and Modeling of a Small Antenna for Binaural Hearing Aids"

A. Ruaro, J. Thaysen, and K. B. Jakobsen

[P8] A. Ruaro, J. Thaysen, and K. B. Jakobsen, "Rapid prototyping analysis and modeling of a small antenna for binaural hearing aids", in *Proceedings of the International Symposium on Antennas and Propagation (ISAP)*, 2015.

Rapid Prototyping of an Electrically-Small Antenna for Binaural-Hearing Instruments

Andrea Ruaro*†, Jesper Thaysen*, and Kaj B. Jakobsen†

*GN ReSound A/S, Lautrupbjerg 7, DK-2750 Ballerup, Denmark
†Department of Electrical Engineering, Technical University of Denmark, DK-2800 Lyngby, Denmark

***Abstract*—Rapid prototyping is emerging as a technology that can provide detailed mechanical parts, e.g., for use in antenna mock-ups, in a short lead time. Nevertheless, one of the main issues associated with it is that the materials suitable for 3D printing are not characterized at radio frequencies (RF). This study analyzes the main RF parameters (dielectric constant, loss tangent, surface roughness) and applies the results to the modeling of the prototype of an electrically small (ESA) antenna for binaural hearing instruments applications. After discussing the specific technology choices and their relevancies, it is shown how the analyzed parameters can be used to obtain good correlation between simulations and measurements.**

***Index Terms*—Rapid prototyping; electrically small antennas (ESA); wireless body-area networks (WBAN); electromagnetic compatibility (EMC); consumer electronics.**

I. Introduction

Rapid prototyping in the electronics industry is of special interest due to the possibility to have access to prototypes at a very early stage, i.e., as soon as the mechanical design is outlined. Rapid prototyping, also known as 3D printing, is emerging today as a technology that enables fast fabrication of devices. The printed devices are typically inexpensive and easy-to-build. The technology has been used, e.g., for antenna prototypes and to manufacture a 60 GHz plastic lens-antenna [1]–[3]. For the antenna designer, this translates into a great potential of building mechanical support for its designs. On the other side, the performance of the evaluation mock-ups is extremely dependent upon the process itself. The ability to identify and separate the critical factors from the non-critical is important in order to be able to model the antennas in an efficient way.

RF and antenna electronics poses serious challenges on 3D printed prototypes. In fact, even though the freedom during the design process is a great advantage for the engineering of the device, the material itself strongly impacts the result. In particular, it is necessary to establish a correlation among the 3D-printed prototype and the final parts that will be used in the mass production. In fact, specific deposition processes for the conductive parts have to be studied. The main issue, nevertheless, is with the electrical properties of the plastics themselves. Some processes may prove to be better than others in this regard, but this still has to be studied. Among the potential issues there are: the inclusion of air bubbles within the plastics that changes the effective dielectric constant from prototype to prototype, or from batch to batch; inherently higher loss tangent as compared to cast plastic; poor or non-existing RF characterization of the materials.

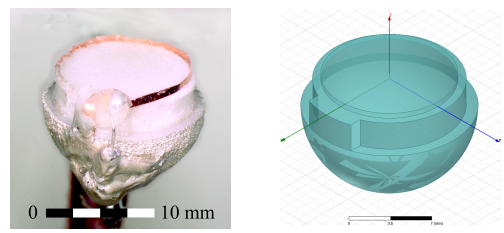

(a) (b)

Fig. 1: Photo of the prototype (a) and rendering of the 3D-printed mechanical support (b), respectively.

Nevertheless, the understanding and correct modeling of such properties would allow the antenna designers to evaluate their prototypes. As an application example, in the hearing instruments (HI) there is a need to wirelessly connect two devices placed at each ear with an ear-to-ear (E2E) link, as this allows for more advanced signal processing [4]. Recently, a few solutions have been proposed by different authors [5]–[8]. The 2.4 GHz ISM band is preferred here due to its world-wide availability and the amount of available communications standards, such as Bluetooth Low Energy (BLE) or ZigBee. In this study, Selective Heat Sintering (SHS) 3D-printed plastics are used as the frame of an antenna for binaural hearing instruments.

The article is organized as follows: Section II describes the antenna design and implementation. In the following section, the main electrical parameters are analyzed. Section IV then presents and discusses the simulation and measurement results. Finally, Section V summarizes the findings.

II. Antenna Design and Implementation

The prototype antenna comprises of an Inverted-F Antenna (IFA) arm, bent on a plane situated above an hemispherical ground plane with a radius of $r = 7.5$ mm. This concept was recently introduced for on-body devices, and it is suitable for the use in binaural hearing instruments due to its good radiation efficiency and polarization characteristic [9], [10]. The electrical size of the antenna at 2.4 GHz is $ka = 0.38$,

where k is the free space propagation constant, and a the radius of the sphere circumscribing the antenna. Thus the antenna can be contained within the Wheeler radiansphere [11] since the electrical length is less than one radian, i.e., it is an electrically small antenna [12].

A picture of the antenna is shown in Fig. 1a. A more substantial description of the antenna is found in [9].

The mechanical support for the antenna, shown in Fig. 1b, is prototyped with additive manufacturing. A SHS 3D printer is used to build the frame. In this technology, moderate heat is selectively applied to a thin layer of a specific thermoplastic powder in order to bind it together and to form a solid structure. The process is repeated after the deposition of a new layer until the desired height is reached.

The hemispherical ground plane is then metalized with conductive paint. The feed structure is electrically connected with conductive glue. If soldering is preferred, since the heat produced during the soldering process can damage the plastic support, it is possible to solder the feed structure on a thin layer of solid copper and afterwards connect or couple it to the ground plane. The IFA arm is made of solid copper with an electrical conductivity of $58 \cdot 10^8$ S/m.

III. Parameter Analysis

A. Surface Roughness

The ability to custom shape the mechanical frame by the 3D printing process on one hand gives multiple advantages, but on the other hand the printing process challenges other aspects of the prototype. E.g., in this case, where a hemispherical ground plane needs to have a good conductivity, different layers of a polycrystalline conductive paint are applied to the antenna support. The porosity of the 3D printed plastics causes it to be partly absorbed into the frame. This results in a complicated profile that is hard to inspect and model. If the roughness of the deposited metal layer by the fabrication method is significant, the recently-developed Huray loss model can be used [13].

In the present work, the results show that an accurate model for the metal surface roughness ρ_{s} is not necessary in order to achieve good agreement between the simulations and measurements.

B. Dielectric Constant

The dielectric constant plays a fundamental role in every simulation model. In fact, parameters like the electrical length of an antenna on a substrate depends significantly on the effective dielectric constant $\varepsilon_{\mathrm{eff}}$ that is mostly determined by the material properties. Unfortunately, such value is not provided by the 3D printer manufacturers: mainly, it falls out of their main scope. Furthermore, in a fast-growing and competitive business as that of 3D printing, it seems to be normal that the manufacturers do not want to disclose specific information about the printing material, as it is part of their competitive advantage. In Table I the relative permittivity values of the mean μ and the standard deviation σ for a set of cast, stereolithography (SLA), and SHS plastics at 2.4 GHz are reported. The results are mostly indicative and were obtained by the use of the cavity perturbation method, where a sample is inserted into a resonant cavity and its properties are inferred from the resulting variation in resonant frequency and bandwidth. Injection molding is a technique traditionally not used in the evaluation of prototypes, as it is the method most often used in the final production. RF-wise, they exhibit higher density and lower losses as compared to the plastics obtainable with 3D printing processes. The SHS process shows the lowest $\varepsilon'_{\mathrm{r}}$, i.e., the largest deviation from the solid plastic properties. The other 3D-printing process analyzed here is a modified SLA that uses a liquid photo-polymer resin that is cured layer-by-layer by an ultraviolet laser to selectively solidify the pattern. The SLA and cast plastics data are here presented in an aggregated form. The higher variance for the first two cases depends on the size of the test population, that is much larger and varies more than in the third case.

TABLE I: Mean and standard deviation, $\mu \pm \sigma$, for the relative permittivity and loss tangent at 2.4 GHz for cast (injection molded), SLA, and SHS plastic

Process	$\varepsilon'_{\mathrm{r}}$	$\tan\delta$
Cast	2.8 ± 0.2	0.006 ± 0.002
SLA	2.53 ± 0.03	0.024 ± 0.005
SHS	2.40 ± 0.01	0.012 ± 0.0006

C. Loss Tangent

Dielectric losses plays a crucial role as well. In fact, it is shown here that this by far is the largest contribution to the overall losses. It is observed that it is possible to obtain good agreement between simulations and measurements when the conductive losses are neglected. The loss tangent $\tan\delta$ was estimated by the use of the cavity perturbation method as well and are shown in Table I.

The loss tangent is a critical parameter since the measured Total Radiated Power (*TRP*) depends nearly entirely on it. The *TRP* performance is a key parameter when the prototype designs are to be evaluated in the early stage. If the loss mechanism in not well understood, the result could be that a decision is made for an over- or underestimated design.

In particular, the SLA process exhibits particularly high losses. This complicates the evaluation scenario for mock-ups. The SHS process shows instead contained losses—about twice that of cast plastics and half of those obtainable by SLA.

IV. Measurement Results and Discussion

The characterization is done in terms of the antenna total radiation efficiency η_{tot}, i.e., a function of two important parameters: the reflection coefficient Γ at the antenna input terminals and the antenna radiation efficiency η_{rad} and is given by

$$\eta_{\mathrm{tot}} = (1 - |\Gamma|^2)\ \eta_{\mathrm{rad}}\ . \tag{1}$$

The total radiation efficiency η_{tot} is obtained by measurement of the total radiated power *TRP* in a radio anechoic chamber.

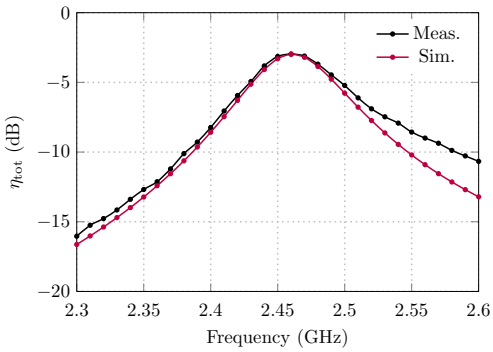

Fig. 2: Measured (black line) and simulated (red line) total radiation efficiency, η_{tot}.

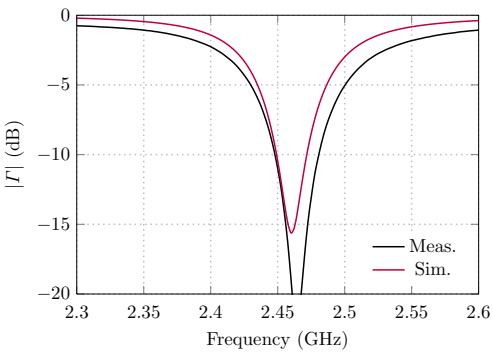

Fig. 3: Measured (black line) and simulated (red line) reflection coefficient at the antenna terminals, $|\Gamma|$.

Since the antenna is well impedance matched, $|\Gamma|^2 \approx 0$ at the center frequency. Hence, the total radiated efficiency is approximately equal to *TRP* normalized with respect to the input power. In order to measure the reflection coefficient Γ at the true antenna terminals, a Vector Network Analyzer (VNA) with a corrected port extension has been used. The simulations are run with a FEM solver (Ansys HFSS®). All simulations and measurements are conducted in free space.

The total radiation efficiency is shown in Fig. 2, whereas the reflection coefficient is reported in Fig. 3. There is an excellent agreement among the simulated (red line) and measured (black line) antenna total efficiency. This is supportive of the fact that the main loss mechanism is not linked to the skin effect on the conductor, but to the dielectric losses in the plastic frame. The efficiency falls in the high range for the purpose of the application in practical HI. The deviation between the curves above the higher band edge is likely due to spurious currents, as the used balun is inherently narrowband. The potential radiation efficiency varies slowly with respect to the frequency.

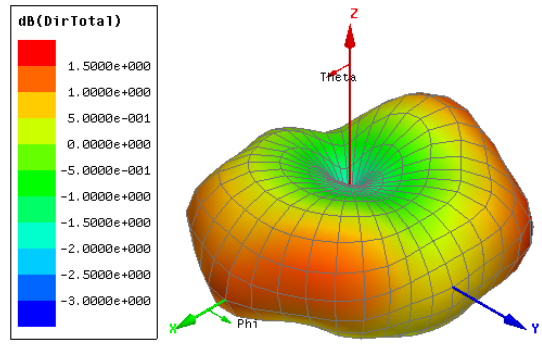

Fig. 4: Simulated directivity (in dB) of the antenna.

The matching provided by the shorting pin of the IFA sets the actual bandwidth. The 3D radiation pattern of the antenna is shown in Fig. 4, where the antenna is oriented as in Fig. 1.

V. Conclusion

The material properties of 3D-printed plastics have been characterized. This allows for efficient and accurate modeling of an antenna for binaural hearing instruments. A SHS printer was used to manufacture the antenna frames. The plastic properties were assessed by the cavity perturbation method. The conductive losses have been analyzed. It was discovered that they had insignificant influence in this application.

An electrically small wearable antenna suitable for E2E communications was implemented and modeled. Excellent agreement between simulations and measurements was obtained. To conclude, it is possible to use rapid prototyping for mock-ups, given that the electrical properties are known.

VI. Acknowledgements

The authors would like to thank Dr. Gianluca Fabio Dorini of Blueprinter A/S for the support and valuable discussions, in addition to sourcing the 3D-printed parts.

References

[1] J. Tribe, W. G. Whittow, R. W. Kay, and J. C. Vardaxoglou, "Additively manufactured heterogeneous substrates for three-dimensional control of local permittivity," *Electronics Letters*, vol. 50, no. 10, pp. 745–746, 2014.

[2] O. S. Kim, "Rapid prototyping of electrically small spherical wire antennas," *IEEE Transactions on Antennas and Propagation*, vol. 62, no. 7, pp. 3839–3842, 2014.

[3] A. Bisognin, D. Titz, F. Ferrero, R. Pilard, C. A. Fernandes, J. R. Costa, C. Corre, P. Calascibetta, J.-M. Riviere, A. Poulain, C. Badard, F. Gianesello, C. Luxey, P. Busson, D. Gloria, and D. Belot, "3D printed plastic 60 GHz lens: Enabling innovative millimeter wave antenna solution and system," *IEEE MTT-S International Microwave Symposium Digest*, 2014.

[4] B. C. Kirkwood, S. A. Hallenbeck, and T. Stender, "How can wireless data exchange in hearing instruments contribute to binaural hearing?" *Hearing Review*, vol. 19, no. 10, pp. 52–55, 2012.

[5] N. Kammersgaard, S. Kvist, J. Thaysen, and K. Jakobsen, "In-the-ear spiral monopole antenna for hearing instruments," *Electronics Letters*, vol. 50, no. 21, pp. 1509–1511, October 2014.

[6] R. Chandra and A. J. Johansson, "A link loss model for the on-body propagation channel for binaural hearing aids," *IEEE Transactions on Antennas and Propagation*, vol. 61, no. 12, pp. 6180–6190, 2013.

[7] L. Huitema, S. Sufyar, C. Delaveaud, and R. D'Errico, "Miniature antenna effect on the ear-to-ear radio channel characteristics," *Proceedings of 6th European Conference on Antennas and Propagation (EuCAP 2012)*, pp. 3402–3406, 2012.

[8] W. H. Yatman, L. K. Larsen, S. H. Kvist, J. Thaysen, and K. B. Jakobsen, "In-the-ear hearing-instrument antenna for ISM-band body-centric ear-to-ear communications," *2012 Loughborough Antennas and Propagation Conference (LAPC)*, 2012.

[9] A. Ruaro, J. Thaysen, and K. B. Jakobsen, "Cavity-backed on-body antenna for custom hearing instrument applications," *accepted to Electronics Letters*, 2015.

[10] S. H. Kvist, S. Özden, J. Thaysen, and K. B. Jakobsen, "Improvement of the ear-to-ear path gain at 2.45 GHz using parasitic antenna element," *6th European Conference on Antennas and Propagation*, vol. 2, pp. 944–947, 2011.

[11] H. Wheeler, "The radiansphere around a small antenna," *Proceedings of the Institute of Radio Engineers*, vol. 47, no. 8, pp. 1325–1331, 1959.

[12] ——, "Fundamental limitations of small antennas," *Proceedings of the Institute of Radio Engineers*, vol. 35, pp. 1479–1484, 1947.

[13] P. G. Huray, O. Oluwafemi, J. Loyer, X. Ye, and E. Bogatin, "Impact of copper surface texture on loss: A model that works," *DesignCon 2010*, vol. 1, pp. 462–483, 2010.

Paper 9

"Battery Coupling Impact on the Antenna Efficiency in a Small Wearable Device"

A. Ruaro, J. Thaysen, and K. B. Jakobsen

[P9] A. Ruaro, J. Thaysen, and K. B. Jakobsen, "Battery coupling impact on the antenna efficiency in a small wearable device", in *Proceedings of the Loughborough Antennas and Propagation Conference (LAPC)*, 2015.

Battery Coupling Impact on the Antenna Efficiency in a Small Wearable Device

Andrea Ruaro*†, Jesper Thaysen*, and Kaj B. Jakobsen†

*GN ReSound A/S, Lautrupbjerg 7, DK-2750 Ballerup, Denmark
†Department of Electrical Engineering, Technical University of Denmark, DK-2800 Lyngby, Denmark

***Abstract*—Wearable electronics is often challenged by the extremely reduced space available to the antenna design. This study assesses the impact that the coupling to a large battery has on a small antenna for wearable devices. The coupling mechanism and its potential risks for the Electromagnetic Compatibility (EMC) performance are discussed in detail. Once the battery is placed within an electronic device, it is seen that one of the main performance parameters, i.e., the antenna radiation efficiency, may drop up to 1.2 dB depending on the battery size.**

***Index Terms*—Electrically small antennas; on-body antennas; wireless body-area networks (WBAN); body-centric communications; electromagnetic compatibility (EMC); electromagnetic interference (EMI); electromagnetic coupling; consumer electronics.**

I. Introduction

Wearable electronics is the enabler of Wireless Body Area Networks (WBAN) on the physical layer. Such devices, for whose communication is an essential function, have to face many challenges specific to the environment that they operate within. In particular, objects that aim at being worn need to be compact, not attract attention, and be lightweight. Due to the compromises necessary during product design in modern electronics the available room for the antenna is severely limited; furthermore, it needs to share its physical space with other electronic parts. These can serve the most diverse functions: some depends on the end use of the product, while other are typical components like sensors, monitors, or buttons. Nevertheless, all have one aspect in common: except for some extremely low-power applications where energy harvesting may suffice, they need to be supplied by a power source, usually a battery. The communication function itself is generally rather power demanding. Most of the times, the larger the battery, the longer the product can maintain its functions. Wearable devices are struggling with some of the challenges of mobiles, but in a much more compact space [1]–[5].

The antenna design for such applications cannot be studied as stand-alone, but needs to be taken into consideration in the context in which it is embedded. When applied to wearable devices, given their dimensions, its implementation often brings the antenna —that must be physically small— to be in close proximity or even share electrical connection with other components of the device, being it the Printed Circuit Board (PCB), a screen, or the battery. As the vast majority of products makes use of harmonized standards (e.g., Bluetooth Low Energy or ZigBee) in the open ISM band at 2.4 GHz, the physical proximity translates as well to electrical proximity. At radio frequencies (RF) this introduces parasitic capacitance, which makes it hard to achieve high isolation among the different parts [1].

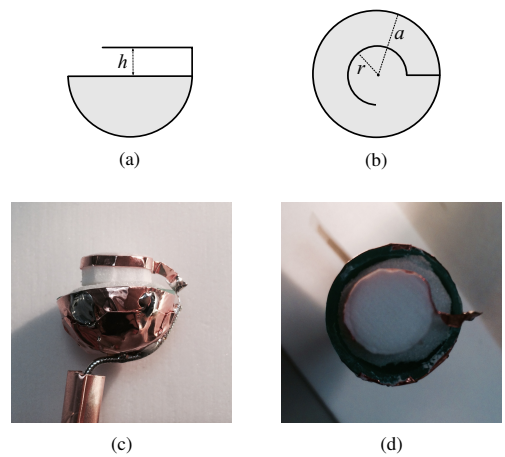

Fig. 1: Diagram of the wearable cavity-backed antenna, (a) side view and (b) top view; and photo of the prototype, (c) side view and (d) top view.

Unwanted, uncontrolled coupling to the battery may be the cause of a long list of Electromagnetic Compatibility (EMC) issues that can severely degrade the antenna radiation performance. For instance, the losses associated to the skin effect due to the currents induced on the battery's conductive surfaces decreases the antenna radiation efficiency. Furthermore, noise from the electronics might couple to the battery and subsequently be re-radiated. These and other issues are described in Section II-A.

A proper decoupling of the battery at RF is therefore of critical importance in order to preserve the antenna radiation characteristic. Furthermore, it is necessary to quantify the magnitude of this phenomenon. The characterization is done in terms of the antenna total efficiency η_{tot}, i.e., a function of two

important parameters: the reflection coefficient at the antenna input terminals, Γ, and the antenna radiation efficiency, η_{rad}. For future standardization, it is of interest to understand what the impact of the commonly available batteries is on the antenna performance in order to develop design guidelines for robust design.

The article is organized as follows: Section II provides the background for the study and describes the coupling mechanism and the issues associated to the battery presence. It also includes the antenna characterization and an overview of the standard battery technology. In Section III the measurement set-up and results are presented and discussed. Finally, Section IV summarizes the findings.

II. Background

A. Coupling Mechanism and Related Issues

The main purpose of the battery is to power the different functions of an electronic device, including wireless communication. Typically, its RF performance is not explicitly characterized by the manufacturers as it is not necessarily in the focus during the design process. Therefore, the EMC scenario for the application needs to be carefully characterized during the development stage. For instance, complications may arise as a battery comprises of two separate parts that need to be electrically separated at DC in order to provide the positive and the negative pole. The gaps in between them introduce a parasitic capacitance. If currents are induced on the conductive parts of the battery, losses can be expected due to skin effect. An equivalent circuit can therefore be sketched as in [6] including resistive losses, stray capacitance, and a self-inductance, as shown in Fig. 2. At RF, the coupling from a nearby antenna is predominantly either capacitive or conductive, the latter in the case a direct path to ground is provided [1]. An RF connection to ground can change the currents' ground return paths: a weaker control on the current flow translates into a weaker control on the design.

Another important issue is that the battery has typically large electrical dimensions as compared to the antenna, and the active antenna element has to share the physical space with other functions [2]. This issue is much more severe in wearable electronics than it is in mobile phones due to their relative dimensions [3], [4]. Given its size, the battery can also act as an unwanted radiator and therefore transmit at out-of-band frequencies, drawing risks to the EMC approval process. This includes as well a series of additional factors, e.g., strong coupling, leading to detuning of the antenna with subsequent increase of the losses due to mismatch, reduction of the overall radiation efficiency, and an increase of the electrical field strength within the device, therefore causing EM noise that can target the device electronics and cause desensitization of the RF chipset. In fact, the electric field is concentrated as a consequence of the reduced overall space available: if the PCB is placed nearby, it is exposed to a higher field concentration that can cause noise to couple from, or couple in, the electronics. The higher field intensity within the frame of the device itself exposes the electronics to additional RF interference that may require implementation of dedicated solutions [7]. Unfortunately, this often translates into higher project cost and longer time-to-market.

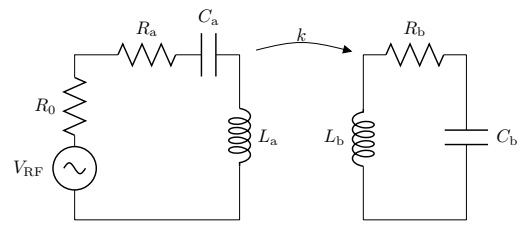

Fig. 2: Equivalent circuit of the coupling mechanism between the antenna (R_{a}, L_{a}, C_{a}) and the battery (R_{b}, L_{b}, C_{b}).

TABLE I: Design parameters for the antenna shown in Fig. 1.

Parameter	Value
a (mm)	20.0
r (mm)	4.8
h (mm)	3.0

Not least, the coupling to the battery may change the field distribution within the device and therefore affect the polarization of the radiated fields. In this case, this parameter —that is of primary importance in some applications [8]— may be compromised. The presence of the battery also reduces the volume available to the antenna, and therefore it increases the Q-factor, i.e., decreases the potential bandwidth of the antenna [5].

B. Antenna Characterization

The antenna used for the test is based on a cavity-backed design. This recently-introduced antenna is suitable for use in on-body devices due to its high radiation efficiency and can be designed to be polarized normal to the user's body when worn [9]. A bent wire, lying on a plane above a thin copper ground plane shaped as a hemisphere, acts as the main radiator. In this case, the radiating element is a $\lambda/4$–monopole, and no matching circuit is implemented. The ground plane shape maximizes the volume available in the device while it reduces the energy radiating directly toward the user body.

A diagram of the antenna is shown in Fig. 1, whereas the design parameters are given in Table I. As the length of the antenna active element has to be equal to $\lambda/4$, and at the same time fit within a shell of diameter a, a bending radius r is calculated from Fig. 1b by means of simple geometry as

$$r = \frac{\lambda/4 - h - a/2}{3\pi/2 - 1}. \tag{1}$$

The mechanical support is provided by a polymethacrylimide (PMI) foam, ROHACELL® 31 HF, with electrical properties of $\varepsilon_{\mathrm{r}} = 1.05$ and $\tan\delta < 0.0002$. The feed is implemented by the use of a semi-rigid coaxial cable, whereas a $\lambda/4$

TABLE II: Common battery information

ID		d	h	type
IEC	alternative	(mm)	(mm)	
SR60	AG1	6.8	2.1	alkaline
SR59	AG2	7.9	2.6	alkaline
SR41	AG3	7.9	3.6	alkaline
SR54	AG10	11.6	3.1	alkaline
SR43	AG12	11.6	4.2	alkaline
SR44	AG13	11.6	5.4	alkaline
PR41	312A	7.9	3.6	zinc-air
PR70	10ZA	5.8	3.6	zinc-air
PR48	13A	7.9	5.4	zinc-air

bazooka balun is soldered onto it in order to prevent spurious radiation.

A more substantial description of the antenna is found in [9].

C. Battery Details

Two different series of pill-shaped batteries are used in this study: alkaline and Zinc-Air. Their type and dimensions are given in Table II. Li-Ion batteries are not included due to their lack of standardization, as they are custom shaped according to each individual application.

During the test, the batteries are centered with respect to the hemispherical ground plane and are placed below the antenna arm at a distance $h = 3$ mm.

III. Measurement Results and Discussion

The reflection coefficient, Γ, has been measured with a Vector Network Analyzer (VNA) at the antenna input terminals. A correction term for the phase delay introduced by the coaxial feed cable is applied. The Total Radiated Power (TRP) is measured in a radio anechoic chamber. The TRP is a function of the antenna radiation efficiency, η_{rad}:

$$TRP = (1 - |\Gamma|^2)\ \eta_{\mathrm{rad}}. \tag{2}$$

In the antenna configuration the active radiator is a monopole arm. It presents at its terminals an impedance that is rather different from 50 Ω due to its reduced dimensions, as shown in Fig. 3. In fact, the potential radiation efficiency of the antenna is rather wideband (i.e., varies slowly with respect to the frequency). The measured TRP is affected by the inherent mismatch. To compute the total radiation efficiency that would be achievable, for instance, with a lumped matching network, for each antenna an ideal matching network that provides a reflection coefficient Γ_0 has been simulated. The magnitude of such network is plotted on the right y-axis in Fig. 4. This is hence accounted for by a matching loss ML correction term given by

$$ML = \frac{1 - |\Gamma_0|^2}{1 - |\Gamma|^2}. \tag{3}$$

The total efficiency therefore takes both terms into account:

$$\eta_{\mathrm{tot}} = (1 - |\Gamma_0|^2)\ \eta_{\mathrm{rad}} = ML \cdot TRP. \tag{4}$$

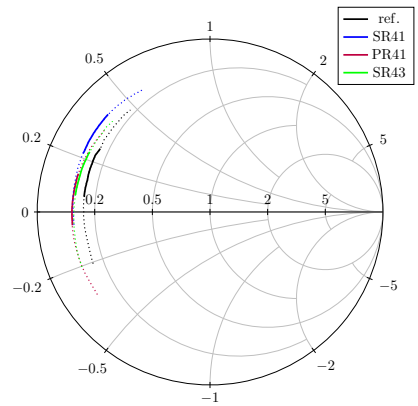

Fig. 3: Measured in-band reflection coefficient, Γ, for selected cases.

Fig. 3 shows the in-band (i.e., from 2.400 to 2.485 GHz) reflection coefficient of the antenna for the selected cases. The magnitude of the change is reasonably small, and therefore has a really limited impact on the overall radiation efficiency. Nevertheless, it is interesting to notice that the introduction of a battery decreases the real part of the impedance even more. This makes it harder to impedance match. Note that the variation of the impedance may be noticed on the radiation efficiency in case of a particularly narrow-band matching network (e.g., used for filtering), i.e., with a high Q-factor, as this would increase the mismatch losses.

Fig. 4 shows the total radiation efficiency for selected cases. It is evident that the introduction of an electrically-large battery into the volume used by the antenna affects its performance due to the causes discussed in Section II-A. A decrease of the radiation efficiency of up to approximately 1.2 dB for larger batteries is observed. This is quite significant given the strict requirements of the applications. No differences were observed for a specific battery type. This supports the fact that the main loss mechanism is linked to the skin effect, i.e., to the resistive losses of the currents induced on the steel can of the batteries. In fact, the conductor loss is caused by the current flow inside the conductor, i.e., to the tangential magnetic field at its surface [10]. At RF, the currents are confined to the outer layer as determined by the skin depth, resulting in increased resistive losses. The magnetic field vector induced on a steel can is shown as obtained from the simulation on the antenna in Fig. 5. Note that the z-distance between the antenna arm and the battery surface is $h = 3$ mm. This is a rather large distance with respect to what may be actually available during a different design process.

The measured difference between the efficiency measured when no battery is present and when a battery is installed is given in Table III. The data are shown at the band edges and at the center of the band. It can be noticed how the

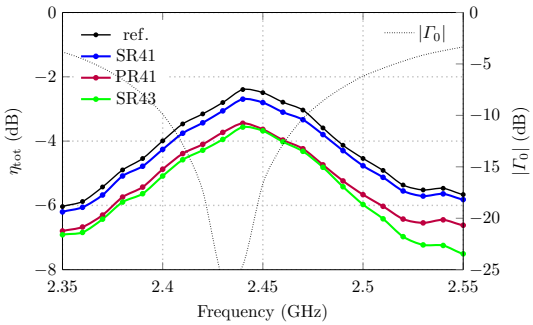

Fig. 4: Total radiation efficiency, η_{tot}, calculated for selected cases as in Eq. 4 from the measured *TRP*. On the right y-axis, the reflection coefficient, Γ_0, of the ideal matching network used for the computation.

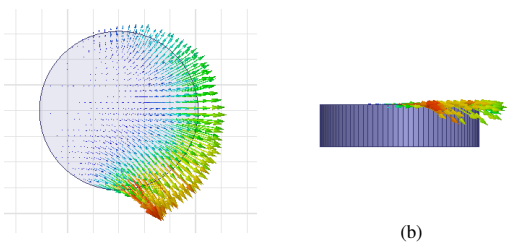

(a) (b)

Fig. 5: Plot of the simulated magnetic field vector, as induced from the antenna on a steel can.

decrease in total radiation efficiency varies across frequencies for the current antenna configuration, ranging from being not critical (e.g., the SR41 case at the band upper edge) to being significant (e.g., the SR43 case at the band upper edge). Therefore, a careful design for any application shall start with a decision about the battery type and positioning, and decisions on the antenna design taken accordingly.

IV. Conclusion

The impact that the coupling to a battery has on a small antenna for wearable devices has been studied in this work.

TABLE III: Decrease in total radiated power ΔTRP due to the presence of a battery

IEC ID	ΔTRP (dB)		
f (GHz)	2.40	2.44	2.48
SR41	−0.27	−0.30	−0.21
PR41	−0.88	−1.05	−1.15
SR43	−1.09	−1.17	−1.22

In particular, it has been discovered that the introduction of the battery decreases the radiation efficiency of the antenna of a significant amount, given the strict requirements that on-body antennas demand for. Drops up to 1.2 dB were measured within the 2.4 GHz ISM band. With regards to the reflection coefficient, the introduction of the battery (in this configuration) decreases the real part of the antenna impedance. The consequences of this are deemed of secondary importance. Furthermore, the coupling mechanism and its potential risks for the Electromagnetic Compatibility (EMC) performance have been discussed in detail. The possible complications that such coupling could create are highlighted.

References

[1] X. Chen, N. Chavannes, G. Ng, Y. Tay, and J. Mosig, "Analysis and design of mobile device antenna–speaker integration for optimum over-the-air performance," *IEEE Antennas and Propagation Magazine*, vol. 57, no. 1, pp. 97–109, Feb 2015.

[2] C.-H. Wu and K.-L. Wong, "Internal shorted planar monopole antenna embedded with a resonant spiral slot for penta-band mobile phone application," *Microwave and Optical Technology Letters*, vol. 50, no. 2, pp. 529–536, 2008.

[3] X. Liang, "The battery effect in mobile antenna design," *Microwave and Optical Technology Letters*, vol. 52, no. 1, pp. 120–122, 2010.

[4] J. Thaysen and K. B. Jakobsen, "Estimation of the optimal location of metallic objects inside a mobile phone," *Microwave Journal*, pp. 196–204, 2005.

[5] A. D. Yaghjian and S. R. Best, "Impedance, bandwidth, and Q of antennas," *IEEE Transactions on Antennas and Propagation*, vol. 53, no. 4, pp. 1298–1324, 2005.

[6] C. Balanis, *Antenna Theory: Analysis and Design*. John Wiley, 2005.

[7] A. Ruaro, J. Thaysen, and K. B. Jakobsen, "Mitigation of Unwanted Forward Narrow-band Radiation from PCBs with a Metamaterial Unit Cell," in *43rd European Microwave Conference (EuMC)*, 2013.

[8] S. H. Kvist, S. Özden, J. Thaysen, and K. B. Jakobsen, "Improvement of the Ear-to-Ear Path Gain At 2.45 GHz Using Parasitic Antenna Element," *6th European Conference on Antennas and Propagation*, vol. 2, pp. 944–947, 2011.

[9] A. Ruaro, J. Thaysen, and K. B. Jakobsen, "Cavity-backed on-body antenna for custom hearing instrument applications," *submitted to Electronics Letters*, 2015.

[10] D. Pozar, *Microwave Engineering*. John Wiley & Sons, 2005.

Paper 10

"Wearable Shell Antenna for 2.4 GHz Hearing Instruments"

A. Ruaro, J. Thaysen, and K. B. Jakobsen

[P10] A. Ruaro, J. Thaysen, and K. B. Jakobsen, "Wearable shell antenna for 2.4 GHz hearing instruments", *IEEE Transactions on Antennas and Propagation*, 2015, submitted for publication.

Wearable Shell Antenna for 2.4 GHz Hearing Instruments

Andrea Ruaro, Jesper Thaysen, and Kaj B. Jakobsen

***Abstract*—A novel concept for an electrically-small on-body antenna targeted for 2.4 GHz ISM band custom in-the-ear (ITE) hearing instrument (HI) applications is introduced. The antenna is based upon a cavity-backed design in order to take advantage of the maximum volume available in the ear while providing isolation from the user's body, and it occupies only 40% of the volume of the sphere with radius a = 12 mm. The antenna is implemented on a realistic 3D-printed lossy substrate and exhibits high efficiency of 70% and 22%, and a 6-dB impedance bandwidth of 108 MHz and 149 MHz, when the antenna is measured in free space and ITE, respectively. A measurement campaign conducted in free space and on a specific anthropomorphic mannequin (SAM) head with ears shows that the radiation pattern is optimal for HI applications. Furthermore, the antenna is primarily polarized normal to the surface of the head to ensure the best on-body path gain. This is substantiated by the study of the ear-to-ear (E2E) path gain, which is measured and compared to analytic and numerical results.**

***Index Terms*—Cavity-backed antennas (CBA); conformal antennas; electrically small antennas (ESA); medical devices; on-body communications; wearable antennas; wireless body-area networks (WBAN).**

I. Introduction

WEARABLE antennas for body-area network (BAN) implementation are quickly emerging as one of the major antenna application fields, drawing interest from both academia and industry. Among the different on-body communication applications, the hearing instrument (HI) industry is particularly interested in developing connectivity solutions. In fact, radio connectivity between HIs allows for advanced binaural signal processing when the important ear-to-ear (E2E) link is ensured [1]. Furthermore, the HIs may be connected to a plethora of accessories, that can be either body-worn or placed in the user's proximity, and hence to the internet as part of the so-called internet of things (IoT).

The 2.4 GHz industrial, scientific, and medical (ISM) band is preferred for this purpose due to the presence of many harmonized standards for low-power communications (such as BLE or ZigBee), its worldwide availability for industrial use, and the trade-off between power consumption and range that can be achieved. In order to ensure the connectivity of HIs, a thorough understanding of the on-body propagation mechanism of electromagnetic waves around a user's head and body is required. In particular, it is challenging but of key importance to ensure a stable E2E link: this has been the focus of much research work in recent times [2]–[7]. As the analysis of this link through software FEM solvers is extremely time consuming due to the electrical size and complexity of the models involved, an accurate channel model has been proposed [2]. This model is based on a thorough investigation of the way that creeping waves propagate around the head, and it allows to compute the E2E path gain PG in a fast and accurate manner. The proposed model is then used to compute the optimal radiation pattern for E2E communication by the use of a genetic algorithm. Additionally, it is used to estimate the variance of the E2E link, which arises due to the difference in shape among human heads, by the use of a Monte Carlo analysis [2].

The E2E link is particularly demanding in terms of requirements on the wearable antenna design and performance. In fact, in order to achieve a good on-body performance, the antenna needs to exhibit optimal radiation efficiency, bandwidth, polarization, and radiation pattern [3], while the volume available for the design is extremely reduced—as most times space comes at a premium in wearable devices. Furthermore, mass production and industrial design needs demand the antenna to be as well low-profile, lightweight, and inexpensive to manufacture. In particular, the antenna polarization characteristic is a performance parameter of utmost importance [4], but the overall constrains are many more. In fact, the efficiency may be seriously jeopardized by the proximity of the antenna to the human head, as the body tissues have very high losses around 2.4 GHz due to the high water content [8]. This may critically impact the overall performance given the magnitude of the drop in efficiency and the fact that the HI radios operate in ultra-low-power regime. Another issue threatening the antenna efficiency is the little volume available for the design, as this necessarily brings the antenna in close physical (hence, electrical as well) proximity of other parts of the device, with a strong likelihood of coupling to them [9]. A large bandwidth is as well hard to achieve for an electrically small antenna (ESA), due to its fundamental limits [10]. In this application, the bandwidth shall cover at least the whole 2.4 GHz ISM band, but a larger bandwidth would help to compensate for the detuning of the antenna caused by the body, which varies across users [11].

Most of the works that study on-body propagation makes use of simple antenna structures, in particular monopoles or general antenna designs that do not take into account the actual application needs. Some work has been done in recent time to propose antennas that are suitable for implementation in HIs, including among others a spiral monopole [12], a

Andrea Ruaro and Jesper Thaysen are with GN ReSound A/S, Lautrupbjerg 7, DK-2750 Ballerup, Denmark (e-mail: aruaro@gnresound.com, jtahysen@gnresound.com).

Kaj B. Jakobsen is with the Department of Electrical Engineering, Electromagnetic Systems, Technical University of Denmark, Ørsteds Plads, Building 348, DK-2800 Kgs. Lyngby, Denmark (e-mail: kbj@elektro.dtu.dk).

TABLE I
OVERVIEW OF THE KEY PERFORMANCE METRICS FOR HI ANTENNAS

reference	type	BW (MHz)	η_{tot} (%)	$\mathbf{P}$	a (mm)	ε_{r}	$\tan\delta$	PG_{E2E} (dB)
[12]	BTE	80*	—	$\parallel$	5	1.1	0.000	−80
[13]	ITE	76	5.3	$\perp$	10*	6.0	0.002	−73*
[14]	ITE	10*	0.3*	$\perp$*	7*	3.6	0.003	−89*
[15]	BTE	240*	—	$\perp$	11	1.1	0.000	−50
This work	ITE	149	22	$\perp$	12	2.4	0.012	−63

'*' denotes different observation conditions.

slot loop [13], a wire-patch [14], and a balanced PIFA [15]. Nevertheless, none fully characterizes the antenna performance measuring all the performance metrics mentioned above. In fact, a measure of the reflection coefficient alone is not sufficient, as most of the energy accepted by the antenna is dissipated in the head in form of heat [8]. Instead, the E2E path gain measure is an excellent performance metric, but on the other side it is a system-level measurement affected by multiple factors and typically needs to be substantiated by numerical results. An overview of the key performance metrics for the mentioned designs is reported in Table I. From left to right are shown in the table, respectively: the reference source; the position of the antenna on the head, either behind-the-ear (BTE) or in-the-ear (ITE); the bandwidth BW; the total radiation efficiency η_{tot}; the main direction of the polarization vector $\mathbf{P}$ (either tangential $\parallel$ or normal $\perp$ to the head surface) [16]; the radius a of the minimum sphere encompassing the antenna; the dielectric constant ε_{r} and the loss tangent $\tan\delta$ of the support substrate; and the maximum E2E path gain PG_{E2E}. All data applies to the 2.4 GHz ISM band. Where available, measured data are preferred to simulation results. The data marked with an asterisk (*) are either strongly dependent on the specific context, or approximated, or non-uniquely defined, or selected among multiple options available in the source: the reader is encouraged to look up the original reference in order to understand the reported data.

On the other hand, cavity-backed antennas were studied in details well in the past, but they were not used for on-body applications until very recent times [16]–[19]. One of the main advantages of cavity-backed antenna is that they are not significantly affected by the electronic environment around them, as the cavity provides some sort of electromagnetic shielding. Based upon this principle only, even without an optimal current distribution, an interesting on-body performance can be achieved by a large, early-stage prototype, where the cavity does not actively contribute to the radiation mechanism [19]. This work introduces and fully characterizes a novel wearable shell antenna based on an open cavity-backed design. The very shell of a customized in-the-ear (ITE) HI is used as part of the antenna. The design is detailed and a prototype is fully characterized by means of numerical simulations and measurements. Selective Heat Synthering (SHS) 3D-printed plastics are used for the antenna frame. This process has been recently characterized at radio frequencies and it allows for an accurate numerical modeling [20].

The article is organized as follows. Section II describes the theoretical principles, the design and the implementation of the antenna. Section III presents the measurement set-up and results, and discusses them. Section IV analyzes the performance of the antenna along the critical ear-to-ear path. Finally, Section V summarizes the findings.

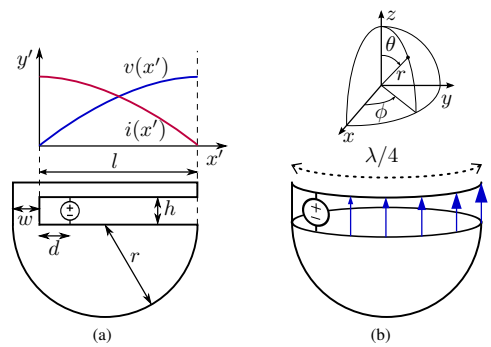

Fig. 1. Antenna diagram, (a) profile and (b) 3D view.

II. THEORY AND DESIGN

A novel antenna is proposed based on the geometry shown in Fig. 1 in order to address all the complex requirements that the hearing instrument application demands.

Simple equations of the radiated fields are not trivial to derive from the field distribution in the aperture. While closed-form expressions exist both for a slot antenna, which can be analyzed as the dual of the equivalent flat wire antenna [16], or an antenna fully backed by a cavity [17], factors like the conformal shape, the small ground plane and the position of the antenna at its edge, and the curvature of the antenna arm, makes it unrealistic to derive a simple equation-based model. The principle of how the antenna function is hence best understood via analogy to an Inverted F-Antenna (IFA) or an open-ended $\lambda/4$ slot antenna. If the antenna cavity is loaded with a dielectric material, the wavelength is $\lambda = \lambda_0/\sqrt{\varepsilon_{\text{eff}}}$, where λ_0 is the free space wavelength and ε_{eff} the effective dielectric constant at the substrate–air interface. For the purpose of symmetry, consider a hemispherical ground plane of radius r, with the edge laying in the xy-plane. A wire is electrically connected to the ground plane, bent at a height h, and curved to follow the edge of the hemispherical cavity. The distance between the wire and the edge of the ground plane is kept constant at h. The length of the wire is such that the current

has an antisymmetric distribution around the slot of length l, i.e.,

$$l = \frac{\lambda/2 + h}{2} \approx \lambda/4 \text{ for } h \ll \lambda \ . \quad (1)$$

Please note, this is somewhat independent on the radius r of the hemispherical ground plane, when it respects the condition:

$$2\pi r > l \Leftrightarrow r > \lambda/8\pi \ . \quad (2)$$

The antenna radiation mechanism is best understood when the voltage distribution shown in Fig. 1 is considered. In fact, the current at the end of the antenna arm is null. As the distance from the open end to the short-circuiting pin is $\lambda/4$, the current distribution is sinusoidal and reaches a maximum at the pin. The pin width w is chosen large enough in order not to present a significant self-inductance at the operating frequency. The voltage distribution is $90°$ out of phase with respect to the current: therefore, at the short-circuiting pin the voltage across the slot is null, while it reaches a maximum at the open end. The feed structure excites a voltage across the slot. Even though the impedance across the slot varies in a complex way as discussed above [17], it is very high at the open end and very low at the short-circuiting pin. As the impedance increases monotonically, there exists a $50\ \Omega$ matched point that can be found at a distance d from the short-circuiting pin.

As the antenna is meant to fit in the ear, it has to be modeled according to each user's unique ear canal shape. The design process starts from this specific physical form, and therefore it is necessary to abandon the symmetry of the cavity and replace it with a more realistic model as shown in Fig. 2. In the hearing industry, this is typically done by taking an impression of the external auditory canal and of the concha. Here, the software model shown in Fig. 2 is generated from a given ear shape. The antenna is then built on a 3D-printed plastic substrate to fit the custom shape of the designed specific anthropomorphic mannequin (SAM) ear. The support is realized with a Selective Heat Synthering (SHS) process that exhibits a dielectric constant $\varepsilon_r = 2.4$ and a loss tangent $\tan\delta = 0.0012$ at the frequency of interest [20]. The conductive layers, i.e., the ground plane and the antenna arm, are implemented with solid copper. A picture of the right ear prototype is shown in Fig. 2d. The final design parameters are based on the idealized model described above, and are optimized for the ITE performance in a commercial FEM software simulator. The shape of the custom cavity, as given by the ear model, and h were assumed as given working assumptions, whereas l, w, and d were subsequently optimized with respect to center frequency and bandwidth. Since the realistic cavity shape is not hemispherical as in the idealized model, the parameter r is undefined. In order to discuss the antenna physical and electrical size, it is therefore replaced by the radius a of the minimum sphere encompassing the antenna. The design parameters of the antenna are listed in Table II.

In order to maximize the on-body performance, the antenna has to have high radiation efficiency, be polarized normally to the head surface, have a omnidirectional radiation pattern in the plane tangential to the head, and have a sufficient impedance bandwidth [3]. The efficiency requirement is determined by the fact that the power that is absorbed into the head is, in fact, dissipated in form of heat. Without even addressing the regulatory issues, this translates in practical applications in a drastic drop of the antenna efficiency. A good way to minimize this is to effectively use the antenna part farther away from the head to concentrate the **E**-field. An antenna with a small ground plane has higher losses given the spatial distribution of its reactive near field [3]. The ground plane helps in shielding the head from the radiation, in a similar way to the widespread use of the ground plane in PIFAs in order to reduce the backward radiation [8].

The radiation pattern on the plane tangential to the body surface and the polarization characteristics are of key importance in order to properly excite strong surface waves. In fact, the signal level in the line-of-sight (LOS) scenario is enough for most applications once sufficient radiation efficiency is guaranteed, as there is no body shadowing—on the contrary, the body can partly act as a reflector [21]. Instead, when the receiving antenna is placed in non-line-of-sight (NLOS), these parameters acquire critical importance. The polarization is the

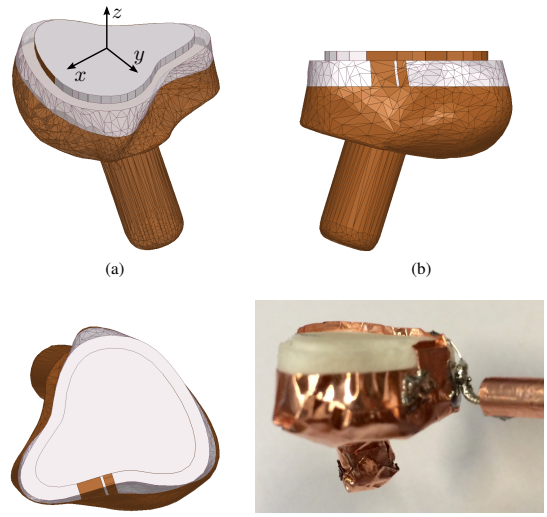

Fig. 2. Custom shell antenna: (a–c) CAD model, different views; (d) picture of the prototype.

TABLE II
ANTENNA DESIGN PARAMETERS

l	23.5 mm
h	2.7 mm
w	2.6 mm
d	0.5 mm
a	12.0 mm
ka	0.62 rad
ε_r	2.4
$\tan\delta$	0.012

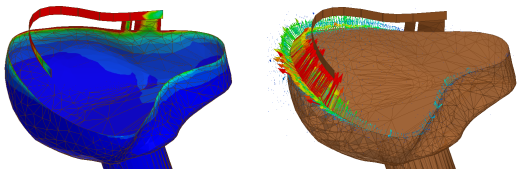

(a) (b)

Fig. 3. Plot of the antenna with overlaid (a) current magnitude and (b) **E**-field vector.

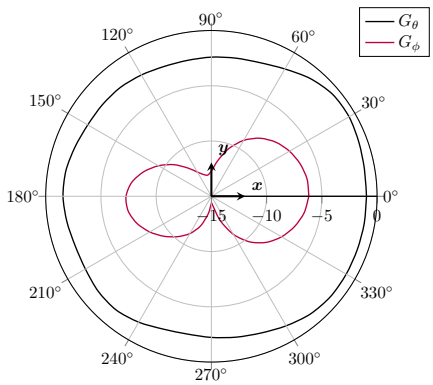

Fig. 4. Simulated free space antenna gain in the xy-plane, divided into its polarization components G_θ and G_ϕ.

dual of that of a flat wire; hence it is normal to the head surface. This can also be seen by the distribution of the surface current and of the **E**-field shown in Fig. 3. This is optimal in order to excite a strong surface wave along the body [3]. Please note that the polarization is weakly dependent on the radius of curvature of the antenna arm, and therefore is suitable to conform to different ear morphologies.

The radiation pattern is optimal as well, as can be seen by the plot of the θ- and ϕ-component of the simulated free-space antenna gain plotted in Fig. 4. There is a strong dominance (above 6 dB in every direction) of the θ-component over the ϕ-component on the plane tangential to the head surface.

The bandwidth is optimized by the shape of the ground plane. In fact, an IFA is strongly dependent on the ground plane dimensions, which impacts the polarization of its main radiation mode and has to be electrically large. A decrease in the size of the ground plane beyond a certain limit may seriously jeopardize the performance of an IFA [22]. Therefore, it is important to maximize the ground plane size within the volume at disposal. In this case, the hemispherical shape maximizes the available volume within half of the Wheeler's sphere [23] and uses most of the available surface to implement the ground plane. This lowers the Q factor, i.e., it results in a larger bandwidth [10]. The electrical size ka of the antenna is promptly obtained in the simplified geometry, as the radius a of the sphere circumscribing the antenna is

$$a = \sqrt{r^2 + h^2} \approx r \text{ for } h \ll r \ , \tag{3}$$

whereas for the custom shaped antenna the actual value reads $ka = 0.62$ rad at a frequency $f = 2.45$ GHz. In the idealized case, the antenna uses only approximately 50% of the volume of the circumscribing sphere. The custom shaped antenna uses only 40% of the volume of the sphere of radius $a = 12$ mm. Even though the shell antenna shape is conformal to the ear canal, the currents are confined in the area close to the aperture: therefore, the design is less dependent upon the specific shape of a given ear. The idealized model works well in this sense. Another advantage of this architecture is that it is relatively insensitive to the presence of conductive parts within the shell itself, e.g., a battery or a device's electronics [24]. Electromagnetic coupling to other parts of a device, which include among others loudspeaker's coils, can easily worsen the radiation efficiency of the antenna [9].

III. Measurement Results

A. Set-up

The designed antenna prototype was measured in free space (FS), as a reference, and on-body. The on-body measurements are conducted with the antenna placed in-the-ear (ITE) of a SAM head. The shape of the antenna shell is designed to fit such ear design. The ear material is a CTIA-compliant [25] homogeneous silicone-carbon dielectric with average electrical properties $\varepsilon_{\mathrm{r,ear}} = 28$ and $\sigma_{\mathrm{ear}} = 1.15$ S/m at $f = 2.45$ GHz (data measured by the supplier). The low-loss outer shell of the SAM head itself is 2 mm thick. This was not included in the simulation set-up, where a homogeneous head model is used. This was shown to possibly influence the measured results [5], but as shown below, it is not deemed critical here. The fill liquid in the phantom is targeted to $f = 2.4$ GHz and is CTIA compliant [25], with nominal electrical properties $\varepsilon_{\mathrm{r,SAM}} = 44$ and $\sigma_{\mathrm{SAM}} = 2$ S/m. The slight difference in the electrical properties between the CTIA-compliant liquid and the FEM model is neglectable [2].

The antenna is fed with a coaxial cable. The VNA measurements used the port extension correction in order to measure the S-parameters, including the phase, at the true antenna port. To prevent the RF cable to radiate as a consequence of the spurious currents running on it, as the antenna has an unbalanced architecture, a $\lambda/4$ bazooka balun is soldered onto the cable itself as visible in Fig. 2d. The cable hence does not represent an extension of the small ground plane, and the presence of spurious currents running on the coaxial cable outer shell was not observed during the analysis at the VNA. In any case, during the measurements the cable lays onto a plane tangential to the head, so that it is mostly ϕ-polarized (as it is a wire radiator) to ensure an even lesser impact on the measurement results.

The measurement campaign was conducted in a ETS-Lindgren commercial anechoic chamber. The measurement coordinate system is shown in Fig. 2 for the antenna in free space, and in Fig. 5 for the antenna placed in-the-ear of the SAM head. In free space, the antenna arm lays on the xy-plane, with the positive z-axis oriented toward the opposite side of the conductive shell. The origin of the coordinate system is centered with respect to the center of the

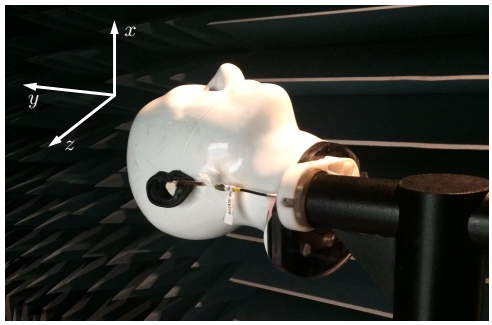

Fig. 5. Picture of the measurement set-up, with the antenna coordinate system.

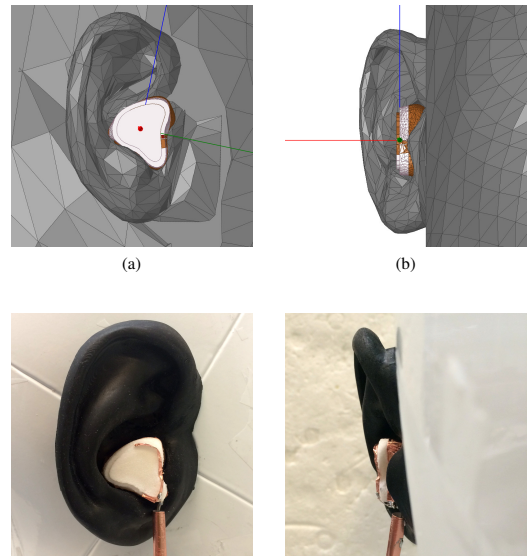

Fig. 6. Detail of the antenna fitted into the human ear. Position in the FEM solver, (a) front view and (b) side view, and position in the SAM ear, (c) front view and (d) side view.

circle circumscribing the antenna on the xy-plane. The same orientation is kept when the antenna is measured on the head, i.e., the xy-plane is the plane tangential to the head surface and the z-axis is normal to the head surface. The origin of the coordinate system is centered at the right ear of the SAM. The measurements are reported for the right ear prototype.

In the anechoic chamber, ferrite beads were mounted on the feed cable to the antenna connector in order to suppress spurious radiation. The distance of the antenna from the mast that controls the rotation is 250 mm, i.e., approximately $2\lambda_0$ at the operating frequency $f = 2.4$ GHz. Some reflections and shadowing in the radiation patterns are due the presence of the mast. The measured fields are directly sampled in the Fraunhofer region, and are therefore considered a good approximation of the true far field. The chamber is calibrated. The data are processed by the chamber manufacturer's proprietary software EMQuest$^{\text{TM}}$ EMQ-100. The total efficiency is computed based on the estimation of the total radiated power (TRP) of the antenna.

For the in-the-ear measurements, the antenna is fitted within the SAM ear as shown in Fig. III-A and Fig. III-A, whereas the ear canal works as a guide. The semielastic dielectric material, which the ears are made of, introduces a small air gap in between the antenna and the ear surface. The antenna feed sits in between the tragus and the anti-tragus, with the end of the antenna arm fitted in the concha. In this area, which is where the antenna is farther from the tissue, is where the concentration of the $\mathbf{E}$-field is highest. The feed cable descends in front of the lobule toward the neck. It can be seen from Fig. III-A and Fig. III-A how the profile of the antenna is low on the ear, as it is meant to be operated in the case of hearing instruments.

B. Results

There is a rather strong general agreement between measurements and simulations. From the voltage standing wave ratio $VSWR$ shown in Fig. 7, it is seen how the impedance match improves and becomes significantly more wideband when the antenna is worn. This is expected, as it means that a significant amount of the power is not being reflected back to the VNA: hence it might be radiated, or dissipated in form of losses in the antenna dielectric fill or in the human tissues.The antenna is de-tuned when worn, as a consequence of the capacitive loading provided by the proximity of the human body. This is seen in both simulations and measurements. The impedance match was chosen to optimize the antenna performance in the ITE case. The bandwidth performance of the antenna is rather remarkable given its overall dimensions. The bandwidth is defined here as the impedance bandwidth for $|S_{11}| \leq -6$ dB, or equivalently $VSWR \leq 3$. In fact, as bandwidth is not uniquely defined, this is a commonly accepted value given the application, in addition to the fact that the antenna is severely space-constrained [26]. The measured free space impedance bandwidth is $BW_{6\text{dB,FS}} = 108$ MHz $\sim 4.4\%$, and the on-body bandwidth is $BW_{6\text{dB,ITE}} = 149$ MHz $\sim 6.1\%$. The performance is comparable to that of an IFA on a large solid ground plane in the 2.4 GHz band [27], whereas the arm height here is 2.7 mm only.

The simulated and measured radiation efficiency is plotted if Fig. 8. The free space efficiency is excellent, especially recalling the high dielectric loss tangent of the mechanical support. It peaks at -1.54 dB $\sim 70\%$ for a frequency $f = 2.51$ GHz. The on-body efficiency peaks at -6.50 dB $\sim 22\%$ at $f = 2.45$ GHz, while in the whole 2.4 GHz ISM band it is above -7.54 dB. The efficiency drop is around 5 dB only. This is deemed rather reasonable for a wearable antenna inserted deep in the body, and is due to the shielding effect provided by the conformal ground plane among other factors.

With regards to specific absorption rate (SAR) assessment, it shall be noted that due to the very low power of the related applications, no SAR study is required by regulatory bodies [28]. In fact, wearable devices are required to operate

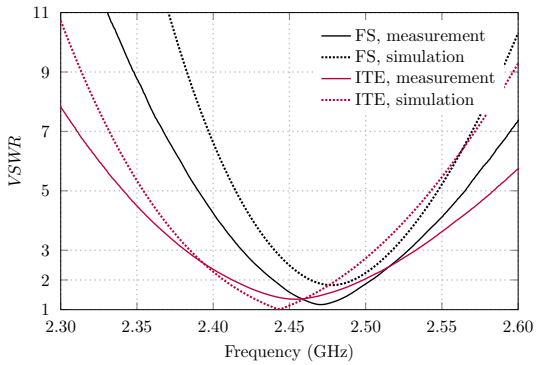

Fig. 7. The reflection coefficient expressed as $VSWR$ at the antenna interface in free space (FS) and on the SAM head in-the-ear (ITE).

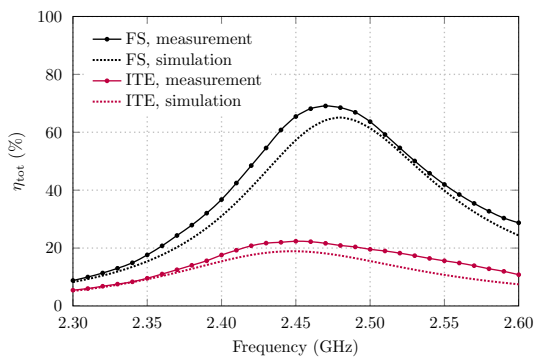

Fig. 8. The antenna radiation efficiency in free space (FS) and on the SAM head in-the-ear (ITE).

as low-power applications in order to preserve the battery's lifetime. Therefore, the value of the radiated fields is typically several orders of magnitude smaller than that of, e.g., handset applications. In the case of an example HI, the peak output power of the radio chip may be in the few-mW range; furthermore, the radio operates with low duty cycle, i.e., below 5% [29]. Therefore, as SAR is a system metric, the average output power $P_{\text{out}} = 0.05$ mW $= -13$ dBm is used in this case for SAR calculations [30], [31]. The devices are well below the SAR test exclusion threshold due to the extremely low power operation [28]. The SAR values are shown for different average output power P_{out} values in Table III. The values are numerically simulated with Ansys HFSS™ and are estimated conservatively. While the first reported case is representative of actual HI operation, the second ($P_{\text{out}} = 1$ mW $= 0$ dBm) refers to potential continuous-wave operation, or operation with a duty cycle of 100%, equivalently. The third case listed in Table III is the limit case for BTLE operation (within the ETSI range) [29] with 100% duty cycle, and still falls below the regulatory limits. Fig. 9 shows the SAR spatial distribution normalized to each case peak value, respectively.

The radiation patterns for the antenna are shown in Fig. 10

TABLE III
SAR VALUES

P_{out} (dBm)	$\text{SAR}_{1\text{g}}$ (W/Kg)	$\text{SAR}_{10\text{g}}$ (W/Kg)
-13	$7 \cdot 10^{-3}$	$2 \cdot 10^{-4}$
0	0.13	0.04
10	1.30	0.35

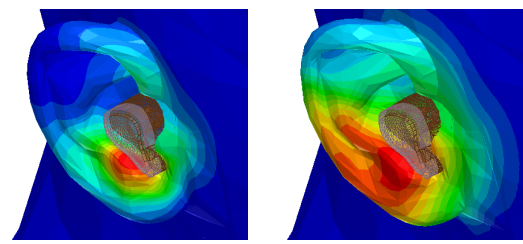

(a) (b)

Fig. 9. Spatial distribution of the SAR value, averaged over (a) 1 g (FCC) and (b) 10 g (IEC) of tissue, normalized to the relative peak value listed in Table III, respectively.

and Fig. 11 for the free space and on-body case, respectively. The respective coordinate systems are those shown in Fig. 2 and Fig. 5, respectively, with the open side of the cavity oriented toward positive z-axis and the xy-plane being tangential to the head. In free space, the antenna is nearly omnidirectional in the xy-plane as desired. The tilt on the yz-cut is mostly dependent on the inclination of the **E**-field. In fact, in Fig. II it can be seen that the **E**-field is not purely z-aligned since the antenna arm is inset slightly inwards. In the measurements, the back lobe is affected by the presence of the chamber mast. This introduces some reflections and generates an angle-dependent ripple. The omnidirectionality in the xy-plane is maintained when the antenna is fitted into the SAM ear. In the xz- and yz-cuts the head shadowing effect can be observed. Overall, there is a reasonably good agreement between the simulated and measured radiation patterns that are shown in Fig. 10 and Fig. 11, especially taking into account the the differences between the software model and the actual prototype, and the repeatability of the antenna placement in the real life scenario.

The performance of the antenna is summarized in Table IV for the FS and ITE cases.

IV. EAR-TO-EAR LINK

In order to achieve binaural hearing benefits as mentioned in the introduction, each hearing instrument need to be able to

TABLE IV
MEASURED ANTENNA PERFORMANCE

	FS	ITE	
$BW_{6\text{dB}}$	108	149	MHz
η_{peak}	-1.54	-6.50	dB
$PG_{\text{E2E,avg}}$	—	-66.1	dB

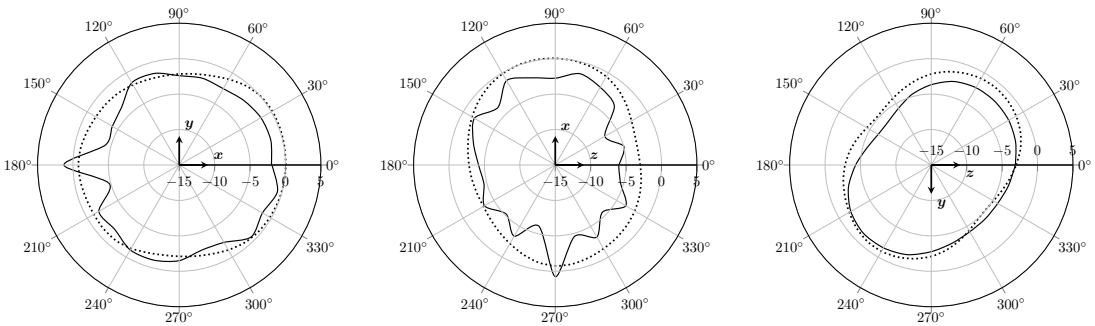

Fig. 10. Free space radiation patterns (antenna total gain) in dBi, measured (solid line) and simulated (dotted line). Left: xy-plane ($\theta = 90°$). Center: E-plane ($\phi = 0°$). Right: H-plane ($\phi = 90°$). The patterns are plotted at $f = 2.45$ GHz.

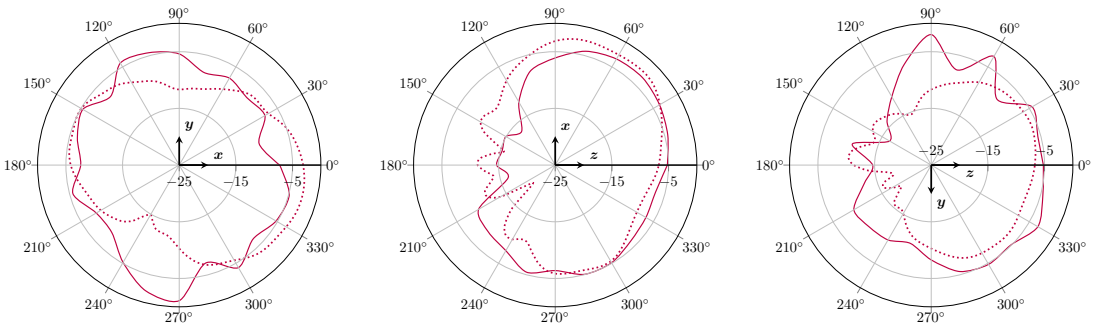

Fig. 11. In-the-ear radiation patterns (antenna total gain) in dBi, measured (solid line) and simulated (dotted line). Left: xy-plane ($\theta = 90°$). Center: E-plane ($\phi = 0°$). Right: H-plane ($\phi = 90°$). The patterns are plotted at $f = 2.45$ GHz.

communicate with another one that is placed at the opposite side of the head [1]. In this sense, the Ear-to-Ear (E2E) connectivity is the key parameter that has to be ensured by the antenna design. This is dependent upon the antenna radiation properties, such as efficiency and polarization, and on the path loss along the surface of the head. The overall loss is high since most of the electromagnetic energy is radiated directly into the space along the LOS directions, whereas the NLOS propagation around the head has to rely on creeping waves.

As anticipated in the introduction, Kvist *et al.* [2] recently proposed a method to calculate the E2E path gain PG using creeping waves along a number of elliptical paths around the head. This approach draws a series of elliptical paths with different semi-major axes to reproduce the shape of the head, where the convergence of the path gain is obtained for a sufficiently high number of paths. The radiation pattern of the antenna is then taken into account as a weight function in order to provide the excitation along these paths, each one representing a separate creeping wave that propagates around the head.

This result is compared to numerical simulation results obtained by a commercial FEM solver. Also in this case, the convergence of the simulation is reached to ensure a reasonable uncertainty on the very low path gain level. PMLs layer are places around the truncated human body model to absorb incident radiation and to avoid a non-physical contribution from the propagation of electromagnetic waves along these boundaries.

For the E2E path gain measurements, the same SAM head that was detailed in Section III was used with the set-up shown in Fig. 12. A VNA was used to record the path gain $|S_{21}|$. The measurements were conducted in a shielded chamber with EM absorbers. The cables were routed as far as possible from each other to avoid coupling in between them. Both the VNA and the operator were shielded as much as possible by absorbers. Signal averaging was used to minimize the impact of the reflections from the operator.

The measured E2E path gain agrees well with the analytic and numerical calculations, and with previous studies reported by multiple authors [2], [3], [5]–[7], [12]–[15]. The results are shown in Fig. 13. It can be seen that the strong θ-component excited by the antenna assists in ensuring a good E2E path gain, with a simulated maximum of $PG_{\mathrm{sim}} = -54.4$ dB at a frequency $f = 2.44$ GHz. The calculated model falls close, with an absolute difference from the simulated value of only $\Delta PG = PG_{\mathrm{sim}} - PG_{\mathrm{calc}} = 0.05\%$ at a frequency $f = 2.44$ GHz. The deviation of the model from the simulated result increases with frequency as the propagation paths become electrically longer. This suggests a possible influence of the undefined antenna phase center. In fact, given its configuration,

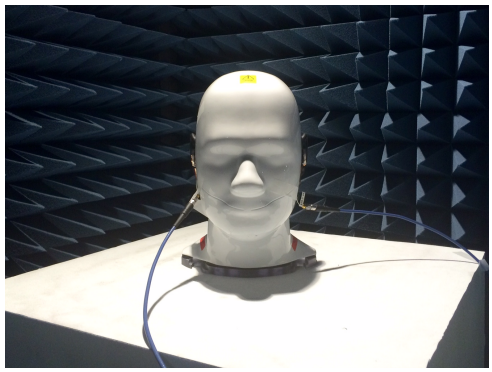

Fig. 12. Picture of the set-up for the measurement of the E2E path gain.

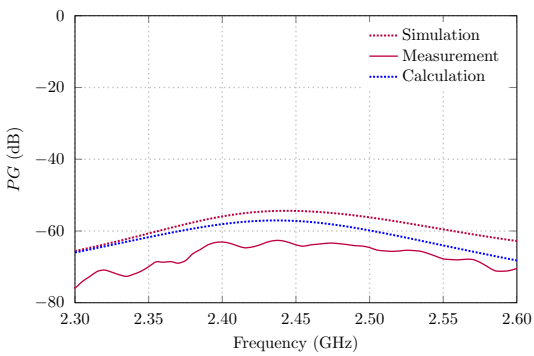

Fig. 13. Plot of the E2E Path Gain (PG), with results from FEM simulation, measurements on SAM head, and calculation based on the analytic model [2].

when placed on-body the antenna does not possess a clearly identifiable phase center. The difference in the electrical length of the propagation paths may also be the cause for the lower E2E path gain that was measured, as the antenna was placed on the SAM slightly below the position that was used for the simulation, as can be seen in Fig. 6.

V. Conclusion

A novel wearable shell antenna was introduced in this work. The application as an on-body hearing instrument antenna was studied. In particular, the novel concept makes use of a ground plane conformal to a user's ear canal to maximize the available volume and reduce the losses caused by the human body, while it ensures high radiation efficiency and a strong polarization component normal to the head surface. The operating principle of the antenna was analyzed by means of analogies to the well-known radiating mechanism of IFAs and slot antennas. The antenna has been fully characterized with the study of the reflection coefficient and matching, radiation efficiency, simulated currents and fields, and radiation pattern, both in free space and when worn in-the-ear (ITE). Furthermore, the critical parameter E2E path gain was studied and compared to a deterministic model that showed a convergence among computation, FEM simulation, and measurements.

References

[1] B. C. Kirkwood, S. A. Hallenbeck, and T. Stender, "How can wireless data exchange in hearing instruments contribute to binaural hearing?" *Hearing Review*, vol. 19, no. 10, pp. 52–55, 2012.

[2] S. Kvist, J. Thaysen, and K. Jakobsen, "Ear-to-ear on-body channel model for hearing aid applications," *IEEE Trans. Antennas Propag.*, vol. 63, no. 1, pp. 344–352, Jan. 2015.

[3] P. S. Hall *et al.*, "Antennas and propagation for on-body communication systems," *IEEE Antennas Propag. Mag.*, vol. 49, no. 3, pp. 41–58, 2007.

[4] N. P. I. Kammersgaard, S. H. Kvist, S. Özden, J. Thaysen, and K. B. Jakobsen, "Body-worn antennas for body-centric wireless communications," in *Loughborough Antennas Propag. Conf. (LAPC)*, 2014.

[5] R. Chandra and A. J. Johansson, "A link loss model for the on-body propagation channel for binaural hearing aids," *IEEE Trans. Antennas Propag.*, vol. 61, no. 12, pp. 6180–6190, 2013.

[6] S. H. Kvist, S. Özden, J. Thaysen, and K. B. Jakobsen, "Improvement of the ear-to-ear path gain at 2.45 GHz using parasitic antenna element," in *Proc. of 6th European Conf. Antennas Propag. (EuCAP)*, vol. 2, 2011, pp. 944–947.

[7] A. Vasylchenko, C. Hennemann, and R. Dubrovka, "Characterization of the ear-to-ear propagation channel using microstrip dipole antennas," in *Proc. 8th Int. Conf. Antenna Theory Techn. (ICATT)*, 2011, pp. 202–204.

[8] M. Jensen and Y. Rahmat-Samii, "EM interaction of handset antennas and a human in personal communications," *Proc. IEEE*, vol. 83, no. 1, pp. 7–17, 1995.

[9] X. Chen, N. Chavannes, G. Ng, Y. Tay, and J. Mosig, "Analysis and design of mobile device antenna–speaker integration for optimum over-the-air performance," *IEEE Antennas Propag. Mag.*, vol. 57, no. 1, pp. 97–109, Feb 2015.

[10] A. D. Yaghjian and S. R. Best, "Impedance, bandwidth, and Q of antennas," *IEEE Trans. Antennas Propag.*, vol. 53, no. 4, pp. 1298–1324, 2005.

[11] S. Pehrson, S. H. Kvist, K. B. Jakobsen, and J. Thaysen, "Morphological investigation of the differences on the ear-to-ear path gain and the packet loss at 2.45 GHz," *34th Annu. Antenna Meas. Techn. Assoc. Symp. (AMTA)*, pp. 43–48, 2012.

[12] N. Kammersgaard, S. Kvist, J. Thaysen, and K. Jakobsen, "In-the-ear spiral monopole antenna for hearing instruments," *Electronics Letters*, vol. 50, no. 21, pp. 1509–1511, October 2014.

[13] W. H. Yatman, L. K. Larsen, S. H. Kvist, J. Thaysen, and K. B. Jakobsen, "In-the-ear hearing-instrument antenna for ISM-band body-centric ear-to-ear communications," in *Loughborough Antennas Propag. Conf. (LAPC)*, 2012.

[14] L. Huitema, S. Sufyar, C. Delaveaud, and R. D'Errico, "Miniature antenna effect on the ear-to-ear radio channel characteristics," in *Proc. of 6th European Conf. Antennas Propag. (EuCAP)*, 2012, pp. 3402–3406.

[15] S. H. Kvist, K. B. Jakobsen, and J. Thaysen, "Design and measurement of a 2.45 GHz on-body antenna optimized for hearing instrument applications," in *34th Annu. Antenna Meas. Techn. Assoc. Symp. (AMTA)*, 2012, pp. 33–37.

[16] C. Balanis, *Antenna theory: analysis and design*, 3rd ed. John Wiley, 2005.

[17] C. R. Cockrell, "The input admittance of the rectangular cavity-backed slot antenna," *IEEE Trans. Antennas Propag.*, vol. 24, no. 3, pp. 288–294, 1976.

[18] N. Haga, M. Takahashi, K. Saito, and K. Ito, "A cavity-backed slot antenna for on-body BAN devices," in *Proc. IEEE Int. Workshop Antenna Technol. (IWAT)*, 2008, pp. 510–513.

[19] A. Ruaro, J. Thaysen, and K. B. Jakobsen, "Cavity-backed on-body antenna for custom hearing instrument applications," *Electronics Letters*, 2015.

[20] ——, "Rapid prototyping analysis and modeling of a small antenna for binaural hearing aids," in *Int. Symp. Antennas Propag. (ISAP)*, 2015.

[21] N. P. I. Kammersgaard, S. H. Kvist, J. Thaysen, and K. B. Jakobsen, "Pinna model for hearing instrument applications," in *Loughborough Antennas Propag. Conf. (LAPC)*, 2014, pp. 141–143.

[22] M. C. Huynh and W. Stutzman, "Ground plane effects on planar inverted-F antenna (PIFA) performance," *IEE Proc. Microw. Antennas Propag.*, vol. 150, no. 4, pp. 209–213, 2003.

[23] H. Wheeler, "The radiansphere around a small antenna," *Proc. IRE*, vol. 47, no. 8, pp. 1325–1331, 1959.

[24] A. Ruaro, J. Thaysen, and K. B. Jakobsen, "Battery coupling impact on the antenna efficiency in a small wearable device," in *Loughborough Antennas Propag. Conf. (LAPC)*, 2015.
[25] CTIA Certification, "Test plan for wireless device over-the-air performance," v3.3.2, September 2014.
[26] Y. Rahmat-Samii, J. Guterman, A. A. Moreira, and C. Peixeiro, "Integrated antennas for wireless personal communications," in *Modern Antenna Handbook*, C. A. Balanis, Ed. John Wiley & Sons, Inc., 2007, pp. 1077–1142.
[27] D. Liu and B. Gaucher, "The inverted-F antenna height effects on bandwidth," in *Proc. IEEE Antennas Propag. Symp.*, vol. 2, 2005, pp. 367–370.
[28] Federal Communications Commission, "447498 D01 general RF exposure guidance," version 6, October 2015.
[29] Bluetooth SIG Regulatory Committee, "Bluetooth low energy regulatory aspects," version 10, April 2011.
[30] International Electrotechnical Commission, "Human exposure to radio frequency fields from hand-held and body-mounted wireless communication devices - Human models, instrumentation, and procedures," IEC 62209-2:2010, part 2, March 2010.
[31] IEEE International Committee on Electromagnetic Safety, "IEEE recommended practice for measurements and computations of radio frequency electromagnetic fields with respect to human exposure to such fields, 100 kHz-300 GHz," IEEE Std C95.3-2002 (R2008), December 2002.

Andrea Ruaro was born in Venezia, Italy, in 1988. He received the B.Sc. degree in Information Engineering from the University of Padova in 2010, and the M.Sc. degree in Electrical Engineering from the Technical University of Denmark in 2012. He is currently working toward the Ph.D. degree at the Technical University of Denmark. Since 2012 he has been affiliated with GN ReSound A/S, a leading hearing instrument manufacturer.

His research interests include electromagnetic interaction and coupling, EMC, and on-body antennas and propagation.

Jesper Thaysen received the B.Sc., M.Sc., and Ph.D. degrees in electrical engineering from the Technical University of Denmark in 1998, 2000 and 2005, respectively. Since 2008 he has been employed at GN ReSound A/S, a Danish hearing instrument manufacturer, where he currently acts as the Director of the Radio Systems group in R&D.

His research interests include small antennas and on-body antennas and propagation. Dr. Thaysen has overseen more than 40 B.Sc. and M.Sc. students, as well as 3 Ph.D. students, as the company representative in university-industry cooperative projects.

Kaj B. Jakobsen received the B.Sc.EE and the M.Sc.EE degree from the Technical University of Denmark, Kgs. Lyngby, in 1985 and 1986, respectively, the Ph.D. degree in Electrical Engineering from University of Dayton, Dayton, OH, in 1989, and the HD in Organization and Management, Copenhagen Business School, Copenhagen in 2000. From 1986-1989 he was a Fulbright Scholar at the Department of Electrical Engineering, University of Dayton, OH. Since 1990 he has been with the Department of Electrical Engineering, Technical University of Denmark, Kgs. Lyngby, where he is Associate Professor.

His research interests are in body-centric wireless network, wireless body area network, and body sensor network. He received in 1989 the NCR Stakeholder Award, Ohio, USA, and was appointed Teacher-of-the-Year at the Technical University of Denmark in 1994.

Paper 11

"Head-Centric Body-Channel Propagation Paths Characterization"

A. Ruaro, J. Thaysen, and K. B. Jakobsen

[P11] A. Ruaro, J. Thaysen, and K. B. Jakobsen, "Head-centric body-channel propagation paths characterization", in *Proceedings of the European Conference on Antennas and Propagation (EuCAP)*, 2015.

Head-Centric Body-Channel Propagation Paths Characterization

Andrea Ruaro*†, Jesper Thaysen*, and Kaj B. Jakobsen†

*GN ReSound A/S, Lautrupbjerg 7, DK-2750 Ballerup, Denmark
†Department of Electrical Engineering, Technical University of Denmark, DK-2800 Lyngby, Denmark

***Abstract*—Wearable devices are experiencing a strong momentum. This leads to an ever increasing demand to ensure a stable link between the different nodes or sensor placed around the human body. In this sense, Body-Coupled Communication (BCC) has a high potential to support the development of Wireless Body-Area Networks (WBAN). This work characterizes, by mean of experiments, the intra-body propagation channels when a pair of differential electrodes is applied on a human head. This is necessary in order to investigate opportunities and drawbacks for a multitude of applications, e.g., binaural hearing instruments, as little has been done so far. Furthermore, a comparison to the typically investigated intra-body links is presented.**

***Index Terms*—Body-coupled communications (BCC); intra-body communications (IBC); wireless body-area networks (WBAN); medical devices; electromagnetic compatibility (EMC).**

I. Introduction

Wireless Body-Area Networks (WBAN) drew the scientific community's attention in the last decade, and are going to be one of the major trends in the industry in the coming years. The on-body sensors may gather data, e.g., for health monitoring purposes or display them to the user, e.g., audio and video. Examples are shown in Fig 1. In this scenario, an interconnected network of sensors is either able to communicate with each other, or via a hub that hosts the main computing function. Of specific interest is the Ear-to-Ear (E2E) link, as it enables real-time data exchange between two hearing instruments. This would directly benefit hearing impaired people, whom use such devices [1].

Typically, the on-body sensors are linked through the use of radio frequency (RF) solutions, where the 2.4 GHz ISM band is often preferred thanks to the presence of harmonized standards such as Bluetooth Low Energy (BTLE) or ZigBee. Nevertheless, such solution is somewhat demanding for the system, in particular due to the quite large transmit power (necessary to ensure the off-body link) and to the relatively high on-body propagation losses: e.g., the mean path gain value for an infinitesimal dipole perpendicular to the surface of the head is $|S_{21}| = -61.1$ dB [2]. Another challenge is represented by the susceptibility to interference, both coming from the device electronics [3] and from the more and more significant crowding of the 2.4 GHz band [4]. In contrast, Body-Coupled Communications (BCC), also known as Intra-Body Communications (IBC), use the human body to transmit the signal, where the radiated energy is mostly confined within it. This leads to small-size and low-power devices. It serves security and privacy purposes, too [5].

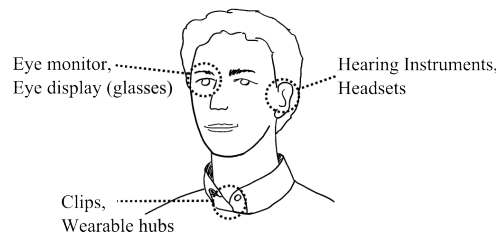

Fig. 1: Examples of on-body sensors and devices that require different interface positions on the head.

Some studies investigated the path losses among nodes placed on the user torso, mostly chest, but also on the arms [6]. It can be easily expected that the propagation of electromagnetic waves in such channels is different from that around the head, due to the different thickness of the flesh and the dominant presence of the brain that invalidate, e.g., the arm models [7], [8]. Therefore there is the need to characterize this link to enable new applications.

In fact, the focus has lately been on devices that interact in the environment around the head of a user or link the head to other devices. This comes natural, as most sensory functions are pivoted around the eyes, ears, mouth, and nose. The ears, in particular, may host hearing instruments with communication capabilities. Furthermore, the ears constitute an accessible interface for sensors to monitor valuable health parameters, like heart rate or blood oxygen rate.

Among the main approaches to couple the signal to the body channel are the galvanic or transmission-line and the capacitive coupled approach. Even though the second may be considered more representative of wearable devices that aim to be as little invasive as possible for the user, as the electrodes can be in delicate contact or in close proximity to the user body in order for the system to operate, the first is preferred in this work. The reason behind this choice is the fact that the system is more stable and independent from the outer environment or movements of the user, and presents a well-defined ground return path [9]–[11].

The article is organized as follows: in Section II the test set-

up and its validation are described. The next section provides reference measurements for different paths on the user body, as well as measurements focused, in contrast, on the head-centric paths. It also discusses the results. Finally, Section IV summarizes the findings.

II. Measurement Set-up and Validation

A. Set-up

Different measurement systems are proposed and discussed in the literature, and a discrepancy in the optimum frequency range for transmission is noticed [6]–[11]. This analysis considers the whole range spanning from 1 MHz to 25 MHz. At frequencies higher than 60 MHz, the human body starts to have a size comparable to a significant fraction of the wavelength and thus can act as an antenna and bias the measurements. The measurements can be extended to cover the frequency range between 25 MHz and 60 MHz if possible unwanted resonances are controlled.

The measurement set-up is shown in Fig. 2. A Vector Network Analyzer (VNA) is connected to a pair of transmit (TX) electrodes at one port and to a pair of receive (RX) electrodes at another, hereafter Port-1 and Port-2, respectively. A pair of wideband baluns are introduces to decouple the VNA cables. The conducted return path is interrupted thanks to the high isolation between the two ports as from the instrument design, i.e., the leaked power is smaller than -65 dB in the frequency range targeted here as reported in the device manual [12]. The use of a single instrument for both transmission and reception avoids uncontrolled conducted coupling, e.g., between the power supplies, as in the case of a set-up that uses different instruments for TX and RX. It must be noted that a weak control over the actual grounding technique might create artifacts in the measurements. In particular, a direct conducted coupling path may increase the received power as measured at the receiver or hide the signal due to an increased noise floor. There still is, of course, a radiated coupling return path. The results are compensated for the system inherent losses, i.e., the calibration of the instrumentation is based upon the unknown-through technique so to account for the transmission losses. This is allowed from the reciprocity $S_{21} = S_{12}$ of the electrode system [13].

The electrodes are made from thin flexible copper. Their shape is squared, with overall dimensions of 25 mm $\times$ 25 mm. A smaller electrode size has a negative impact on the path gain, whereas a larger one complicates the electrodes placement and brings limited or no benefit. This choice also eases the comparison with existing literature [11]. The losses and the conductivity of copper lead to results very close to those obtained using different conductors. The distance between the two electrodes is fixed here at $d_{\text{electrodes}} = 20$ mm, and its parametrization falls out of the scope of this work. The electrodes are directly applied to the user skin through a thin layer of conductive adhesive.

The characterization of the intra-body channel is assessed through the insertion or path gain, i.e., the inverse of the insertion or path loss. The path gain is defined as

$$PG = -IL = 20 \log |S_{21}|$$

and is hereafter equivalently referred to as $|S_{21}|$ (dB). The VNA allows for direct measurement of the S-parameters of the target channel, as

$$S_{21} = \left. \frac{b_2}{a_1} \right|_{a_2=0} ,$$

where a_1 is the amplitude and phase of the wave incident on Port-1, and b_2 is the amplitude and phase of the wave propagating away from Port-2, under the condition that no power is incident on Port-2.

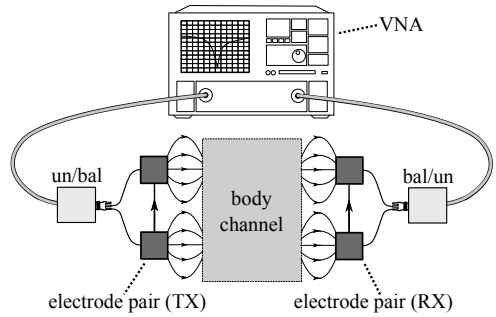

Fig. 2: Measurement set-up.

B. BCC on the user body

The measurements are carried out on multiple subjects of both genders and are here presented in average. The subjects were sitting and held a natural still position. The measurements cover a span of different days in order to account for climate (e.g., pressure, temperature, humidity, ...) and body (e.g., sweat) conditions. The measurement accuracy uncertainty is comparable to that of other studies reported in literature, i.e., within a few decibel. The measurements were carried out in a large room with ordinary furniture and electromagnetic environment, in order to reproduce the actual conditions under which an user would operate the system. A digital Butterworth filter is applied to the data in order to reduce the visual disturbance caused by high frequency noise.

The electrodes are first applied to the test subjects' left arm to validate the system. In Fig. 3 is shown the path gain for two different distances of the electrode pairs. The first distance, represented by the colored line, is chosen to be 100 mm in order to ease the comparison with the results already present in the literature. The second, as read by the black line, is selected to be 130 mm so that it directly compares to the E2E link, as further discussed in Section III.

In both cases it can be seen that the path gain increases with the frequency. This makes higher frequencies a preferred candidate for further investigations. The difference between the two curves changes slightly across the whole frequency

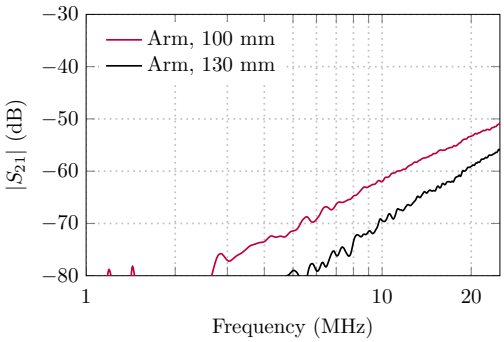

Fig. 3: Insertion gain for the electrode pairs placed on the arm at a distance of 100 mm (red line) and 130 mm (black line), respectively.

range, whereas the lower values measured on the 130 mm channel are related, as logical, to the higher losses along the physically longer path. Anyway, along the whole frequency spectrum the performance is still acceptable, even though these results fall in the low end – especially if compared to the on-body path gain at higher frequencies (e.g., 2.4 GHz).

III. Measurements of Head-centric BCC

In a study conducted on 25 test subject, it was found that the shortest path between the ears along the body surface is on the back of the head. This measures on average $l_{\text{back}} = 217$ mm with a standard deviation of $\sigma = 20$ mm for the tested population [14]. The paths that are analyzed are those on the back of the head, over the head, and in front of it. Nevertheless, as the body is transparent to radiation at the frequencies studied here, the head width with mean $w_{\text{head}} = 141$ mm and standard deviation $\sigma = 8$ mm is used here for comparison. This study makes use of an electrode-to-electrode distance of 130 mm as it is a good representation of the actual tested population, and therefore falls reasonably close to the mean value. It is considered the shortest distance as the one that carries most of the energy.

The electrode pairs are placed on the two opposite sides of the head. The TX electrode is placed close to the ear, in the case of the right ear with the upper left corner aligned to the upper end of the tragus and the left side of the electrode along the lobule, as shown in Fig. 4. The RX electrode is placed 20 mm directly below the TX electrode, conformal to the head surface. The position is mirrored on the opposite side of the head.

Fig. 5 shows a comparison of the path gain of two different channels: the E2E path, and that for the case in which the electrode pairs are placed on a user arm at a distance of 130 mm. The latter is hereafter referred to as the along-the-arm channel, and the separation distance between the electrode pairs omitted. It is evident that both curves follow a

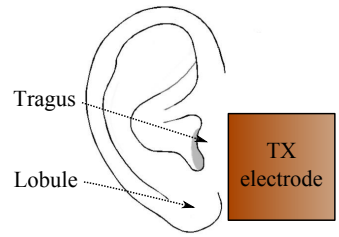

Fig. 4: Anatomy of the outer ear, with TX electrode placement.

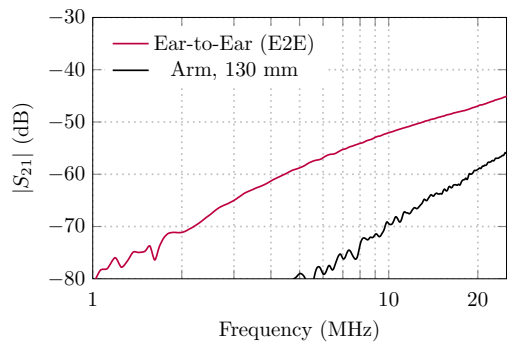

Fig. 5: Insertion gain for the electrode pairs placed at a distance of 130 mm on the head (red line) and on a user arm (black line), respectively.

similar trend, constantly increasing in the double-log scale. In particular, the path gain of the along-the-arm channel peaks at the limit frequency $f = 25$ MHz, where it has a value of $|S_{21}| = -56$ dB, while along the E2E path it reaches a maximum value of $|S_{21}| = -45$ dB.

Fig. 6 shows the ratio between the two curves discussed above (solid line), with a trend-line (dashed line) overlapped to it. This quantity is defined here as the ratio of the E2E path gain to the along-the-arm path gain: i.e.,

$$\Delta PG = \frac{|S_{21,\text{E2E}}|}{|S_{21,\text{arm,13cm}}|} \quad .$$

This measure is of high interest as it allows to visualize the discrepancy between the two trends. In fact, even though both curves follow the same tendency and the path gain reaches an optimum at similar frequencies, it is interesting to notice how their difference decreases at the higher frequencies. Please note, the large variation in the range of $f = [1, 3]$ MHz is due to the proximity of the measured absolute values to the VNA's noise floor.

The difference in path gain is most remarkable in the frequency range of $f = [3, 8]$ MHz, where it reaches a value of above 20 dB. This highlights a difference in the intra-body propagation channel through the head as opposed to that on the arm. It also means that the E2E channel cannot be modeled

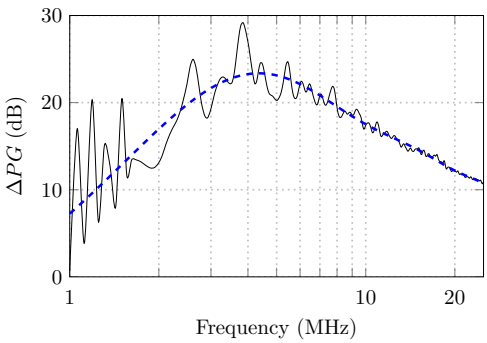

Fig. 6: Ratio (in dB) of the path gains, i.e., the ratio of the ear-to-ear path gain to that of the equivalent distance on the arm.

with the same parameters used for the arm, and therefore invalidates the models presented so far in the literature when applied to this particular path.

The discrepancy may find a first explanation in the different anatomy of the head as compared to other parts of the body. In fact, the arm is often modeled as a layered structure of muscle, with a thin layer of fat and an air interface directly above it. It shall be considered that, on the contrary, below the skin in the head there is the cranium and the brain. It is known that the latter has different constitutional parameters as compared to muscles. The value of the permittivity is, among others, also a function of the frequency, hence a possible root cause of the deviation in the behavior of the two channels. Furthermore, another interesting aspect is the absence of a direct air interface along the whole length of the channel as in the case of the arm. As the electrodes couple to the body channel in a galvanic way, it is considered unlikely that a contingent direct coupling between the electrodes happens through the electrically shorter path around the head.

IV. Conclusion

The E2E propagation channel has been characterized by experiments. The set-up used an electrode system that was galvanic coupled to the user's body. The body-coupled channel is characterized for a given system as having a path loss reaching an optimum in proximity of the maximum measured frequency $f = 25$ MHz, where the insertion gain is measured to $|S_{21}| = -45$ dB. This falls in the high end of the studies in the sector. Even more interesting is to notice how the E2E link compares to along-the-arm link when the electrode pairs are separated by the same spacing. The E2E link shows higher path gain with the difference decreasing at higher frequencies, while the ratio of the two reaches a peak of 23 dB around a frequency of $f = 4$ MHz. This poses new questions for modeling it as compared to arms. The use of BCC to ensure the E2E link appears therefore to be promising and deserves to be further examined, with the characterization ranging from passive (measurement instrumentation) to active devices.

References

[1] B. C. Kirkwood, S. A. Hallenbeck, and T. Stender, "How Can Wireless Data Exchange in Hearing Instruments Contribute to Binaural Hearing?" *Hearing Review*, vol. 19, no. 10, pp. 52–55, 2012.

[2] S. Kvist, J. Thaysen, and K. Jakobsen, "Ear-to-Ear On-Body Channel Model for Hearing Aid Applications," *IEEE Transactions on Antennas and Propagation*, vol. 63, no. 1, pp. 344–352, Jan. 2015.

[3] A. Ruaro, J. Thaysen, and K. B. Jakobsen, "Mitigation of Unwanted Forward Narrow-band Radiation from PCBs with a Metamaterial Unit Cell," in *43rd European Microwave Conference (EuMC)*, 2013.

[4] P. Popovski, H. Yomo, and R. Prasad, "Dynamic Adaptive Frequency Hopping for Mutually Interfering Wireless Personal Area Networks," *IEEE Transactions on Mobile Computing*, vol. 5, no. 8, pp. 991–1003, 2006.

[5] M. Fujikawa and M. Nishigaki, "A Study of Prevention for Social Engineering Attacks using Real/Fake Organization's Uniforms: Application of Radio and Intra-Body Communication Technologies," *Proceedings of the 6th International Conference on Availability, Reliability and Security (ARES 2011)*, pp. 597–602, 2011.

[6] T. C. W. Schenk, N. S. Mazloum, L. Tan, and P. Rutten, "Experimental Characterization of the Body-Coupled Communications Channel," *IEEE International Symposium on Wireless Communication Systems (ISWCS 2008)*, pp. 737–742, 2008.

[7] N. Haga and K. Ito, "Equivalent Circuit of Intra-Body Communication Channels Based on a Lossy Conductor Model," *IEEE Antennas and Propagation Society International Symposium (Digest)*, pp. 672–675, 2012.

[8] K. Fujii, M. Takahashi, and K. Ito, "Electric Field Distributions of Wearable Devices Using the Human Body as a Transmission Thannel," *IEEE Transactions on Antennas and Propagation*, vol. 55, no. 7, pp. 2080–2087, 2007.

[9] K. Partridge, B. Dahlquist, A. Veiseh, A. Cain, A. Foreman, J. Goldberg, and G. Borriello, "Empirical Measurements of Intrabody Communication Performance under Varied Physical Configurations," *UIST (User Interface Software and Technology): Proceedings of the ACM Symposium*, pp. 183–190, 2001.

[10] H. Baldus, S. Corroy, A. Fazzi, K. Klabunde, and T. Schenk, "Human-Centric Connectivity Enabled by Body-Coupled Communications," *IEEE Communications Magazine*, vol. 47, no. 6, pp. 172–178, 2009.

[11] M. Amparo Callejon, D. Naranjo-Hernandez, J. Reina-Tosina, and L. M. Roa, "A Comprehensive Study into Intrabody Communication Measurements," *IEEE Transactions on Instrumentation and Measurement*, vol. 62, no. 9, pp. 2446–2455, 2013.

[12] *E5071C ENA Network Analyzer Data Sheet*, Agilent Technologies, Inc., February 2014.

[13] A. Ferrero and U. Pisani, "Two-Port Network Analyzer Calibration Using an Unknown 'Thru'," *IEEE Microwave and Guided Wave Letters*, vol. 2, no. 12, pp. 505–507, 1992.

[14] S. Pehrson, S. H. Kvist, J. Thaysen, and K. B. Jakobsen, "Morphological Investigation of the Differences on the Ear-to-Ear Path Gain and the Packet Loss at 2.45 GHz," *34th Annual Antenna Measurement Techniques Association Symposium (AMTA)*, pp. 43–48, 2012.

Paper 12

"Combined antenna—electrode system for custom hearing instrument applications"

A. Ruaro, J. Thaysen, and K. B. Jakobsen

[P12] A. Ruaro, J. Thaysen, and K. B. Jakobsen, "Combined antenna—electrode system for custom hearing instrument applications", *IET Electronics Letters*, 2016, submitted for publication.

Combined antenna-electrode system for custom hearing instrument applications

A. Ruaro, J. Thaysen, and K. B. Jakobsen

A novel dual-frequency antenna-electrode system is introduced. A prototype is fabricated and its dual-mode operation is characterized by measurements on a SAM head. From the measurements is seen that the antenna can achieve satisfactory radiation efficiency $\eta_{\mathrm{tot}} = 13.6\%$ and a nearly omnidirectional radiation pattern at a primary (high) frequency $f_1 = 2.4$ GHz when worn in the ear. At the same time, the prototype can be operated at a secondary (low) frequency $f_2 = 30$ MHz as an electrode pair and transmit a signal on the ear-to-ear channel with a path gain as high as $PG_{\mathrm{E2E}} = -59.5$ dB. The path gain is sufficient in order to establish an ear-to-ear link resilient both to environment interference and Rayleigh fading.

Introduction: Wearable electronic devices lead the research and development of antennas toward miniaturization. The ever-growing attention to wireless body-area networks (WBAN) and the internet of things (IoT) exerts a strong influence in many technology sectors, among which are healthcare applications. In the vast majority of cases, the new devices need to operate in the 2.4 GHz industrial-scientific-medical (ISM) band in order to be compatible with major radio standards, e.g., Wi-Fi, BTLE, or Zigbee. The radio system's form factor, integration, and compactness are of paramount importance for the design of wearable electronics. In particular, devices such as hearing instruments (HI) have to support both off-body connectivity with accessories and an on-body ear-to-ear (E2E) data link necessary to enable advanced signal processing [1]. The head environment was found to have some potential advantages propagation-wise in the megahertz frequency range [2]. The advantages of radio operation at these frequencies include resilience of the link to environment interference and Rayleigh fading. Furthermore, at low frequencies the system requires less power [3], and thus poses less stress on the battery lifetime of such devices. A dual-mode system was recently researched [4], but it did not included the aspects of integration in a device—that constitutes the real research limit. This is the first time ever that this novel concept, which takes into account the integration needs, is fit within an actual design.

Design and implementation: The model of the antenna-electrode system is shown in Fig. 1 in a generalized form. The system can operate at a primary frequency $f_1 = 2.4$ GHz in the gigahertz range, and at a secondary frequency $f_2 = 30$ MHz in the megahertz range. The antenna that operates at f_1 consists of a curled flat wire that follows the profile of an electrically-small ground plane at a height $h = 2.7$ mm. The ground plane is shaped to fit the concha and outer ear canal of an user's ear. The antenna has a length $\ell \approx \lambda/4$ at its operating frequency, and is impedance matched by the use of a short pin of width w placed at a distance d from the feed. The dimensions are shown in Table 1. The radiation mechanism is similar to that of an inverted-F antenna (IFA): the **E**-field reaches the maximum value in the proximity of the open end as shown on the left in Fig. 1. The design is able to ensure high efficiency when used on body, due to the shielding effect of the ground plane [5]. The radiation pattern is suitable for on-body use, since the zero in the z-direction is compensated by the reflections introduced by the human head.

The electrode system is conformal to the shape of the concha and outer ear canal of the model ear. The single electrode of each pair has an area A in the FEM model, and the electrodes are spaced at a distance s apart. The design parameters of the electrodes are shown in Table 1. The orientation of the **E**-field is shown on the right in Fig. 1.

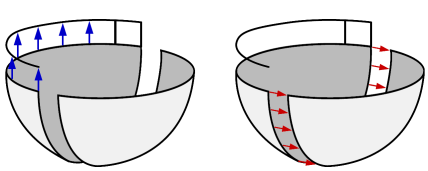

Fig. 1 *The novel combined system concept shown in 3D perspective. Plot of the **E**-field: high-frequency mode (left) and low-frequency mode (right).*

Fig. 2. Prototype, front (left) and back (right) view.

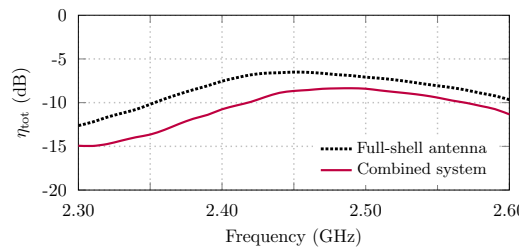

Fig. 3 *Measured antenna total efficiency for the device placed in the ear, full shell antenna (dotted line) and combined antenna-electrode system (solid line). The results are an average of the left-ear and right-ear prototype results.*

A prototype of the combined system is implemented on a 3-D printed plastic substrate with dielectric constant $\varepsilon_r = 2.4$ and loss tangent $\tan\delta = 0.012$. The prototype is shown in Fig. 2. The whole system is small, both physically and electrically, and can be encompassed by a sphere of radius $r = 12$ mm.

Measurement results: The measurements were conducted on a specific anthropomorphic mannequin (SAM) head with ears. The ears are made of a homogeneous dielectric material designed for RF use. The phantom liquid is CTIA-compliant at 2.4 GHz. All the measurement were conducted in a standard radio-anechoic chamber. Only the on-body scenario is taken into account, as it is representative of the actual operation case of the device. The measurement coordinate system is centered at the antenna position, i.e., the SAM head's ear. Given the antenna dimensions, the data are directly sampled in the Fraunhofer region and are therefore assumed as a correct representation of the true far-field. A bazooka balun and ferrite beads are added to the cables to prevent unwanted radiation. The antenna total efficiency η_{tot}, which is a function of the antenna radiation efficiency and of the mismatch loss, is plotted in Fig. 3. The decrease in efficiency is caused by the size reduction of the ground plane when the gap that separates the electrodes is introduced. The 3D directivity radiation pattern of the combined system, when placed in the right ear of the SAM head, is shown in Fig. 4 for two different head orientations.

The measurement and simulation set-up are shown in Fig. 5 for the electrode system. An additional pair of wideband baluns were added to the VNA cables in order to prevent the measurement system itself from introducing artifacts. In order to obtain reliable results, it is necessary to control the ground return path and to ensure that there is no indirect coupling between the ports. The measurements require averaging and narrow IF bandwidth to increase the VNA dynamic range at the lower

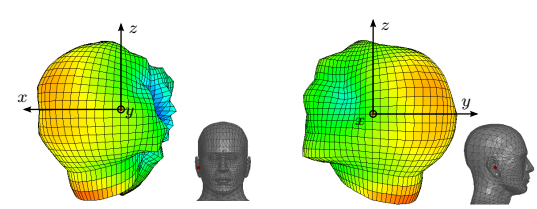

Fig. 4 *3D radiation pattern (directivity, in dBi) at 2.45 GHz when the antenna is placed in the right ear, front (left) and side (right) view. The color scale ranges from blue (low) to red (high).*

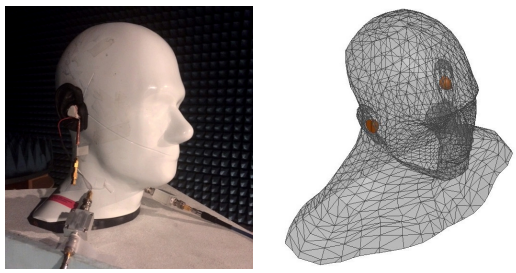

Fig. 5 *Set-up used for the estimation of the electrode ear-to-ear path gain PG_{E2E}, measurement (left) and simulation (right).*

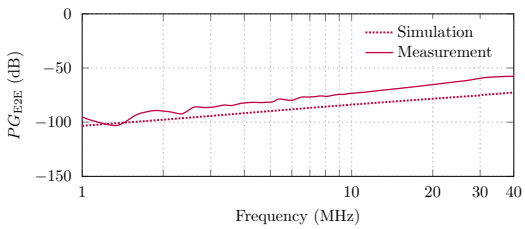

Fig. 6. Electrode ear-to-ear path gain PG_{E2E} at MHz frequencies.

frequencies. The coaxial feed of the high-frequency antenna is terminated with a 50 Ω load. The electrode ear-to-ear path gain PG_{E2E}, which is a function of the propagation loss and of the mismatch loss, is shown in Fig. 6. There is good agreement between simulations and measurements in terms of absolute difference and trend. The values in the 10–40 MHz range are comparable to the ear-to-ear transmission performance at 2.4 GHz [6]. The **E**-field intensity is plotted along the main propagation path across the head on a plane that spans the two ears and is shown in Fig. 7. A summary of the main performance parameters is shown in Table 2.

Conclusion: A novel dual-mode antenna-electrode system is introduced. For the first time, a combined system is designed and implemented in an application-realistic form factor, given the fact that this is among the main constraints affecting the actual performance. Simulations and measurements on a prototype show that the antenna exhibits high on-body radiation efficiency $\eta_{\mathrm{tot}} = 13.6\%$ at a primary frequency $f_1 = 2.4$ GHz. At the same time, the integrated electrode pair can transmit to a symmetric system along the in-body ear-to-ear channel at a secondary frequency $f_2 = 30$ MHz. It achieved a path gain as high as $PG_{\mathrm{E2E}} = -59.5$ dB. The combined antenna-electrode system is able to establish an effective off-body link to another device and an in-body ear-to-ear link.

A. Ruaro and K. B. Jakobsen (*DTU Electrical Engineering, Technical University of Denmark, DK-2800 Kongens Lyngby, Denmark.*)

J. Thaysen (*GN ReSound A/S, DK-2750 Ballerup, Denmark.*)

E-mail: kbj@elektro.dtu.dk

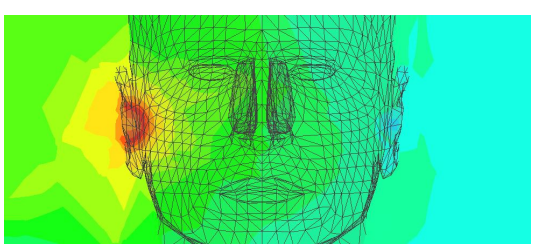

Fig. 7 *Plot of the **E**-field across the head model at a frequency $f = 30$ MHz. The color scale ranges from blue (low) to red (high).*

Table 1: Design parameters for the antenna (left) and electrodes (right).

h	2.7 mm
ℓ	24.0 mm
d	1.0 mm
w	1.5 mm

A	792 mm^2
s	3.0 mm

Table 2: System performance summary

Parameter	Value (dB)	Frequency (MHz)
η_{tot}	−8.66	2450
PG_{E2E}	−59.5	30

References

1 B. C. Kirkwood, S. A. Hallenbeck, and T. Stender: 'How can wireless data exchange in hearing instruments contribute to binaural hearing?,' *Hearing Review*, Vol. 19, No. 10, pp. 52–55, 2012.

2 A. Ruaro, J. Thaysen, and K. B. Jakobsen: 'Head-centric body-channel propagation paths characterization,' in *Proc. European Conf. Antennas Propag. (EuCAP)*, 2015.

3 K. Ito, N. Haga, M. Takahashi, and K. Saito: 'Evaluations of body-centric wireless communication channels in a range from 3 MHz to 3 GHz,' *Proc. IEEE*, Vol. 100, No. 7, pp. 2356–2363, 2012.

4 K. Ito: 'Compact dual-mode antenna for body-centric wireless communications,' in *Proc. European Conf. Antennas Propag. (EuCAP)*, 2015.

5 A. Ruaro, J. Thaysen, and K. B. Jakobsen: 'Cavity-backed on-body antenna for custom hearing instrument applications,' *Electronics Letters*, 2015.

6 S. H. Kvist, S. Özden, J. Thaysen, and K. B. Jakobsen: 'Improvement of the ear-to-ear path gain at 2.45 GHz using parasitic antenna element', in *Proc. European Conf. Antennas Propag. (EuCAP)*, 2011.